Wouter J. de Bruin BSc
Master Student Applied Earth Sciences
Delft University of Technology

Simulation of Geochemical Processes during Low Salinity Water Flooding by Coupling Multiphase Buckley-Leverett Flow to the Geochemical Package PHREEQC

A Case Study for an Oil Field on the Norwegian Continental Shelf

MSc Thesis
AES2006

Carried out at Statoil ASA,
a leading energy company in oil and gas production.

Supervisor TU Delft: Prof. Dr. Pacelli L.J. Zitha
Supervisor Statoil: Dr. Dagmar Spangenberg

Stjørdal, August 2012

Abstract

Simulations carried out for low salinity water flooding often do not include geochemical processes. Salt concentration, and thus the salinity, is modelled as a water tracer that does not react with the reservoir formation.

The goal of this MSc thesis is to improve the understanding of the influence of geochemical processes on the mixing of formation water and injection water, during low salinity water flooding. The geochemical processes taken into consideration are CO_2-buffering, ion exchange and mineral dissolution.

An initial understanding of the geochemical processes was gained by performing numerous simulations with the U.S. Geological Survey geochemical package PHREEQC. A limitation of this simulator is that it only allows for single-phase aqueous flow.

To overcome this limitation, a multiphase Buckley-Leverett simulator has been developed in MATLAB® that couples oil-water flow to the geochemical package PHREEQC. Subsequently, the newly developed simulator was used to study the effects of geochemical processes on the increase in oil recovery. In addition, simulations were performed to study low salinity slug sizes and dispersion.

Although the low salinity mechanisms are still subject of extensive research, it is assumed that increases in oil recovery due to low salinity water flooding can be modelled as a change in relative permeability, from oil- or mixed-wet to more water-wet.

Simulation results showed that fully removing calcite (calcite content 0.97 Wt%) from the reservoir, requires an excessive amount of pore volumes of low salinity water to be flushed through the reservoir. Therefore, dissolution of all calcite seems a near injector well-bore effect only. In the majority of the case study field, the minimum salinity level reached will be around 910 ppm.

Simulations also showed that, during the injection of low salinity water into the case study field, Na^+ attached to the cation exchanger is replaced by Ca^{2+}. This is a result of the preferential adsorption of double valence ions when lowering the ionic strength, and decreasing the Na^+/Ca^{2+} ratio in the reservoir.

In simulation runs where geochemical interactions were included, higher salinity levels were observed in the reservoir compared to passive salt tracer simulations. In addition to an increase of 160 ppm due to the initial calcite dissolution, a secondary increase due to calcite dissolution as a result of cation exchange was noted. Depending on the amount of exchange sites, significantly higher ion concentrations (~2000 ppm) were observed. As the low salinity effect is assumed to be triggered solely by the salinity level, including geochemical interactions can therefore lead to a lower low salinity EOR potential.

The increase in oil production observed for a non-geochemical affected secondary low salinity injection scheme (1.0 pore volume formation water followed by 4.0 pore volumes low salinity water) is 5.8% of the originally oil in place (OOIP) compared to a high salinity injection scheme (5.0 pore volumes of formation water), for low salinity thresholds ranging from 1000-3000 ppm. By including geochemical effects, the amount of incremental oil was 0.5%, 3.2%, 5.7% or 5.8% of the OOIP for a salinity threshold of 1000 ppm, 1500 ppm, 2000 ppm, or 3000 ppm, respectively. This indicates that, especially for low values of the low salinity threshold, geochemical interactions may be of importance for the EOR potential.

However, it is important to note that the amount of calcite and number of cation exchange sites have been calculated based on bulk rock data. In addition, it has been assumed that the aqueous phase is in contact with all calcite and clay. By doing so, the effects of the geochemical interactions are overestimated.

Dispersion was found to be very important for the determination of minimum low salinity slug sizes. However, no accurate dispersion data were available for the case study field to verify the current model. Simulation results showed that frequent (2 days/month) injection of seawater slugs during low salinity flooding may increase salinity levels throughout the whole reservoir above the threshold values, effectively eliminating the increase in oil production. Injecting larger seawater slugs on a less regular interval (2 weeks/year) results in fractions of the reservoir having a higher salinity than the threshold value. However, the overall impact on the cumulative oil production was far less (-0.6% of the OOIP compared to no seawater slugs).

An interesting continuation of this project would lie in a detailed study of the chemical composition of the rock surface. As the cation exchange sites are likely to be less, the impact of cation exchange induced calcite dissolution on the salinity is reduced. This will result in an increase of low salinity EOR potential.

Preface

This MSc thesis has been conducted at Statoil ASA in Stjørdal in partial fulfilment of the Master of Science degree in Applied Earth Sciences at the University of Technology Delft.

In the summer of 2011 I did a Statoil summer internship at the Reservoir Management Department in Stavanger. During that time, I made clear that I was also highly interested in a MSc thesis position. I would like to thank Sigurd Haugen, the department leader, for all his help in finding a MSc thesis position. It is due to his efforts that a suitable position in Stjørdal was found.

My sincere thanks go out to my daily supervisor Dagmar Spangenberg. Although there were 581 km between her desk and mine, daily communication via any means of electronic communication method resulted in an excellent follow up on my work.

I would also like to thank Alireza RezaeiDoust, Vegard Kippe, Kristian Sandengen, and all other interesting persons I met during the course of this thesis, for their valuable help and highly interesting discussions.

Thanks also go out to prof. dr. P.L.J. Zitha who found the time in his busy schedule to supervise my thesis. In addition I would like to thank prof. dr. J. Bruining, prof. dr. W.R. Rossen, and dr. ir. F.J. Vermolen for volunteering to be members of the examination committee.

Without the financial support of both the Erasmus program and Statoil I would not have been able to carry out this thesis.

Last but not least, I would like to thank my parents and my girlfriend, Femke Gelderblom. Their believe and encouragements have been a tremendous boost over the years that helped me to complete my studies at the Delft University of Technology.

Wouter de Bruin

Stjørdal, Augustus 2012

Contents

List of Tables

List of Figures

List of Acronyms

BL	Buckley-Leverett
CEC	Cation Exchange Capacity
CFL	Courant-Friedrichs-Lewy (condition)
COM	Component Object Model
CPU	Central Processing Unit
EDL	Electrical Double Layer
FW	Formation Water
HS	High Salinity
IOR	Improved Oil Recovery
LHS	Left-Hand Side
LS	Low Salinity
LSW	Low Salinity Water
MATLAB®	MATrix LABoratory
NCS	Norwegian Continental Shelf
OOIP	Original Oil In Place
PV	Pore Volume
RAM	Random Access Memory
RHS	Right-Hand Side
SI	Saturation Index
SRP	Sulphate Removal Plant
SWCTT	Single Well Chemical Tracer Test
TDS	Total Dissolved Solids
USGS	U.S. Geological Survey
XRD	X-Ray Diffraction

List of Symbols

Δt	Numerical time step	days
Δx	Numerical grid cell size	m
A	Surface	m^2
α	Phase type	-
C_γ	Concentration of ion type γ	mol/l
e	Elementary charge	C
ϵ_0	Permittivity of free space	$\mathrm{F \cdot m^{-1}}$
ϵ_r	Relative permittivity of water	-
f	Fugacity	-
f_w	Fractional flow for water	-
g	Gravitational acceleration	$\mathrm{m/s^2}$
γ	Interfacial tension	N/m
γ	Ion type	-
h	Dimensionless particle velocity	-
I	Ionic strength	$\mathrm{mol/m^3}$
κ^{-1}	Debye length	m
k	Absolute permeability	m^2 or cP
k_{ro}	Relative permeability to oil	-
k_{rw}	Relative permeability to water	-
k_B	Boltzmann constant	$\mathrm{J \cdot K^{-1}}$
λ_α	Mobility of phase α	$\mathrm{m^3 \cdot s/kg}$
n	Amount of moles	mol
N	Number of grid cells	-
N_A	Avogadro constant	1/mol

p_c	Capillary pressure	Pa
P_{CO_2}	Partial pressure of CO_2	atm
P_r	Reservoir pressure	atm
q	Flow rate	m^3/day
ϕ	Porosity	-
Φ	Potential	eV
R	Dissolution rate	mol/(cm^2·s)
R	Universal gas constant	J·(mol ·K)$^{-1}$
ρ	Density	kg/m^3
S_o	Oil saturation	-
S_{or}	Residual oil saturation	-
S_w	Water saturation	-
S_{wc}	Connate water saturation	-
T	Temperature	K or °C
θ	Reservoir inclination angle	°
Θ	Contact angle	°
u	Darcy velocity	m/day
v	Characteristic velocity	m/day
V	Volume	m^3
x	Fraction of mineral	-
x	Distance	m

Chapter 1

Introduction

The estimated world energy demand is expected to grow continuously for the next 30 years. Although the share of oil in the world's energy mix is likely to decrease throughout the next three decades, the total demand for oil during this period will increase from around 90 Mbpd to 100 Mbpd (Statoil ASA, 2012). To be able to meet future demand it is of utmost importance to get the most oil out of existing fields.

To do so, both improved oil recovery (IOR) and/or enhanced oil recovery (EOR) methods can be used. IOR methods are often regarded as processes that add energy to a reservoir to stimulate oil production and increase the recovery factor. EOR techniques do not merely add energy to a reservoir, but aim at altering the original properties of oil or oil/rock interactions to improve displacement, and subsequently reservoir recovery (Schlumberger, 2012).

EOR on the Norwegian Continental shelf (NCS) is not novel. The NCS has an extensive history of EOR projects, which have led to higher recovery factors compared to other oil and gas provinces around the world. The average recovery factor for Statoil operated fields in Norway has risen to 50% this year (Statoil ASA, 2012). Without EOR methods, this would not have been possible. Numerous EOR methods have been tested and studied on the NCS over the past four decades. Among these methods are miscible gas injection, water-alternating-gas injection, simultaneous water-and-gas injection, foam-assisted WAG injection, and microbial EOR (Awan et al., 2008).

As a way of improving the recovery from oil and gas fields, water flooding has been known and used for almost a century all over the world in a wide variety of fields. In the past, the chemical composition of the injected water was designed, if at all, to ensure minimum risk of formation damage. This strategy was also applied during the time that the first water injection schemes for the NCS were developed. A great effort was put into the quality of the water mainly with respect to reservoir formation damage (Mitchell and Finch, 1981).

The potential for enhanced oil recovery by varying the chemical composition of the injection water was first shown by Yildiz and Morrow in 1996. Studies have been carried out, continuing along this path, which demonstrated that by decreasing the salinity of injection water the oil recovery can be increased (Tang and Morrow, 1997).

The underlying principles that govern the low salinity effect are still not well understood and are subject of extensive research. The proposed mechanisms are both physical, e.g. fines production that can block high permeable zones, and geochemical. These mechanisms involve wettability alteration of the oil-water-rock system from often mixed-wet to more water-wet. Immobile oil that was formerly stuck to the rock can now be produced resulting in higher oil recovery. Because low salinity water injection targets previous immobile oil, it qualifies as an EOR technique.

The objective of this work is to improve the understanding of the geochemical interactions upon injection of low salinity water in the NCS reservoir under consideration. Mixing, ion exchange and mineral dissolution are the main mechanisms of interest. Focus is put on the interactions between the rock surface and aqueous phase.

For studying the geochemical interactions use will be made of the PHREEQC geochemical simulator, made available by the U.S. Geological Survey. This simulator is able to calculate detailed ion speciation in one-dimensional single-phase aqueous flow through porous media in combination with surface chemistry.

To improve the simulations a multiphase Buckley-Leverett flow simulator will be built in MATLAB® and is coupled to the geochemical simulator PHREEQC. The aim of this simulator is firstly, to increase the understanding of the two-phase flow on the geochemical behavior. Secondly, the intention is to develop an easy-to-use tool that can be applied for similar future reservoir geochemistry studies.

The main body of this thesis is divided into four chapters. Chapter 2 provides an introduction to the low salinity water injection EOR method and will cover general wettability, an introduction to the low salinity mechanisms, geochemical interactions, and Buckley-Leverett modeling. Chapter 3 presents the simulations performed with the PHREEQC geochemical simulator are depicted. Chapter 4 describes the mathematical methods and assumptions used to construct the coupled simulator. The results of the simulations carried out with this simulator are described in Chapter 5. Conclusions, based on the entire thesis, and suggestions for future work are covered in Chapter 6.

Chapter 2

Theory

This chapter will cover the classic theory regarding wettability and depict current methods for modelling low salinity influences on relative permeability. The proposed mechanisms underlying the low salinity water flooding EOR method are examined in detail. Next, geochemical interactions like mixing, ion exchange, and mineral dissolution will be investigated. Finally, the Buckley-Leverett flow theory will be covered both for classical and low salinity water flooding settings.

2.1 Wettability

The concept of wettability is the basic macroscopic model used in reservoir engineering to describe the preference of reservoir rock to be in contact with either oil, water, or both. During the injection of low salinity water one aims at altering the wettability of the rock such that more oil is released. This section will introduce the reader to the basic theory behind wettability and the influence of wettability on relative permeability.

2.1.1 Basics

The ultimate oil recovery from a reservoir using a water drive is highly dependent on the wettability of the reservoir. This quantity describes the preference of the rock to be in contact with one fluid or another. In a water-wet two-phase system that interacts with the rock matrix, e.g. an oil reservoir with connate water, the rock surface will prefer to be in contact with water. This principle is shown schematically in Figure 2.1. For a water-wet reservoir, oil tends to have little contact to the matrix compared to water. Wettability is not a discrete process, every wetting state ranging from fully water-wet to fully oil-wet can occur.

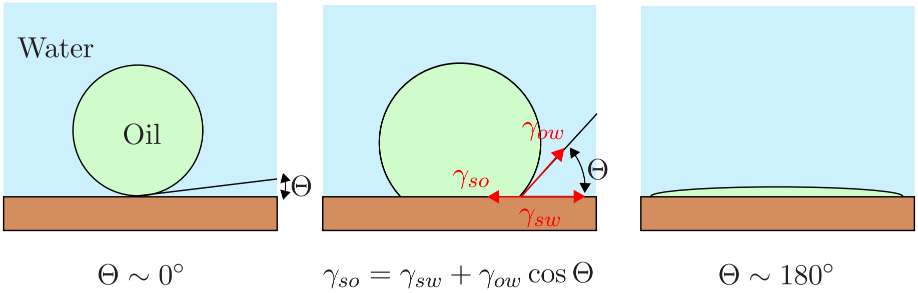

Figure 2.1: Example of wettability differences for an oil droplet. From left to right: water-wet, mixed-wet and oil-wet. Redrawn after Abdallah et al. (2007).

A measure for the wettability of a phase, is the contact angle with respect to the surface of the rock. The contact angle is a result of the interfacial tension γ_{so} and γ_{sw} for the surface-oil and surface-water terms, respectively, and γ_{ow} for the oil-water term (Abdallah et al., 2007).

For a water-wet oil reservoir the contact angle between the rock surface and the oil is $\Theta < 90°$. For the oil-wet case $\Theta > 90°$. Intermediate wetting is loosely defined as $\Theta \sim 90°$ (Dake, 1978).

Understanding the wettability of multiphase porous medium systems has always been challenging, as it arises due to a combination of *physical* and *chemical* processes that influence each other in many ways (Drummond and Israelachvili, 2004). Over the last few decades, many studies have aimed at improving the understanding of wettability and its influence on oil recovery. More water-wet oil reservoirs, in general, tend to have a more favorable oil displacement and hence better recovery compared to oil-wet systems. Whether or not this is true in a specific reservoir depends on the rock's pore system (Chilingar et al., 1996).

2.1.2 Influence on Displacement

The wetting phase in an uniformly wetted system will be both found in the smaller pores and spread out as a thin film covering the rock surface in the larger pores. The non-wetting phase is found in the centers of the larger pores (Anderson, 1987).

Figure 2.2 illustrates the impact of wettability on the relative permeability of both the wetting and non-wetting phase.

In the case of a water-wet reservoir (Figure 2.2(a)) a thin film of water will cover the rock surface. Upon injection of water into the reservoir, water will preferably move along the rock surface. Because water follows the rock surface it will travel through smaller pores compared to the non-wetting phase. Oil,

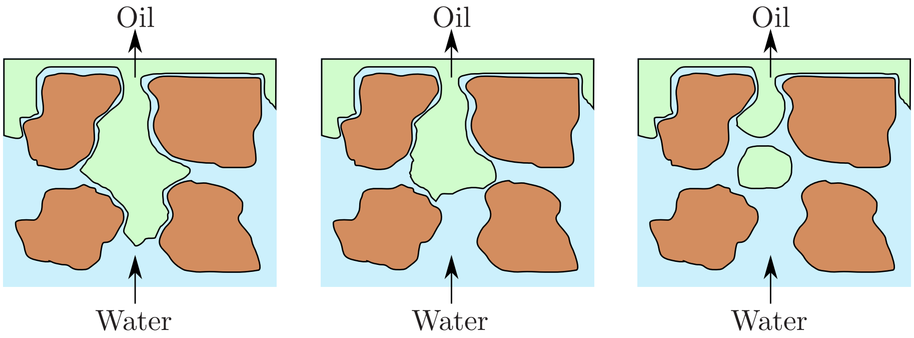

(a) Example of a water-wet system

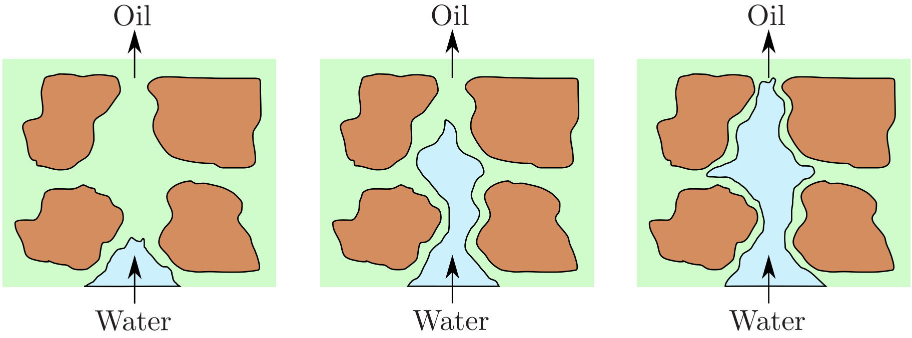

(b) Example of an oil-wet system

Figure 2.2: Water displacing oil from a pore during water flooding. Figure 2.2(a) shows displacement in a strongly water-wet reservoir. Figure 2.2(b) shows the displacement in a strongly oil-wet reservoir. Redrawn after Raza et al. (1968).

the non-wetting phase in this case, will travel through the larger pores.

For an oil-wet reservoir (Figure 2.2(b)), oil covers the rock surface. Upon water injection, the non-wetting water phase will flow through the larger pores. By doing so, it will bypass vast amounts of smaller pores filled with valuable oil. This results in earlier water breakthrough and lower oil recovery compared to the water-wet case.

From this illustration it is clear that, by changing the wettability of a reservoir from oil- or mixed-wet to water-wet, the relative permeability of water is reduced while at the same time the relative permeability for the oil flow is increased. This results in more favourable flow conditions for oil. In addition, the residual oil saturation will be lower as previous immobile oil attached to the surface has been mobilized.

2.1.3 Impact of Low Salinity Flooding

Multiple studies (including Mahani et al. (2011), Robertson (2007), Vledder et al. (2010)) have shown that low salinity water injection can alter the wettability on a field-wide scale. Existing evidence suggests that low salinity water injection used in mixed-to-oil-wet sandstone reservoirs can lead to a more water-wet rock surface, a lower remaining oil saturation and higher oil recovery.

It is however important to note that there have also been studies conducted that have led to more oil-wet reservoirs after flooding with low salinity water (Sandengen et al., 2011). The same study additionally reported that a complete halt in oil production can occur upon injection of low salinity water. This indicates that it is of utmost importance to have a good understanding of the geochemical processes in addition to the physical processes taking place in an oil reservoir.

An exact definition for oil fields that will benefit from low salinity water injection does not yet exist. However, low salinity injection has high potential to act as a wettability modifier, if the mixed-to-oil-wettability in a sandstone reservoir is caused by (Vledder et al., 2010)

- grain surface distributed clays such as kaolinite,
- highly saline ($\gg$ 10,000 ppm) formation water particularly with high content of divalent cations, e.g. Ca^{2+}, and
- reservoir crude containing surface-active components.

The way low salinity water flooding changes wettability is not yet fully understood. The next section covers three proposed mechanisms for low salinity water flooding, which are considered to be most plausible.

2.2 Low Salinity Mechanisms

Several low salinity mechanisms have been proposed in the last decade. Three main mechanisms that will be discussed in more detail are electrical double layer expansion, ion exchange and clay mobilization. These mechanisms are based on geochemical processes. Clay mobilization can however also have physical effects, e.g. clogging of pores.

2.2.1 Electrical Double Layer Expansion

At the interface between a charged surface and a solution a potential will develop. This potential difference is build up out of two distinct layers, with their respective properties. Because of these two layers, it is called the electrical double layer (EDL). A schematic overview of the EDL is shown in Figure 2.3. The two layers within the EDL are:

(a) *Stern layer*: a compact layer close to the charged surface with a thickness of about 1 nm. Ions in this layer are fixed. The major part of the potential drop will occur over this layer (Grahame, 1947).

(b) *Diffuse layer*: a layer with varying thickness between 1-500 nm, depending on the extent of *double layer expansion.* Ions of opposite sign with respect to the charged surface are attracted as a result of electrostatic forces. At the same time, a diffusivity related osmotic pressure difference counteracts this and tries to equilibrate the ion concentration with respect to the bulk solution. A similar force competition occurs for ions with the same sign as the surface. Due to electrostatic forces these ions are repelled from the surface. Back-diffusion from the bulk solution counteracts the repulsion (Van Olphen, 1977).

    The diffuse layer is split up into two separate regions by the Zeta potential. The equipotential plane formed by the Zeta potential is also called the slipping plane as it defines the region of ions that can move (slip) along the region with more tightly fixed ions:

    (I) Region Stern Potential-Zeta Potential: In this region the ions will not be affected by tangential stress, such as water flowing past the solid's surface (e.g., clay). The ions are tightly bound to the solid's surface in the double layer.

    (II) Region Zeta Potential-Bulk Fluid: In this region of the diffuse layer the ions can move under influence of tangential stress. That is, the force that keeps the ions in place can be overcome by water flowing past the solid's surface.

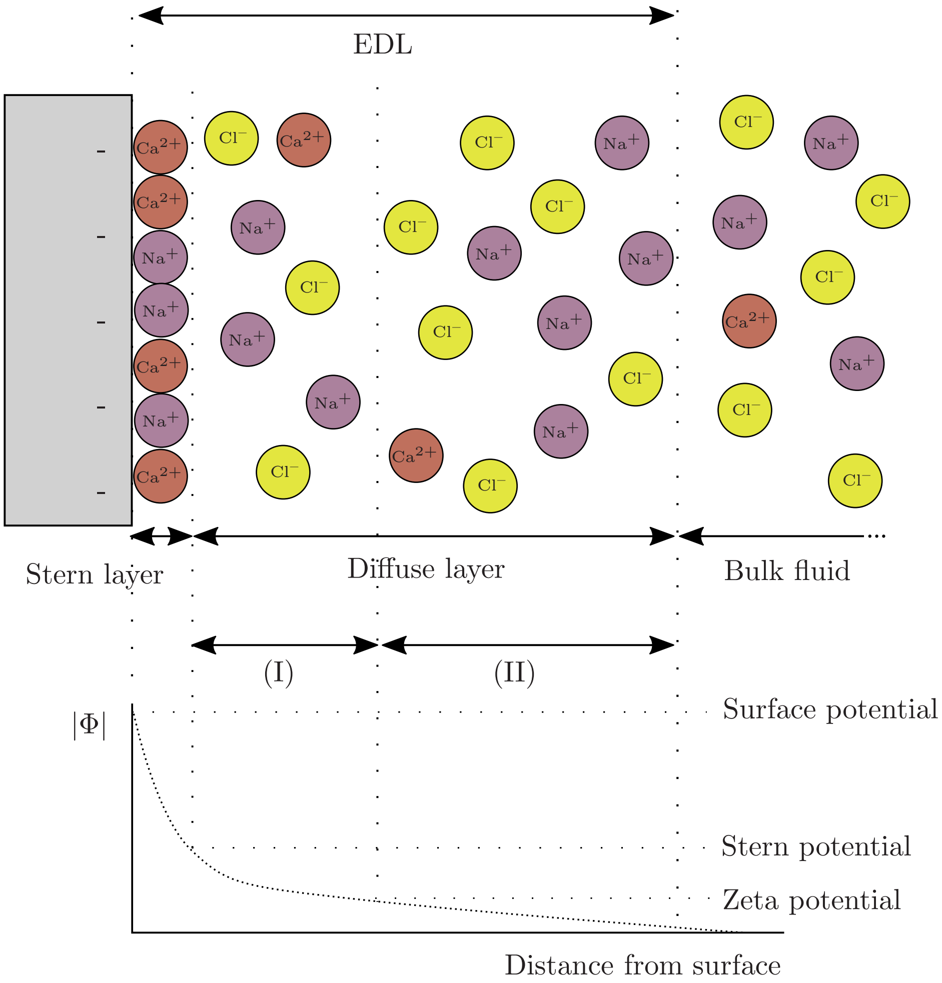

Figure 2.3: Schematic illustration of the electrical double layer (Stern-layer model) occurring on clay with a negative surface charge. The potential compared to the bulk fluid as function of the distance from the clay surface is drawn below the schematic model. Note that the ratio between positive and negative charges becomes smaller (i.e., the ratio will reach a value close to one) if one moves from the negatively charged clay surface towards the bulk fluid.

In general, it holds that ions further away from the charged surface easier to displace than ions close to the charged surface. The potential drop over the diffuse layer is more gradual compared to the potential drop in the Stern layer.

The thickness of the EDL is dependent of the ionic strength of the solution. During low salinity water flooding, the electrolyte concentration of the bulk water solution diminishes, which effectively leads to an expansion of the EDL. Especially the diffuse layer will behave in this fashion. However, for an increase in electrolyte concentration the EDL thickness will be significantly compressed. Multi valence ions have a larger impact on double layer expansion or compression compared to single valence ions (Stumm and Morgan, 1996).

Two types of double layers can occur, namely:

- *EDL due to adsorption of potential-determining ions*: this type of double layer is created by the preferential adsorption of a single type of potential-determining ion. Adsorption can occur due to chemical bonds or due to physical adsorption (e.g., hydrogen bonds and Van der Waals forces). The preferentially adsorbed ions will form the inner coating of the EDL. The counter ions that will be accumulated on top will result in a second layer. Together they form a double layer. Upon changing the salinity, the surface potential will remain constant whilst the surface charge changes.
- *EDL due to interior crystal imperfections*: this type of double layer forms as a result of imperfections in a clay lattice. For the case study field, kaolinite has imperfections leading to a negative surface charge per unit area. This quantity, the charge density, is fixed. Upon injection of low salinity water the surface charge therefore cannot change. However, the surface potential (i.e., the potential difference between the two-phases) will change. The surface potential will become smaller upon injection of low salinity water, and become larger for higher concentrations of electrolytes. This type of EDL is regarded as being of more importance in low salinity water flooding (Statoil ASA, 2010).

The low salinity effect that leads to improved oil recovery is not observed above the threshold salinity of 5,000 ppm TDS (RezaeiDoust et al., 2009). From Zeta potential measurements during Statoil core flooding experiments it was shown that this behavior coincides with the behavior of EDL expansion (Statoil ASA, 2010). That is, no significant EDL expansion is observed for salinities above 5,000 ppm TDS.

For values below the threshold salinity, the EDL will expand as the potential difference between the fixed charge density on the clay and the bulk fluid increases. In physical chemistry, the Debye length κ^{-1} is regarded as the thickness of an EDL. The Debye length is a function of the solution's ionic strength, and can be calculated as follows (Stumm and Morgan, 1996)

$$\kappa^{-1} = \sqrt{\frac{\epsilon_r \epsilon_0 k_B T}{2 N_A e^2 I}} \tag{2.1}$$

where ϵ_r is the relative permittivity, ϵ_0 the permittivity of free space, k_B the Boltzmann constant, T the absolute temperature, N_A the Avogadro constant, e the elementary charge, and I the solution's ionic strength. The Debye length

Table 2.1: Debye length calculation parameters for the case study field

Parameter	Unit	Value	Comment
ϵ_r	-	78.5	Relative permittivity for water
ϵ_0	$F \cdot m^{-1}$	$8.854 \cdot 10^{-12}$	Permittivity of free space
k_B	$J \cdot K^{-1}$	$1.381 \cdot 10^{-12}$	Boltzmann constant
N_A	1/mol	$6.022 \cdot 10^{23}$	Avogadro constant
e	C	$1.602 \cdot 10^{-19}$	Elementary charge
T	K	358.15	Reservoir temperature
I	mol/m^3	$0\text{-}1 \cdot 10^{-3}$	Ionic strength

for varying ionic strength can be calculated for the case study field by making use of Equation 2.1 and the parameters from Table 2.1.

Figure 2.4 shows the calculated Debye length for the case study field as a function of the ionic strength. In the same figure, the ionic strength of the case study field formation water (FW) as well as the ionic strength of low salinity water (LSW) are plotted. The corresponding Debye lengths are approximately 35 nm and 300 nm, respectively. After low salinity water injection, the EDL will have expanded approximately 9 times. However, it is clear from the figure that the expansion is highly non-linear. The largest change in EDL thickness occurs at relatively low ionic strength.

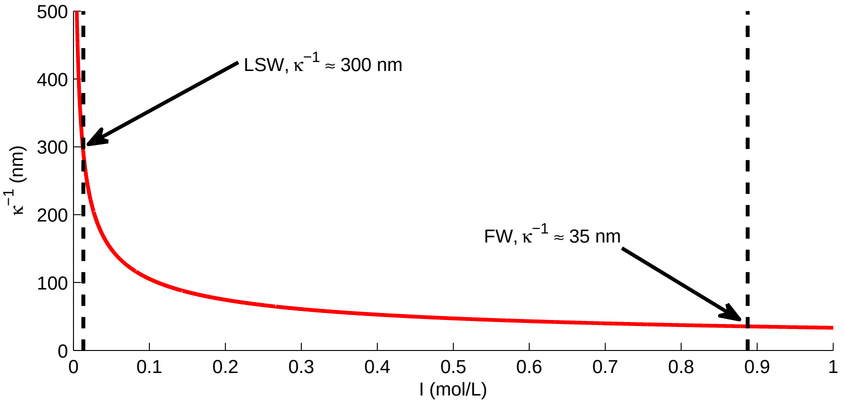

Figure 2.4: Debye length as function of ionic strength.

A threshold ionic strength can be defined at which the expansion of the double layer reaches a certain desired value. The ionic strength threshold can be converted into a salinity, which is the preferred way of representing the threshold value in the oil and gas industry. For the electrical double layer effect, it is important that salinities in reservoir simulations are accurate, as small deviations at low salinities can have large impact on the EDL expansion, and consequently on the EOR efficiency.

2.2.2 Ion Exchange

The ion exchange mechanism starts from the principle that oil particles can be attached to clays in 8 different ways (Lager et al., 2007). Not all clay attachment mechanisms are equally important. For simplicity, only direct cation exchange and organometallic complexes are taken into consideration in this description. Ion exchange is in fact closely related to the electrical double layer mechanism. Ion exchange, as described by Lager et al. (2008), takes place mainly in the EDL region.

Figure 2.5 illustrates the basic idea behind the ion exchange mechanism. During high salinity (HS) flooding, with FW or seawater, charged oil particles will mostly remain attached to the cation exchanger sites. During injection of low salinity water in a reservoir containing calcite, the amount of Ca^{2+} attached to the cation exchanger sites will increase. As a result of this process, positively charged oil particles and organometallic complexes from the exchanger will detach. Both in lab experiments (Lager et al., 2007) and field

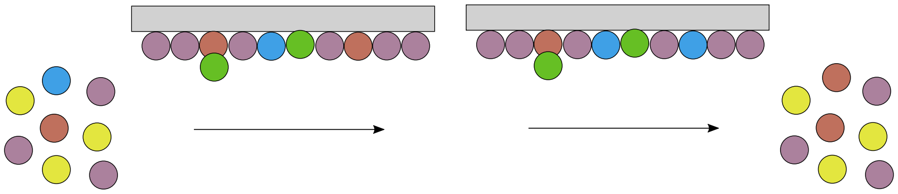

(a) HS, before flooding

(b) HS, after flooding

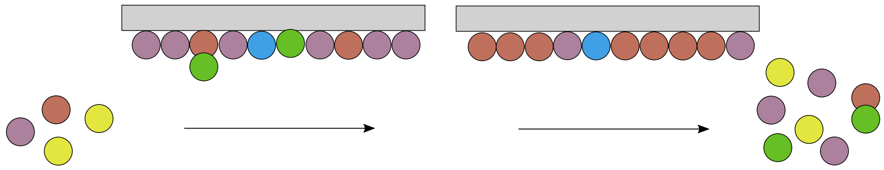

(c) LSW, before flooding

(d) LSW, after flooding

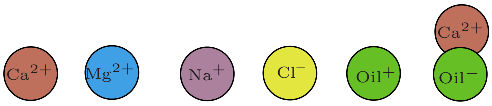

(e) Legend

Figure 2.5: Simple representation of ion exchange low salinity mechanism.

tests (Apello and Postma, 2005), lower Ca^{2+} concentrations have been measured in the produced water compared to the concentrations in the formation and injection water for clay containing siliciclastic sedimentary rocks. This indicates that other attached ions are exchanged by Ca^{2+}.

This process will decrease the amount of oil that contacts the rock matrix. This means that the reservoir changed from mixed- or oil-wet to a more water-wet state. As the oil particles that have been detached were previously immobile, the residual oil saturation of the reservoir is lowered.

This theory was tested experimentally by Lager et al. (2008). In the experiment, a core was flooded with a NaCl-brine many times over as to remove all traces of Ca^{2+} and Mg^{2+} from the exchanger. The column was then flooded with oil. After aging, a high concentration NaCl-brine as flushed through the core, followed by a low concentration NaCl-brine. A tertiary low salinity flood was then performed, only now the water contained some Ca^{2+} and Mg^{2+}.

Due to the initial removal of Ca^{2+} from the core, no organometallic complexes could form. Since no organometallic complexes were formed, that could potentially be removed by low salinity water injection, the primary HS flood was now able to bring the oil saturation down to residual oil saturation. The results matched the predictions: no increase in oil recovery was found for both low salinity floods.

It is important to keep track of the composition of the exchanger as the EOR potential for this low salinity mechanism depends on it.

2.2.3 Clay Mobilization

Tang and Morrow (1997) carried out various core flooding experiments for different oil compositions, temperatures and salinities. They concluded that oil recovery can benefit from low salinity water flooding. Additional experimental research was published (Tang and Morrow, 1999b) and related the increase in oil recovery to clay mobilization, also called fines production or fines migration.

Tang and Morrow (1999b) reported a decrease in permeability during core flooding experiments but did not observe severe clay mobilization. Tang and Morrow (1999a) showed that for both monovalent and multivalent low salinity brine, oil recovery can increase. Figure 2.6 shows a schematic overview of the clay mobilization concept as described by Tang and Morrow (1999b).

Figure 2.6(a) illustrates the water-wet and mixed-wet fines covering the rock surface at low initial water saturation. The mixed-wet fines both interact with the oil and water, as shown in Figure 2.6(b). Due to a competition between mechanical and colloidal forces only partial mobilization of mixed-wet fines will be achieved during water flooding, see Figure 2.6(c). As mixed-wet fines both interact with the oil and water, they tend to group at the oil-water interface acting as interface stabilizing surfactant. After high salinity water flooding, some oil attached to mixed-wet fines will remain in the reservoir.

When the salinity of the injection water is reduced, the electrical double layer of the particles is expanded. As a result of this, the tendency to strip mixed-wet fines from the reservoir rock increases, which causes a partial mobilization of previous immobile oil, see Figures 2.6(d) and 2.6(e).

In the clay mobilization mechanism, the increase in oil production during low salinity water injection is accounted to the mobilization of mixed-wet clay particles. The incremental oil production originates from:

- Direct mobilization of otherwise immobile oil due to mobilization of the clay particles to which the oil is attached. As a result, the residual oil saturation decreases.
- Indirect mobilization of oil due to blocking of prolific flow paths. This leads to flow through less permeable zones enhancing the sweep efficiency.
- Clay particles acting as surfactant on oil-water interfaces. This results in stabilized oil-water interfaces enhancing the displacement.

Mechanical effects such as pore blocking or porosity changes due to clay mobilization are not taken into account in this thesis.

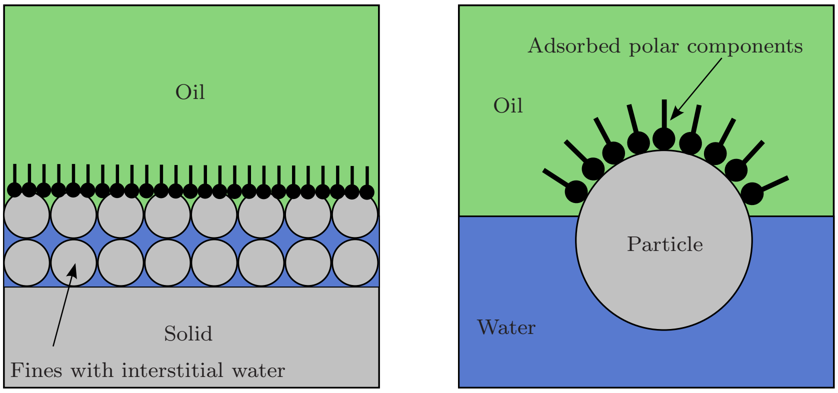

(a) Adsorption onto potentially mobile fines at low initial water saturation

(b) Mobilized particle at oil-water interface

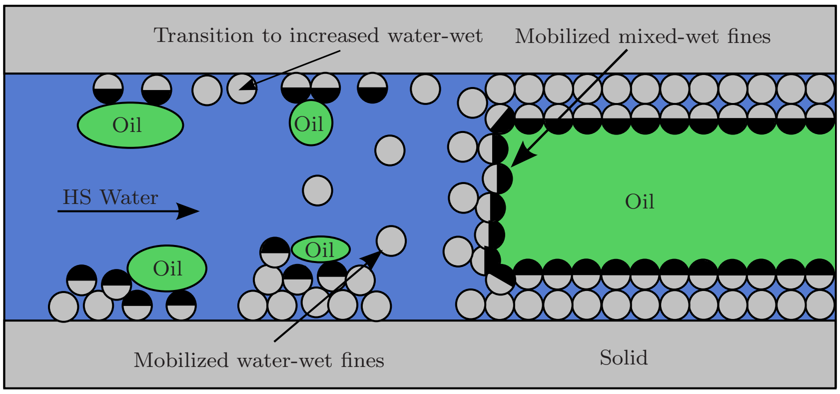

(c) Partial stripping of mixed-wet fines from pore walls during water flooding

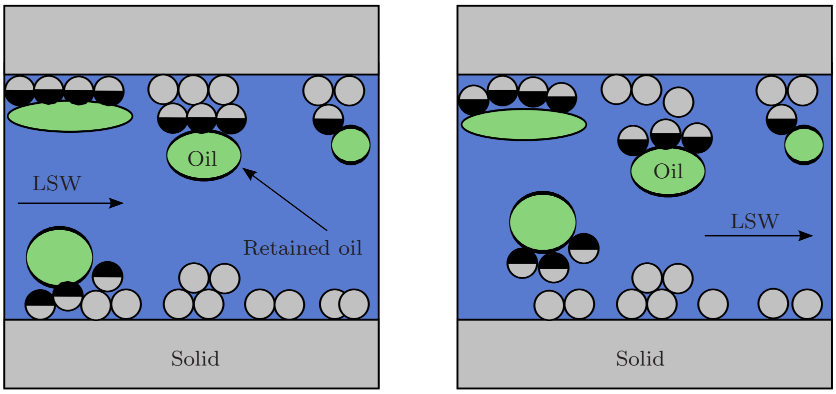

(d) Retained oil before injection of dilute brine

(e) Partial mobilization of residual oil through detachment of fines

Figure 2.6: Role of potentially mobile fines in clay mobilization, redrawn after Tang and Morrow (1999b).

2.3 Geochemical Interactions

When injecting low salinity water into an oil reservoir, it will not only act as an inert displacement medium that boosts the reservoir pressure. Numerous geochemical interactions will also take place, which have an important impact on the fluid behavior and oil recovery. For the case study field these interactions include

- carbonic acid equilibria,
- dissolution and/or precipitation, and
- sorption (i.e., absorption, adsorption and ion exchange).

Dissolution, precipitation, adsorption and ion exchange take place at the surface of the rock. A general term for these processes therefore is *surface chemistry*. During absorption ions will go into a solid's lattice and this process is therefore not referred to as being surface chemistry. The carbonic acid equilibrium is assumed to take place evenly spread throughout the aqueous phase. Each process will be discussed in more detail having the characteristics of the case study field in mind. The description of the geochemical processes is mostly based on Apello and Postma (2005).

2.3.1 Carbonic Acid Equilibria

As in many oil fields, carbon dioxide (or CO_2) is present as a gas in the case study field. The CO_2 present in the reservoir is partly dissolved in the formation water leading to aqueous CO_2

$$CO_2(g) \rightleftharpoons CO_2(aq) \tag{2.2}$$

Part of the CO_2 in solution will associate with water to form carbonic acid via the following equilibrium reaction equation

$$CO_2(aq) + H_2O \rightleftharpoons H_2CO_3 \tag{2.3}$$

Typically, this equilibrium leans highly to the left side making CO_2 in distilled water at 25°C about 600 times more abundant than H_2CO_3 (Apello and Postma, 2005). To simplify notation, the sum of $CO_2(aq)$ and H_2CO_3 will be written as $H_2CO_3^*$ resulting in the overall equilibrium reaction

$$CO_2(g) + H_2O \rightleftharpoons H_2CO_3^* \tag{2.4}$$

An overview of the equilibria in the carbonic acid system is given in Table 2.2.

Table 2.2: Carbonic acid system equilibria (Apello and Postma, 2005)

Equilibrium formula	Equilibrium Constant	Value
$H_2O \rightleftharpoons H^+ + OH^-$	$K_W = [H^+][OH^-]$	$10^{-14.0}$
$CO_2(g) + H_2O \rightleftharpoons H_2CO_3^*$	$K_H = [H_2CO_3^*]/[P_{CO_2}]$	$10^{-1.5}$
$H_2CO_3^* \rightleftharpoons H^+ + HCO_3^-$	$K_1 = [H^+][HCO_3^-]/[H_2CO_3^*]$	$10^{-6.3}$
$HCO_3^- \rightleftharpoons H^+ + CO_3^{2-}$	$K_2 = [H^+][CO_3^{2-}]/[HCO_3^-]$	$10^{-10.3}$

When an open system with respect to CO_2 pressure is assumed, which means that the CO_2 pressure is both known and fixed, the CO_2 species can be easily calculated for a distilled water. For a given CO_2 pressure the $H_2CO_3^*$ concentration will be known and independent of pH via

$$\log[H_2CO_3^*] = \log[P_{CO_2}] - 1.5 \tag{2.5}$$

The HCO_3^- concentration is given by

$$\log[HCO_3^-] = \log[H_2CO_3^*] + \text{pH} - 6.3 \tag{2.6}$$

which is a function of pH. The CO_3^{2-} concentration is also a function of pH, and the HCO_3^- concentration, as follows

$$\log[CO_3^{2-}] = \log[HCO_3^-] + 2\text{pH} - 16.6 \tag{2.7}$$

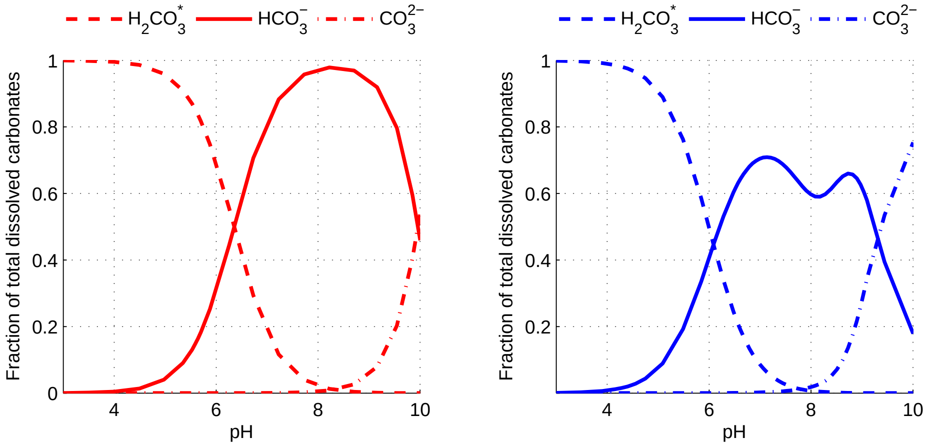

(a) Distilled water

(b) Formation water

Figure 2.7: Comparison of carbonic species as a fraction of the total dissolved carbonates between distilled water (2.7(a)) in equilibrium with CO_2 at atmospheric conditions at 25°C and formation water (2.7(b)) at reservoir conditions.

Plotting these functions, either directly or as done in this case by making use of the geochemical simulation software PHREEQC, as fractions of the total dissolved carbonates versus pH leads to Figure 2.7(a). Note that the $H_2CO_3^*$ concentration is fixed. The total amount of dissolved carbonates increases upon increasing the pH.

However, performing a carbonate-species analysis by hand for formation water would be a tedious task as equilibria with other ions in the solution must be taken into account. The final speciation of a particular solution will therefore result from an iterative process. The strength of the geochemical simulator PHREEQC is that it automates this process.

As an example the same analysis carried out for distilled water has been carried out for the case study formation water in the absence of rock interactions, leading to the results plotted in Figure 2.7(b). As can be seen, due to the formation of other species, the fraction of HCO_3^- for the two types of water shows quite different behavior for the pH range of 3-10.

Determining CO_2 Pressure

The CO_2 pressure in the case study field can be calculated using the ideal gas law, corrected using the fugacity coefficient f for the reservoir's non-ideal behavior, and using the CO_2 content measurements from Appendix A (Moran et al., 2010)

$$P_{\mathrm{CO}_2} = \frac{n_{\mathrm{CO}_2}}{n_m} P_r f \tag{2.8}$$

where n_{CO_2}/n_m is the measured CO_2 fraction of the mixture, and P_r the reservoir pressure from Appendix A.

An estimate for the fugacity coefficient of $f = 0.6$ at reservoir conditions of the case study field was found in the literature (Spycher and Reed, 1988). A second estimate was calculated using MultiScale 8.0[1] which resulted in $f = 0.7$. In this thesis the average of $f = 0.65$ for the fugacity coefficient is used.

2.3.2 Dissolution and Precipitation

Dissolution and precipitation reactions are of major importance when considering water composition in both low salinity and conventional water flooding. Even before the EOR potential of low salinity water was discovered reservoir engineers focussed on 'water quality' with respect to dissolution and precipitation of minerals (Mitchell and Finch, 1981). Especially precipitation can

---

[1] MultiScale is a software package developed by the NTNU and Scale Consultant AS which can be used to calculate the fugacity coefficient of a mixture.

lead to formation damage and/or scaling[2]. As the low salinity injection water that will be used in the case study field only contains low concentrations of dissolved sodium chloride, scaling is unlikely.

The composition of case study formation rock samples was determined by X-ray diffraction (XRD). The XRD data shows that the dissolvable minerals calcite and dolomite are present in the rock, both with around 1 Wt%.

a) Calcite

The brine used in LSW injection consists often only of moderate concentrations of monovalent ions such as Na^+ and Cl^-. By injecting this water into a reservoir the established equilibria between the formation water and dissolvable minerals are disturbed. For the case study field, this will lead to calcite dissolution as the Ca^{2+} concentration of the injected water is approximately zero, whereas the equilibrium with calcite in the reservoir prescribes a higher concentration. The concentration of Ca^{2+} is reestablished by dissolving calcite.

Calcite can dissolve in water according to the following dissolution equilibrium reaction

$$\mathrm{CaCO_3} \rightleftharpoons \mathrm{Ca^{2+}} + \mathrm{CO_3^{2-}} \tag{2.9}$$

In (distilled) water not in contact with CO_2, Equation 2.9 would fully describe the situation. However, as the reservoir water is in contact with carbon dioxide and other species, the calcite dissolution is more complex (Apello and Postma, 2005). Recall from the previous section that the contact with CO_2 leads to different carbonate species for various pH values. If one includes these equilibrium reactions (Table 2.2) into the calcite dissolution reaction, the overall reaction between carbon dioxide and $CaCO_3$ becomes

$$\mathrm{CO_2(g)} + \mathrm{H_2O} + \mathrm{CaCO_3} \rightleftharpoons \mathrm{Ca^{2+}} + 2\,\mathrm{HCO_3^-} \tag{2.10}$$

clearly indicating the relation between the carbon dioxide in the reservoir and calcite dissolution. As bicarbonate (HCO_3^-), which is a base, also plays a role in the dissolution equilibrium, this process will also influence the pH of the system. In Section 3.2.2 the relationship between CO_2 pressure and pH is analyzed.

The rate at which calcite is dissolved is limited by the dissolution rate, and the specific surface of the mineral. Pokrovsky et al. (2009) proposed a second-order polynomial empirical relation to estimate the calcite dissolution rate

$$\log R = A + B \times P_{\mathrm{CO_2}} + C \times (P_{\mathrm{CO_2}})^2 \tag{2.11}$$

---

[2] Mineral precipitation is called *scaling* in the oil industry. Scaling can lead to severe clogging of pipes, or the wellbore.

where R is the dissolution rate in mol/(cm^2·s) and $P_{\mathrm{CO_2}}$ is the partial pressure of CO_2 in atmosphere. The parameters A, B and C are empirical and depend on temperature and pH. For conditions ($T = 100$ °C; pH $= 5$) close to reservoir conditions ($T = 85$ °C; pH $= 5.7$) the values are $A = -7.75$, $B = -0.00169$ and $C = -0.00047$. The correlation coefficient R^2 in this case is 0.92, which indicates that the model provides an accurate estimate.

b) Dolomite

The dissolution of dolomite in water can be described by (Apello and Postma, 2005)

$$2\,\mathrm{CO_2(g)} + 2\,\mathrm{H_2O} + \mathrm{CaMg(CO_3)_2} \rightleftharpoons \mathrm{Ca^{2+}} + \mathrm{Mg^{2+}} + 3\,\mathrm{HCO_3^-} \qquad (2.12)$$

Similarly to calcite, CO_2 pressure influences the process and bicarbonate is formed leading to pH dependence. As dolomite is present in the reservoir with roughly the same weight percentage, a logical conclusion would be to include dolomite in the model in the same way as the calcite. However, as the dissolution of dolomite is more than an order of magnitude slower than calcite (Deynoux et al., 2004) it is neglected in the model. This will lead to a minor increase of calcite dissolution and a slightly lower Ca^{2+} concentration after all calcite has been dissolved.

2.3.3 Sorption

Sorption of ions or charged particles can take place in various ways. Sorption of ions can be both external (adsorption) and internal (absorption). When an ion that is ‘captured’ by one of these processes is replaced by a different ion, the process is called ion exchange. Figure 2.8 gives a schematic overview of the different sorption processes. Both for adsorption and absorption the reversed process is called desorption.

a) Adsorption

Clays consist of ions adsorbed layer by layer. The typical mineral formula for kaolinite is (Swaddle, 1997)

$$\mathrm{Al_2(OH)_4[Si_2O_5]} \qquad (2.13)$$

As can be seen, the formula contains two Al^{3+} ions and is therefore called aluminosilicate. If, during the formation of the clay, no aluminium ions but lower valence ions are adsorbed, a charge imbalance will occur. The charge imbalance will result in a negative surface charge of the clay. Whether or not

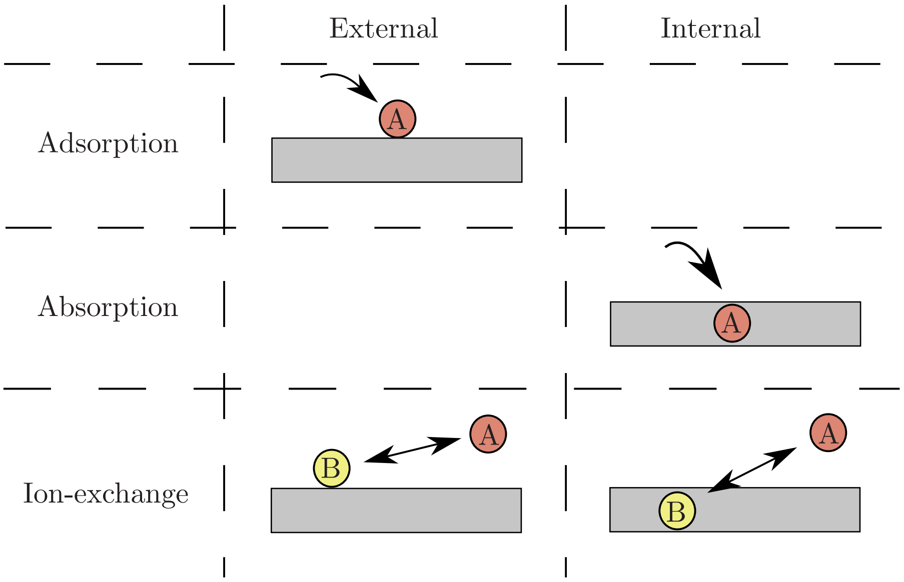

Figure 2.8: Schematic overview of sorption processes.

the clay has a negative surface charge and how much the imbalance is, depends on many factors such as the type of the clay and the depositional environment.

The negative surface charge leads to adsorption of positive charged particles and ultimately leads to the electrical double layer effect, which plays an essential role in the low salinity effect.

b) Absorption

Clays of the smectite type, such as montmorillonite, can absorb large amounts of water and are therefore also called swelling clays (Swaddle, 1997). The swelling of clays can both have positive and negative influences on the oil recovery:

- Negative: oil can be trapped due to blocked pores by the swollen clay.
- Positive: drained areas can be blocked consequently promoting new flow paths, enhancing the reservoir sweep, and thus increasing oil recovery.

The whole rock XRD data (Appendix B) shows the presence of mica, a potential swelling clay, in the formation. This has however not been taken into account, and is outside the scope of this thesis.

c) Ion Exchange

As opposed to adsorption and absorption, ion exchange is a process that takes place between two ions.

Due to the negatively charged surface of the clay, the ion exchanger will exchange positive ions between the water in the reservoir and the clay's surface. Since mainly positive ions are exchanged, the exchanger can be regarded as a cation exchanger. Upon injection of LSW, the electrochemical equilibria in the reservoir are shifted and changes in ion exchange site occupation will establish. One of the possible equilibrium reactions that takes place is

$$2\mathrm{NaX} + \mathrm{Ca}^{2+} \rightleftharpoons 2\mathrm{Na}^{+} + \mathrm{CaX}_2 \tag{2.14}$$

where X is a single negatively charged exchange site.

Upon injection of LSW, both the Ca^{2+} concentration as well as the Na^{+} concentration are lowered significantly. The new exchanger equilibrium is both a function of the solution's ionic strength and relative concentrations of individual ions.

In the next chapter, simulations will be run to investigate the behavior of the ion exchanger during LSW injection. The main ions involved in this process are sodium, calcium and magnesium. These are all positive ions with valence plus one or plus two.

2.4 Buckley-Leverett Modeling

As far back as 1942, Buckley and Leverett presented their famous transport equation in the paper ‘Mechanism of Fluid Displacement in Sands’ (Buckley and Leverett, 1942). This equation is now recognised as the basic way of describing immiscible displacement. This section will cover the basics and important assumptions behind the Buckley-Leverett equation. Implications for low salinity water flooding regarding the Buckley-Leverett solution are covered in Section 2.4.2.

2.4.1 Basics

Production of oil using an artificial water drive is very common all over the world. For the simple scenario in which a single injector-producer well pair is regarded, the Buckley-Leverett equation can be used to model the oil-water two-phase flow.

Figure 2.9 illustrates the schematic situation under consideration. Water is being injected in the left well (injector) and is pushed to the right well (producer). The following modelling assumptions are made:

- The horizontal reservoir layer of length L has a constant thickness H where $H \ll L$.
- The layer is bounded by impermeable layers above and below.
- Both the rocks and fluids are considered incompressible.

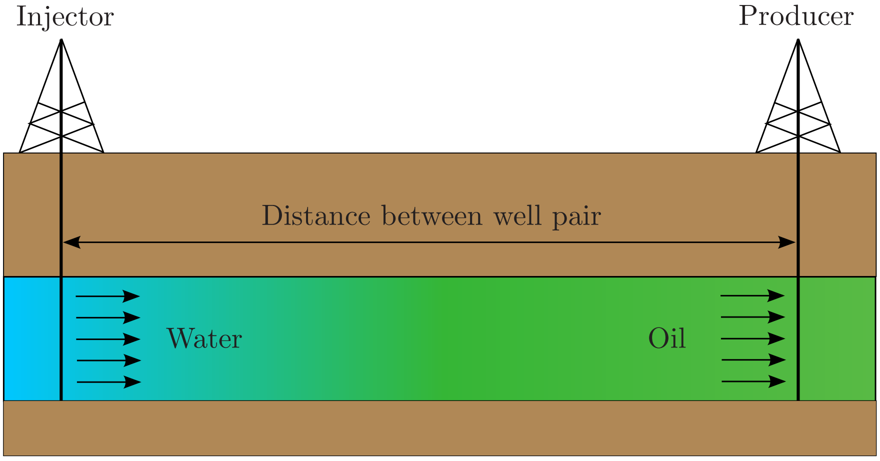

Figure 2.9: Schematic illustration of the Buckley-Leverett well pair. On the left side a water injector and on the right side the oil producer is drawn.

- The porosity and absolute permeability are constant.
- Water and oil flow are independent from each other and obey Darcy's law.
- Capillary forces are negligible.
- Gravity forces are negligible.
- The pressure is a function of the x-coordinate only, which makes the problem one-dimensional.
- The total flow rate q_t is constant throughout the whole reservoir length, which implies that the injection rate is also constant and $q_t = q_w$ must hold at the injector.

The Buckley-Leverett equation can be derived from a simple mass balance (Dake, 1978),

$$\text{mass in - mass out} = \text{rate of mass change} \tag{2.15}$$

or written as

$$q_w \rho_w \bigg|_x - q_w \rho_w \bigg|_{x+dx} = A\phi dx \frac{\partial}{\partial t}\left(\rho_w S_w\right) \tag{2.16}$$

where q_w is the volume of water flowing in or out the volume element, ρ_w the density of water, A the reservoir area of the section perpendicular to the direction of flow, ϕ the porosity and S_w the water saturation in the volume element. Figure 2.10 illustrates the mass balance over a single volume element in the reservoir. Fluctuations in the water density are often small and can therefore be neglected, leading to

$$q_w \bigg|_x - q_w \bigg|_{x+dx} = A\phi dx \frac{\partial S_w}{\partial t} \tag{2.17}$$

Equation 2.17 can be expanded to

$$q_w \bigg|_x - \left(q_w \bigg|_x + \frac{\partial q_w}{\partial x} dx \right) = A\phi dx \frac{\partial S_w}{\partial t} \tag{2.18}$$

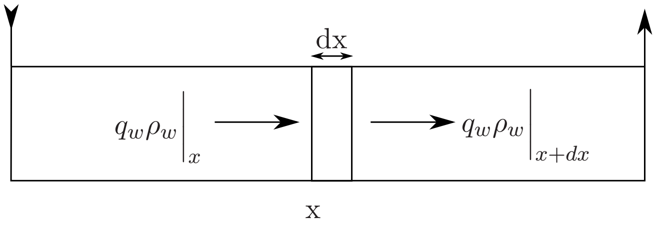

Figure 2.10: Mass balance in Buckley-Leverett equation. Redrawn after Dake (1978).

which in turn can be rewritten as

$$-\frac{\partial q_w}{\partial x}dx = A\phi dx\frac{\partial S_w}{\partial t} \tag{2.19}$$

By bringing all terms to the LHS and dividing by dx, Equation 2.19 becomes

$$A\phi\frac{\partial S_w}{\partial t} + \frac{\partial q_w}{\partial x} = 0 \tag{2.20}$$

As incompressible flow of oil and water is assumed, it must hold that the total combined flow is equal to the sum of both the oil and water flow. Consequently the flow of water is equal to the total flow times the fractional flow of water, that is

$$q_w = q_t f_w = Auf_w \tag{2.21}$$

where u is the Darcy velocity and f_w is the fractional flow of water. Combining both Equations 2.20 and 2.21, and dividing both terms by A, results in the Buckley-Leverett equation as written in its common form

$$\phi\frac{\partial S_w}{\partial t} + u\frac{\partial f_w}{\partial x} = 0 \tag{2.22}$$

Mind that this is only possible when the Darcy velocity is constant, which means that the injection rate must be constant.

The typical solution for Buckley-Leverett flow is schematically illustrated in Figure 2.11 for the situation where no water breakthrough has yet occurred at the producer.

Upon injection of water, assumed as being equal in salinity as the formation water for this purpose, a single shock front will establish in the reservoir. Until water breakthrough has occurred, only oil will be produced. The oil production rate will be constant and equal to the injection rate, as long as no water breakthrough has occurred.

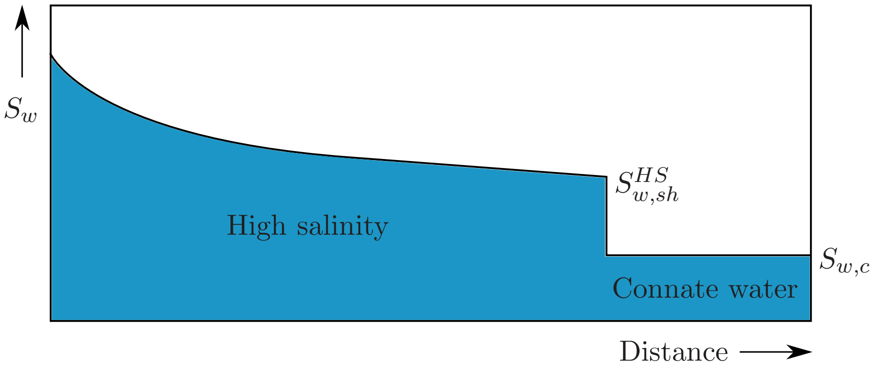

Figure 2.11: Typical Buckley-Leverett solution for HS flooding.

At the time of water breakthrough, the shock front arrives at the producer. The water cut will suddenly rise from zero to

$$f_w = \frac{S_{w,sh}^{HS}}{1 - S_{w,c} - S_{o,r}^{HS}} \tag{2.23}$$

where $S_{w,c}$ is the connate water saturation, $S_{o,r}^{HS}$ the residual, or irreducible, oil saturation at high salinity conditions and $S_{w,sh}^{HS}$ the shock front saturation at high salinity conditions.

After water breakthrough, water and oil will be co-produced and the fraction of water will steadily rise. Consequently, the fraction of oil in the produced fluids decreases over time.

When the fraction of oil becomes too small to be economically produced, the well will be shut-in. Large quantities of oil will still be left in the reservoir, which are an interesting target for EOR methods such as low salinity water flooding.

2.4.2 Low Salinity Flooding Modelling

As discussed in Section 2.2, several low salinity mechanisms are proposed, but a unified -and widely accepted- theory has not yet been formulated. To model the low salinity effect, a change in relative permeability model is assumed, as was done in previous work (Jerauld et al., 2006a,b). A relative permeability model more favourable to oil displacement is used in areas of the reservoir that are flooded with low saline water.

The change in relative permeability can be implemented in the Buckley-Leverett transport equation. By modelling the relative permeability as both a function of the water saturation and the salinity, the solution of the Buckley-Leverett equation becomes more complex. It is however still possible to construct an analytical solution similar to the one derived for polymer flooding by Pope (1980). In this thesis, only a numerical solution method will be used. The full derivation of the numerical model will be given in Chapter 4.

Earlier work regarding modelling low salinity water flooding by using Buckley-Leverett theory indicates that the solution shows much different behavior than with ordinary water flooding (Jerauld et al., 2006b). In addition, significant differences occur for secondary and tertiary injection modes.

When low salinity water flooding is used in secondary mode, no water has been injected into the reservoir prior to the low salinity water. Figure 2.12(a) shows the typical Buckley-Leverett solution for secondary mode flooding, the dashed line shows the classic Buckley-Leverett profile from Figure 2.11 as a reference. A distinct difference between the classic Buckley-Leverett solution

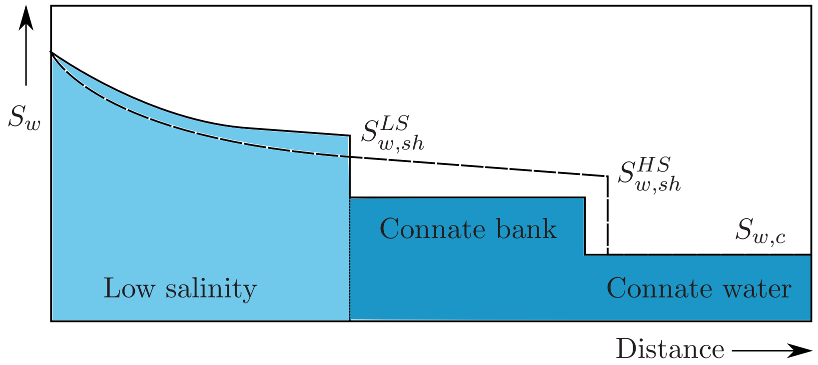

(a) Secondary mode

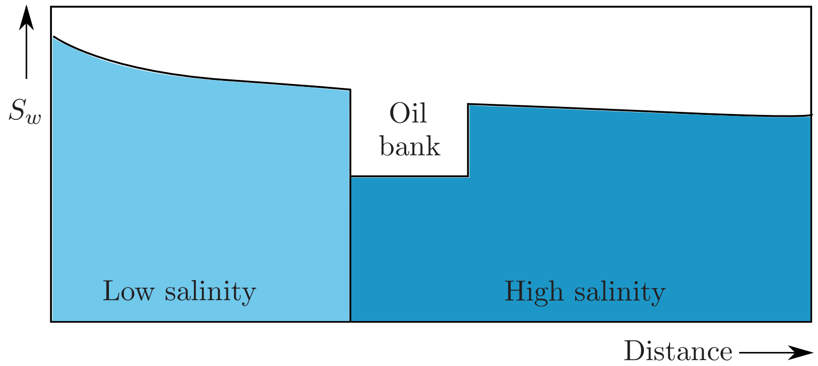

(b) Tertiary mode

Figure 2.12: Expected behavior for low salinity flooding modelled by the Buckley-Leverett equation. Redrawn after Pope (1980).

and the solution for secondary mode low salinity water flooding is the two-shock front.

The first shock observed at a producer is caused by a connate water bank that is pushed in front of the low salinity water, a process called connate water banking. This bank of connate water will be at a constant water saturation somewhere between the connate water saturation $S_{w,c}$ and the low salinity shock front saturation $S_{w,sh}^{LS}$. The second shock is observed at the producer when the low salinity water reaches the producer. This will increase the water saturation from the connate banking saturation to the low salinity shock saturation $S_{w,sh}^{LS}$. The low salinity shock saturation $S_{w,sh}^{LS}$ will be higher than the high salinity shock front saturation $S_{w,sh}^{HS}$, which indicates the higher recovery potential of the low salinity water. The constant saturation for connate water banking and the two-shock result has also been observed in the field (Vledder et al., 2010).

Most often, low salinity water flooding is used as a method to increase the oil recovery from an already water flooded field. If this is the case, the mode of operation is said to be tertiary. In tertiary mode, the Buckley-Leverett solution shows a different behavior due to the already high water saturations of high salinity water in the field. Figure 2.12(b) shows the typical solution for tertiary mode low salinity water flooding.

During tertiary mode, an oil bank will form in front of the low salinity water slug. As the low salinity water increases the relative permeability to oil, the oil will flow better and accumulate just in front of the low salinity slug to form an oil bank. This happens because the relative permeability to oil in the high salinity water is still unfavourable to oil displacement.

When the oil bank reaches the producer, the water cut will drop and remain constant for the duration of the oil bank production. After the oil bank is produced, the water cut at the producer increases again. This increase coincides with the low salinity water breakthrough (Jerauld et al., 2006a,b).

Chapter 3

PHREEQC Simulations

The goal in this chapter is to investigate the ion speciation in the aqueous phase and the cation exchanger's composition upon injection of low salinity water (LSW). Therefore, we are concerned with the evolution of the concentration of all ions in solution and those attached to the clay surface in space and time.

To gain understanding of geochemical interactions in the case study field upon injection of water, a large set of equilibrium and transport equations are to be solved simultaneously. Solving the system of highly non-linear equations involved, typically is practically impossible. Therefore, the PHREEQC geochemical simulator is used.

The first section of this chapter covers the basic simulation setups used throughout the chapter. The remainder of this chapter will describe the simulations performed to investigate CO_2 buffering, calcite dissolution, cation exchange and mixing, and their respective results.

3.1 Simulation Setups

The U.S. Geological Survey (USGS) package PHREEQC is a geochemical simulator for speciation, batch-reaction, one dimensional transport and inverse geochemical calculations. PHREEQC version 2.18 was used for all simulations throughout this chapter.

A great advantage of PHREEQC is that is contains extensive general databases of geochemical data. In this thesis the default database *phreeqc.dat*, last updated in November 2010, was used.

To aid in writing the simulations, use has been made of the PHREEQC for Windows tool, version 2.18. Although it is possible to use this tool to visualize simulation results, the possibilities are limited. Hence, extensive use has been made of MATLAB® R2012a to read, process and display simulation results.

In this chapter two types of simulations will be carried out. The first type involves equilibrium calculations for water in contact with rock. The second type concerns water transport in a 1D aquifer including geochemical interactions. A detailed description for both setups will be given in the remainder of this section.

3.1.1 Equilibrium Calculations

The equilibrium calculations are performed on a single tank filled with rock and water, no transport of water is included. By default all quantities in PHREEQC need to be specified relative to one kilogram of water.

Figure 3.1 illustrates the single tank setup used in the equilibrium calculations. The system border illustrates that no flow can go in or out of the tank. Mind that this representation is purely indictional for the interactions, as the model has no spatial dimensions.

Various geochemical interactions such as cation exchange, calcite dissolution and CO_2 buffering can be included. Note that not all geochemical interactions are taken into account in all simulations. The effects taken into account in each simulation will be specified clearly at the beginning of each section.

Equilibrium calculations do not include kinetics, that is, only the final equilibrium is calculated, disregarding the time that is needed to reach the particular state.

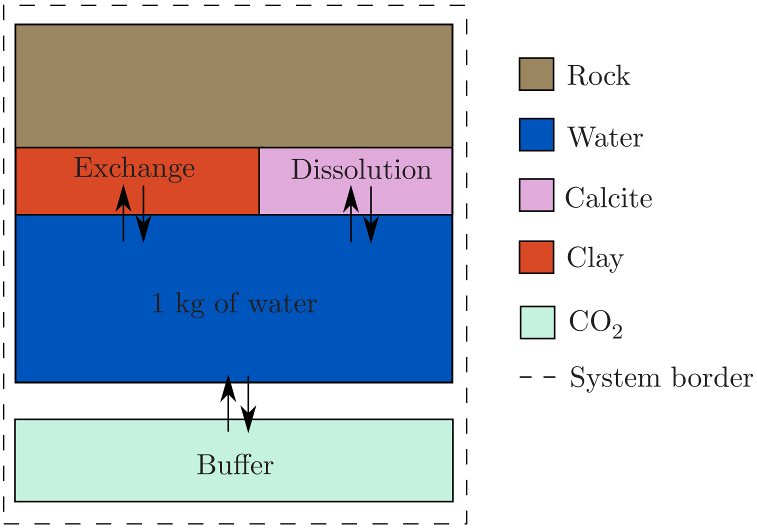

Figure 3.1: Schematic representation of equilibrium calculation setup.

3.1.2 Fluid Flow Simulations

The transport simulations are based on a series of tanks similar to the one defined for the equilibrium calculations. Figure 3.2 illustrates the tank that represent a single grid cell in a transport simulation.

Again, various geochemical interactions are modelled. Two important differences however must be noted. Firstly, the model includes kinetics for the calcite dissolution process. Secondly, transport of water is now included in the model, which means that the system border of a single grid cell is not closed anymore between time steps.

Figure 3.3 shows the basic model for all PHREEQC transport simulations in this thesis. No detailed rock interactions have been drawn in this figure. The interactions are however equal to those of Figure 3.2.

A reservoir with length of 800 m is considered, as it represents a typical injector-producer inter-well distance in the sector of interest in the case study field. The reservoir is divided into 100 grid cells, resulting in a grid cell length of 8 m. PHREEQC uses a cell centered approach for the numerical solution and therefore the position of x_i is $4 + 8 \cdot (i - 1)$ m. One extra grid cell is added in front of the column and will hold the injection water. Hence, the total number of grid cells is 101.

In all simulations, all 100 reservoir grid cells are initially filled with 1 kg of formation water (FW). In addition, the injection fluid grid cell is also filled with FW. Detailed compositional information on FW and all other water types used in the simulations can be found in Appendix C.

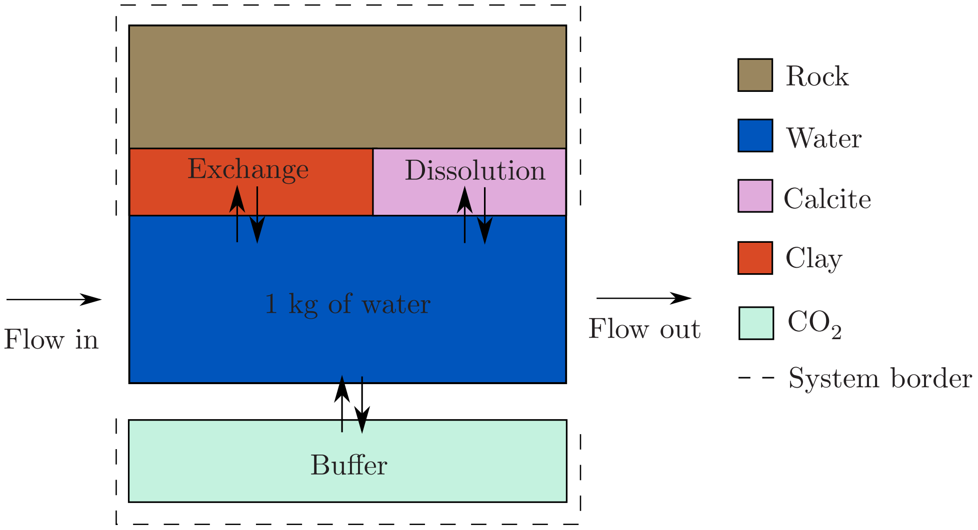

Figure 3.2: Schematic representation of a single grid cell in transport simulations.

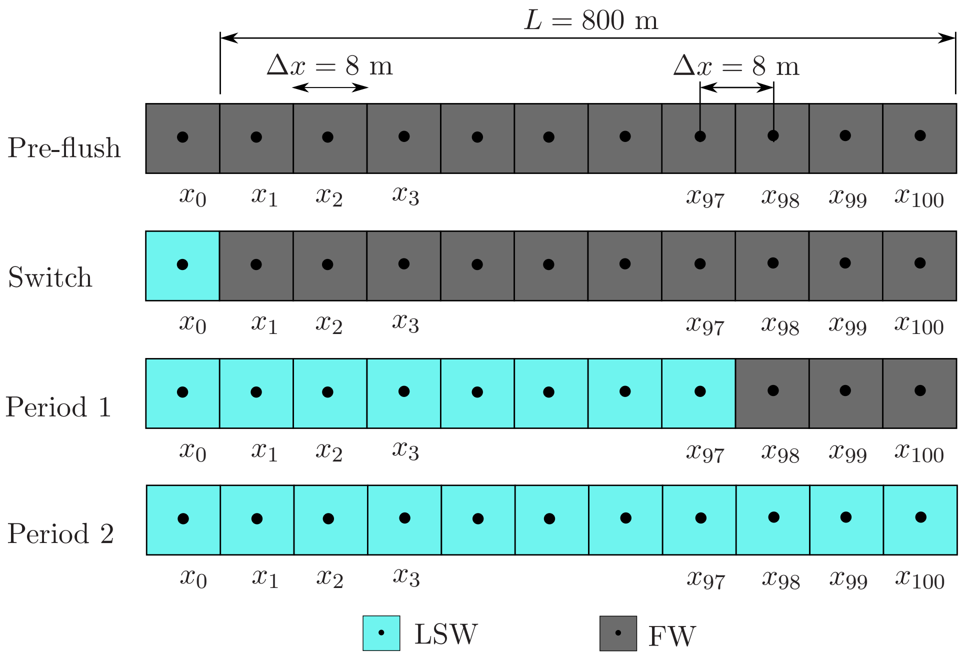

Figure 3.3: Schematic overview of 1D simulation grid during different stages of injection. For simplicity, the rock interactions have not be drawn in this figure.

Depending on the investigated interactions, the rock properties in the reservoir grid cell 1-100 are defined. In the zeroth grid cell no rock is defined. To ensure that a consistent setup has been build, 1.0 PV of FW is flushed through the reservoir prior to switching to LSW. During this pre-flush no changes in ion composition, exchanger occupation or amount of calcite should occur.

When exactly 1.0 PV of FW has been flushed through the reservoir the injector fluid containing grid cell is changed from holding FW to LSW (or any other injection fluid of interest).

Initially, no dispersion is modelled in the system which will result in a sharp border between the injection fluid and the FW. After exactly 100 *shifts*, or 1.0 PV of LSW, all FW will have been displaced.

3.2 Calcite Dissolution

In this section the influence of calcite in the reservoir, during the injection of LSW, is investigated. Firstly, the amount of calcite in the grid cell is calculated and modelled. Secondly, the Ca^{2+} equilibrium concentration is calculated. Thirdly, a transport simulation is carried out to study the behavior of kinetic calcite dissolution.

3.2.1 Model Parameters

From the available PVT data of the reservoir fluid (Appendix A) the average CO_2 content $\mu_{CO_2} = 0.927\%$, average reservoir pressure $P_r = 248.0$ bara, and average temperature $T = 85$ °C were determined. Using Equation 2.8 the CO_2 pressure can be calculated by filling in the CO_2 content, reservoir pressure and fugacity coefficient $f = 0.65$. This results in $P_{CO_2} = 1.38$ atm.

The available measurements for the CO_2 content show significant variability. The uncertainty in CO_2 pressure is taken into account by setting an upper and lower limit for the CO_2 content. These limits are defined as $\mu_{CO_2} \pm 2 \cdot \sigma_{CO_2}$ where $\sigma_{CO_2} = 0.206\%$ is the sample standard deviation of the CO_2 content. The resulting uncertainty span includes all CO_2 content measurements from Appendix A.

The initial amount of calcite has been estimated to be an average of 0.943 mol/kgw (see Appendix B). High and low values are 1.39 mol/kgw and 0.50 mol/kgw, respectively. The rate at which calcite dissolves is assumed to be 10^{-6} mol/(m$^2\cdot$ s). This is around a 100 times slower than the estimate obtained from Equation 2.11. Calcite dissolution is a very fast process, and even by using this conservative estimate, instantaneous equilibrium is a valid assumption. A specific reaction surface for calcite of 0.01 m^2/g is taken from Hellevang and Aagaard (2011).

Table 3.1: Calcite dissolution simulations base model parameters

Description	Units	Value
CO_2 pressure	atm	1.38
Initial amount of calcite	mol/kgw	0.943
Flow velocity	m/y	200
Calcite dissolution rate	mol/(m$^2\cdot$s)	10^{-6}
Specific reaction surface of calcite	m^2/g	0.01
Temperature	°C	85

The ECLIPSE® reservoir model of the case study field has been used to estimate the average flow velocity between the well pair of interest. Results determined ranged from 50 m/y to around 200 m/y. As the calcite dissolution rate is fast enough to fully equilibrate with a grid cell in one time step in both the high and low velocity situations, the results of this simulation are not impacted (only the timescale changes). For all simulations in this thesis the highest flow rate of 200 m/y was used.

An overview of the calcite dissolution model parameters can be found in Table 3.1.

3.2.2 Equilibrium Ca^{2+} Concentration

The partial pressure of carbon dioxide (CO_2) in the reservoir plays a crucial role in the carbonic acid equilibria, and consequently on the calcite dissolution. This was discussed in Section 2.3.1 and 2.3.2, respectively.

Initially, the formation water is in equilibrium with both carbon dioxide and rock. Injecting low salinity water will disrupt this equilibrium. The LSW will form a new equilibrium with both the carbon dioxide and rock leading to calcite dissolution. The amount of calcite that dissolves depends on the CO_2 pressure in the reservoir and the composition of the injected LSW.

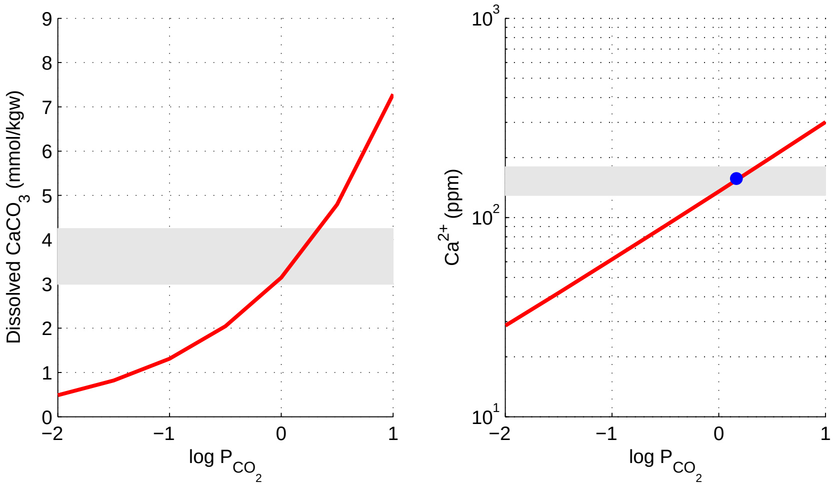

(a) Calcite dissolution

(b) Calcium concentration

Figure 3.4: Figure 3.4(a) shows the amount of calcite that can be dissolved in 1 kg of LSW. The resulting Ca^{2+} concentration as a function of the logarithm of the CO_2 pressure is shown in Figure 3.4(b). In both plots the shaded area represent the resulting uncertainty interval due to the uncertainty in the CO_2 pressure. The blue dot is an estimate for the CO_2 pressure on the NCS at the case study field's reservoir temperature after Smith and Ehrenberg (1989).

Figure 3.4(a) shows the amount of dissolved calcite per kilogram pore water as a function of the CO_2 pressure. Figure 3.4(b) shows the Ca^{2+} concentration as a function of the CO_2 pressure.

The average value for the CO_2 pressure results in an amount of 3.7 mmol dissolved calcite per kilogram water. This results in an equilibrium Ca^{2+} concentration of 160 ppm. In the remainder of this thesis the average CO_2 pressure is used.

In both figures the resulting uncertainty span due to the uncertainty in CO_2 pressure is marked by the shaded area. The calculated minimum amount of dissolved calcite is 3.0 mmol. The upper limit of the uncertainty span is 4.2 mmol. The Ca^{2+} concentration's upper and lower bounds are 130 ppm and 180 ppm, respectively. Even though a wide uncertainty range for the CO_2 pressure was used, the resulting uncertainty span in the Ca^{2+} concentration is only about $\pm 20\%$.

The blue dot in Figure 3.4(b) is an estimate of the Ca^{2+} concentration for the CO_2 pressure on the NCS at the reservoir temperature after Smith and Ehrenberg (1989). This literature value is in good agreement with the estimated values of the CO_2 pressure for case study field.

3.2.3 Calcite Dissolution during Fluid Flow

An important goal in low salinity water flooding is to reduce the amount of double valence ions, such as Ca^{2+}, in the solution. This will lead to an increase of the electrical double layer thickness, as described in Section 2.2. To accomplish this, the injected LSW typically contains only traces of double valence ions. The LSW as defined in the simulations does not contain any double valent ions, see Appendix C.

Due to the low double valent ion concentration, the LSW will disturb the solubility equilibrium of calcite. Calcite will dissolve to counteract the reduction in Ca^{2+} ions below the Ca^{2+} equilibrium concentration.

Although LSW without double valent ions is injected, a non-zero concentration of Ca^{2+} will be established in the aqueous phase in the reservoir. A Ca^{2+} concentration of zero in the aqueous phase in the reservoir, which is only possible in theory, will only happen if all the calcite in a grid cell has been dissolved.

Figure 3.5 shows the results of PHREEQC simulations where LSW dissolves calcite in the first grid cell. In Figure 3.5(a) the total amount of calcite in the grid cell is plotted. At each time step the freshly injected LSW is saturated with Ca^{2+} from the calcite leading to a linear reduction of the amount of calcite. After injecting slightly over 2.2 PVs, all the calcite in the first grid cell is dissolved.

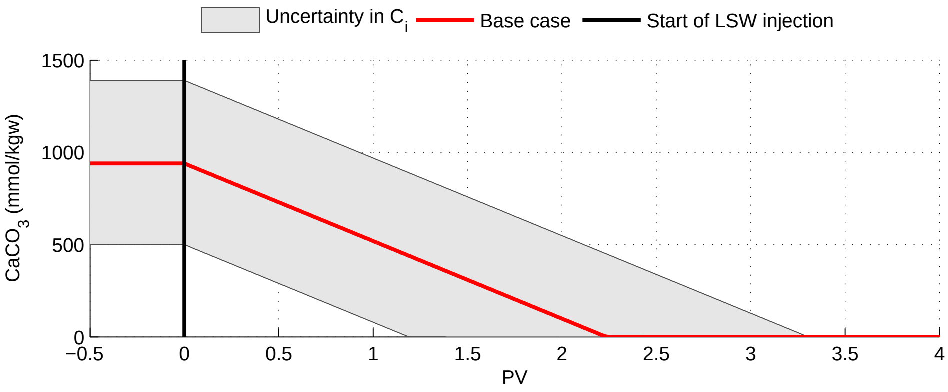

(a) Calcite dissolution

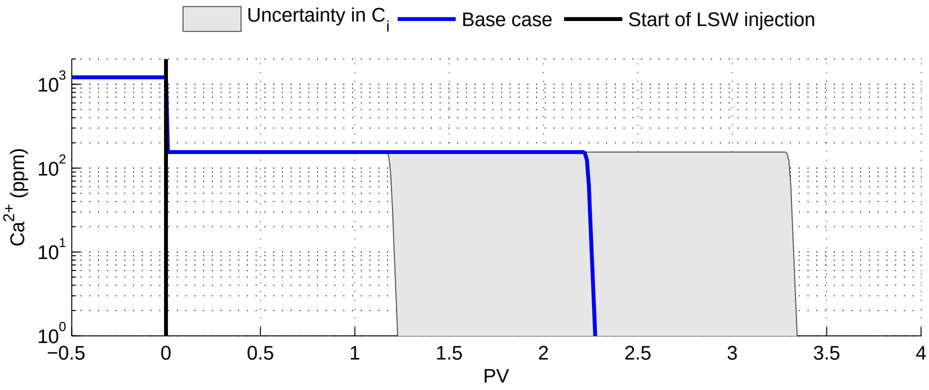

(b) Calcium concentration

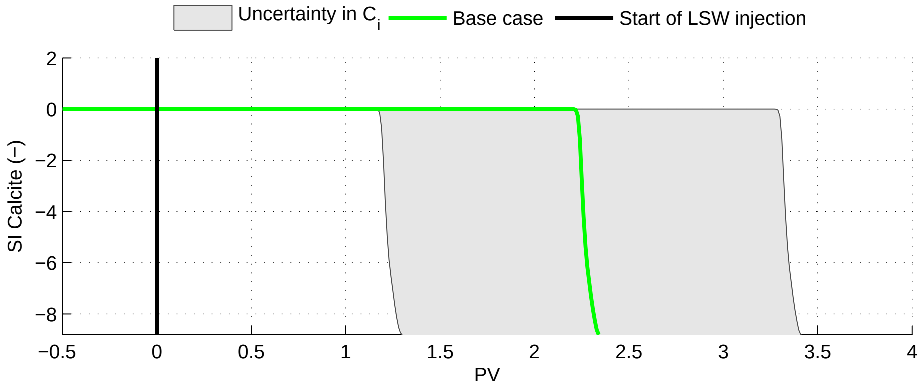

(c) Calcium saturation index (SI)

Figure 3.5: Results for calcite dissolution simulations. Figure 3.5(a) shows the amount of calcite in the first grid cell (i.e., $CaCO_3$ in mmol/kgw) as a function of the injected PVs. In Figure 3.5(b) the corresponding Ca^{2+} concentration is plotted. Figure 3.5(c) shows the saturation index for calcite as a function of injected PVs.

Figure 3.5(b) shows the Ca^{2+} concentration in the first grid cell as a function of the amount of PVs injected. Initially the Ca^{2+} concentration is equal to the FW level, as it should be. When injection starts, the Ca^{2+} concentration drops to 160 ppm. This is equal to the determined equilibrium concentration in Section 3.2.2. The Ca^{2+} concentration remains constant throughout the process of dissolving calcite. Only after all calcite has been dissolved, the Ca^{2+} is completely removed from the solution. The saturation index, which is plotted in Figure 3.5(c), shows clearly that the calcite equilibrium can be reached ($SI = 0$), even for the conservative dissolution rate used in the simulation.

As LSW equilibrates with both the CO_2 and calcite in the first grid cell, no significant changes in concentration will occur in the second grid cell, and onward, until all calcite from the first grid cell has been dissolved. Calcite will therefore dissolve throughout the reservoir in a plug-flow fashion.

Dissolving all calcite in the first grid cell already required more than 2 PV of LSW. It is therefore unlikely that all calcite in the reservoir can be dissolved during the lifetime of a LSW project.

Figure 3.6 shows the sodium, calcium and magnesium concentrations in the first grid cell as functions of the injected PVs. As no Mg^{2+} is present in the injection water, nor a source of Mg^{2+} is present in the simulated reservoir, the Mg^{2+} concentration drops to zero directly after the start of LSW injection. The Na^{+} concentration drops from the FW level to the LSW level and remains constant afterwards. Only the Ca^{2+} concentration and pH are influenced by the calcite in the reservoir.

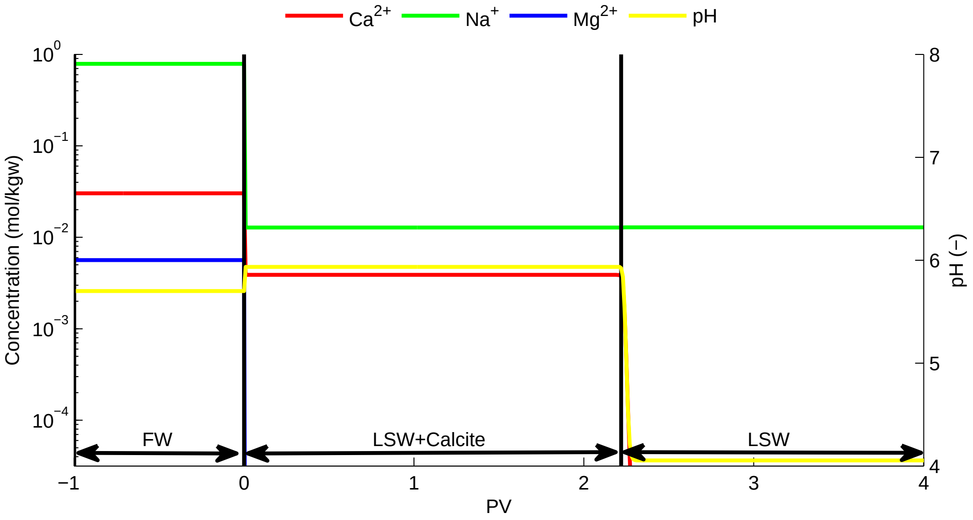

Figure 3.6: Evolution of the ion concentrations in the first grid cell of the model for a simulation including CO_2 and calcite dissolution.

3.3 Ion Exchange

In this section, the effects of ion exchange on the ion concentrations in the reservoir during LSW injection are investigated. First of all, the amount of exchanger sites is calculated and modelled. Next, the exchanger equilibrium behavior is studied. Finally, a transport simulation is carried out to study the effect of ion exchange during aquifer fluid flow in combination with calcite dissolution.

3.3.1 Model Parameters

Negatively charged clay surfaces, due to imperfections in the clay lattice, give rise to cation exchange. Also in the case study field, negatively charged clay's occur.

The cation exchange capacity (CEC) of the formation were calculated by both using the weight percentages of clay and the estimates for typical minimum and maximum CEC for specific rock types taken from Apello and Postma (2005). Appendix B gives an overview of the CEC for each rock type in the formation of the case study field.

By summing up all individual CECs for each rock type the total average CEC for the formation was calculated. These calculations resulted in an estimate for the minimum, base case and maximum number of exchange sites kilogram of pore water. That is, 0.2 mol, 0.45 mol and 0.7 mol exchange sites, respectively.

Other model parameters are equal to those specified in Section 3.2.1. Table 3.2 sums up the model parameters.

Table 3.2: Ion exchange simulations base model parameters

Description	Units	Value
CO_2 pressure	atm	1.38
Initial amount of calcite	mol/kgw	0.943
Flow velocity	m/y	200
Calcite dissolution rate	$mol/(m^2 \cdot s)$	10^{-6}
Specific reaction surface of calcite	m^2/g	0.01
Temperature	°C	85
Exchanger sites	mol/kgw	0.45

3.3.2 Exchanger Equilibrium Behavior

Three equilibrium simulations were performed to study the exchanger's equilibrium behavior. In the first simulation (a) FW is diluted with deionized water to see the effect of ionic strength on the exchanger occupation. In the second simulation (b) the ionic strength is kept constant while the Na^+/Ca^{2+} ratio is varied. Finally, (c) the exchanger occupation is investigated for a grid cell filled with LSW with varying concentrations of Ca^{2+}.

a) Dilution of Formation Water

In this simulation it is investigated how the ion exchanger's composition is influenced by lowering the ionic strength of a solution. This was done because LSW has a significantly lower ionic strength than FW.

FW in equilibrium with 0.45 mol cation exchanger sites and CO_2 is diluted by means of deionized water. No calcite is added to the system such that no extra Ca^{2+} is introduced when the ionic strength of the solution is lowered. The pH is kept at initial reservoir conditions, that is pH $= 5.7$.

Figure 3.7(a) shows the relative ionic strength I^r and relative exchanger composition as a function of the fraction of deionized water in FW. The ionic strength is plotted with respect to the initial ionic strength of FW. The relative

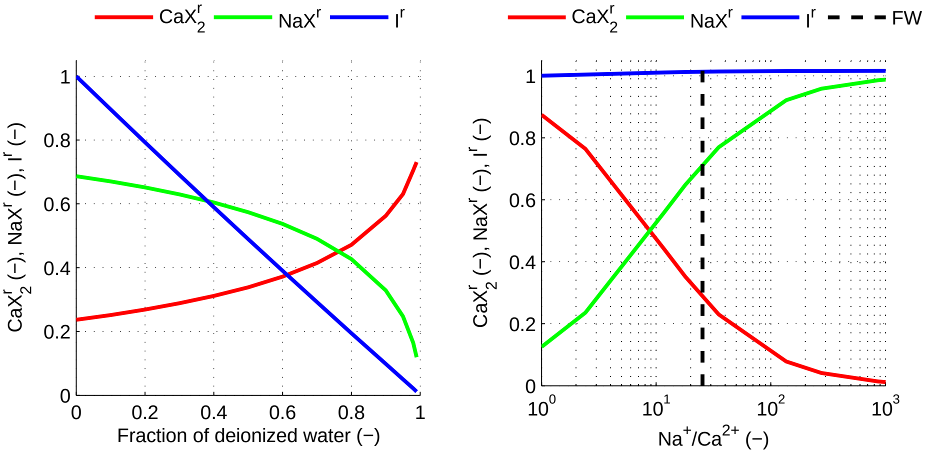

(a) Diluting FW (b) Varying Na^+/Ca^{2+} ratio

Figure 3.7: Relative exchange site occupation under dilution and varying Na^+/Ca^{2+} ratio. Figure 3.7(a) shows the behavior of the exchanger's composition under the influence of a decreasing ionic strength. Figure 3.7(b) shows the exchanger's behavior under varying Na^+/Ca^{2+} ratio at constant ionic strength. The dashed line in Figure 3.7(b) represents the in-situ FW conditions.

exchanger occupation CaX_2^r for calcium and NaX^r for sodium are relative to the total number of exchange sites.

Results indicate that upon lowering the ionic strength of the solution, while keeping the ratio Na^+/Ca^{2+} constant, the amount of Ca^{2+} ions attached to the exchanger increases. This behavior is due to the valence difference between calcium (+2) and sodium (+1).

b) Varying Na^+/Ca^{2+} ratio

The relative amount of ions attached to the exchanger is not only a function of the ionic strength, also the ratio between the ions in solution plays an important role. In this section, the influence of the Na^+/Ca^{2+} ratio on the composition of the exchanger is investigated. This was done because during the injection of LSW the Na^+/Ca^{2+} ratio changes.

In this simulation, only Ca^{2+}, Na^+ and Cl^- were taken into account. The cation exchanger is equilibrated with solutions with varying Na^+/Ca^{2+} ratio for a constant ionic strength in the presence of CO_2. The Cl^- concentrations and pH were kept constant at reservoir conditions. No calcite was added to the system.

Figure 3.7(b) shows the results of this simulation. The relative ionic strength is defined with respect to the ionic strength of FW (only for the ions under consideration). The exchanger composition is again relative to the total number of exchange sites.

The results show that the cation exchange composition and the Na^+/Ca^{2+} ratio are strongly correlated. For an increasing Na^+/Ca^{2+} ratio, Na^+ becomes more abundant than Ca^{2+}, which results in a larger number of cation exchange sites being filled up with Na^+. For a decreasing Na^+/Ca^{2+} ratio the opposite happens.

c) Exchanger Equilibrium for a Varying Ca^{2+} Concentration

In this section the behavior of the cation exchanger is investigated under influence of a changing Ca^{2+} concentration in LSW. This is done to get insight in the exchanger's composition when all calcite in (a section of) the reservoir has been dissolved.

When LSW is injected into the reservoir, calcite is dissolved and consequently the Ca^{2+} concentration in the LSW rises. When the Ca^{2+} equilibrium has reestablished, at a Ca^{2+} concentration of 160 ppm, the Na^+/Ca^{2+} ratio has decreased compared to the Na^+/Ca^{2+} ratio in FW. From (b) it is clear that this will lead to a higher occupancy of the cation exchange sites by Ca^{2+}.

At the same time, the LSW also has a lower ionic strength compared to

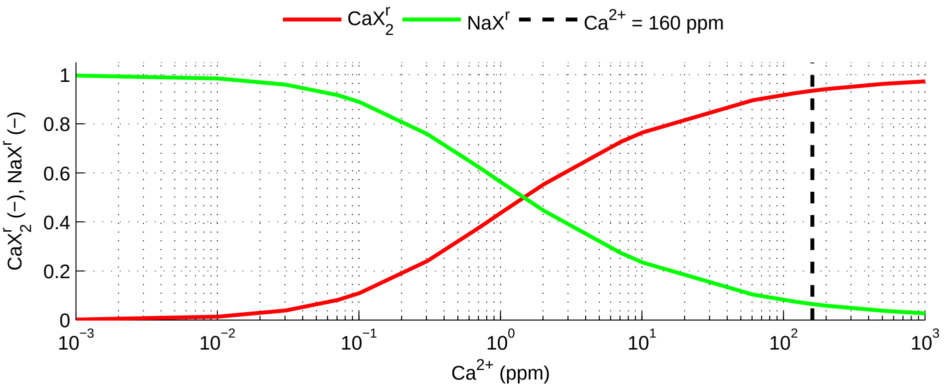

Figure 3.8: Relative exchanger composition in LSW for various Ca^{2+} concentrations. The vertical dashed line shows the exchanger composition during LSW when calcite is present in the reservoir.

FW which also leads to an increase in Ca^{2+} to the exchanger, as discussed in (a).

Figure 3.8 shows the relative composition of the exchanger in LSW as a function of the Ca^{2+} concentration. At a Ca^{2+} concentration of 160 ppm, the calcium equilibrium concentration in LSW, the majority of the cation exchanger sites will be occupied by Ca^{2+}. This is in line with the results from (a) and (b).

When all calcite has been dissolved no Ca^{2+} equilibrium with solid calcite will establish anymore. That is, no Ca^{2+} is being introduced in the solution anymore by means of calcite dissolution.

Note that by having removed all the calcite from the reservoir the Na^+/Ca^{2+} ratio can become larger again, indicating towards a high concentration of Na^+ on the exchanger. At the same time the ionic strength is still low, making the attachment of Ca^{2+} to the exchanger favourable. The studied mechanisms seem to point in different directions.

In the situation that all calcite has been dissolved, the equilibrium with the cation exchanger's composition is again disturbed. Ca^{2+} will be detached from the exchanger and go into the solution. This in turn increases the Ca^{2+} concentration in the solution. From Figure 3.8 it is clear that very low concentrations of Ca^{2+} in solution (a few parts per million) are sufficient to maintain high concentrations of Ca^{2+} attached to the exchanger.

By continuously flooding with LSW eventually all Ca^{2+} will be removed from the exchanger (if no Ca^{2+} is present in the LSW). However, many PVs of LSW are needed. In the next section a transport simulation is performed to further study this behavior.

3.3.3 Exchanger Effects during Fluid Flow

The simulation carried out in this section is equal to the one performed in Section 3.2.3, with the addition of cation exchange.

As already mentioned, flushing the reservoir with LSW results in the grid first cell becoming undersaturated with respect to calcite. This leads to calcite dissolution. However, some of the Ca^{2+} released from dissolution is attached to the cation exchanger and consequently this leads initially to faster calcite dissolution compared to the case without cation exchange. In Figure 3.9(a) this is clearly visible for the nonlinear calcite dissolution between 0.0 and 0.2 PV of injected LSW.

After injection about 0.2 PV the new exchanger equilibrium has been reached, and no additional calcite will be dissolved anymore. The total calcite dissolution rate from that moment onward is again equal to the non-exchange situation. Due to the initial extra calcite dissolution the calcite in the first grid cell can be dissolved fully in approximately 2.0 PV, which is slightly less than in the case without cation exchange.

Figure 3.9(b) shows that the first grid cell remains undersaturated with respect to Ca^{2+} during the time the exchanger adsorbs Ca^{2+} ions. The uncertainty bands plotted in the same figure show that for an increase in amount of exchanger sites the duration of the initial extra calcite dissolution becomes longer. When the CEC is largest, the time needed to fully dissolve calcite is smallest.

Due to the large initial dissolution of calcite, the carbonate species in the reservoir fluid increases. This leads to an increase in the pH, see Figure 3.9(c). This is however just an initial effect. The pH swiftly reverts back to the non-exchange case after around 0.3 PVs have been injected into the reservoir.

Figure 3.10 shows the ion concentrations, cation exchange composition, and pH as a function of the injected PVs in the first grid cell. Initially, during in-situ FW conditions, the cation exchange sites are mostly occupied by Na^+. This is due to the fact that Na^+ is around 25 times as abundant in FW compared to Ca^{2+}.

Upon injecting LSW into the reservoir the ionic strength diminishes, promoting the adsorption of Ca^{2+} on the cation exchanger. In addition, the injected concentration of Na^+ is almost 60 times smaller, whereas due to calcite dissolution the new Ca^{2+} concentration is only 7.5 times smaller compared to the FW case. This leads to a decrease in the Na^+/Ca^{2+} ratio from initially being 25 to approximately 3, which also promotes Ca^{2+} adsorption on the exchanger. This is reflected in the results which show a significant shift to Ca^{2+} being attached to the exchanger sites, and large amounts of Na^+ being released from the ion exchanger.

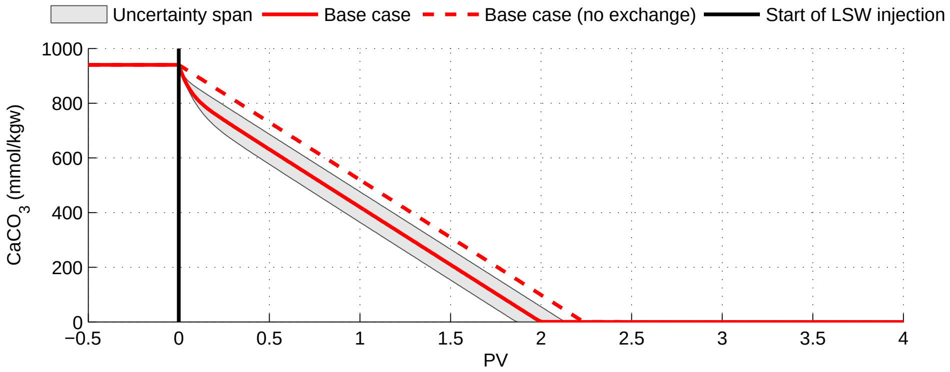

(a) Calcite dissolution

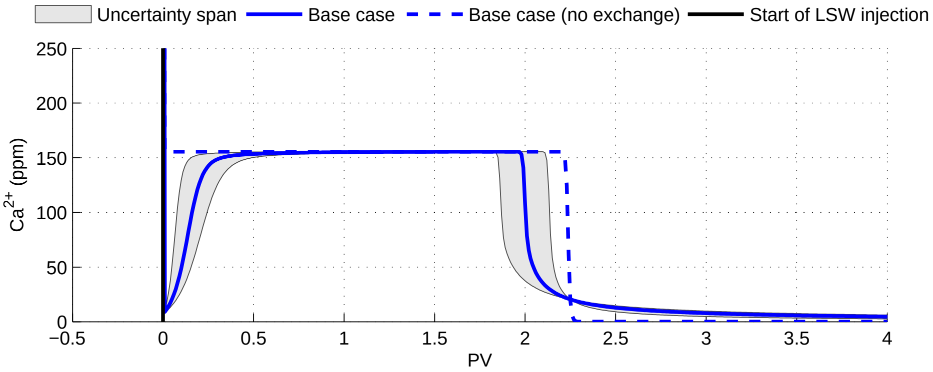

(b) Calcium concentration

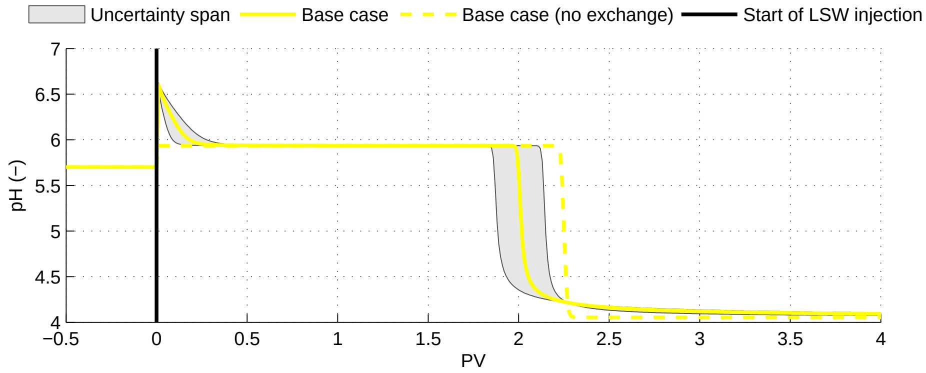

(c) pH

Figure 3.9: Results for ion exchange simulations. Figure 3.9(a) shows the amount of calcite in the first grid cell (i.e., $CaCO_3$ in mmol/kgw) as a function of the injected PVs. In Figure 3.9(b) the corresponding Ca^{2+} concentration is plotted. Figure 3.9(c) shows the evolution of the pH in the first grid cell. For easy comparison, the results of the case without ion exchange have also been plotted in all figures.

When all calcite in the first grid cell has been dissolved, after about 2.0 PV, a new Ca^{2+} equilibrium will establish between the solution and the cation exchanger.

The injected LSW has no Ca^{2+} ions, this disrupts the established exchanger's equilibrium with the solution. To restore the equilibrium, Ca^{2+} will detach from the exchanger and go into the solution. Consequently, Na^+ fills up the empty exchange sites. As discussed in Section 3.3.2, the removal process of Ca^{2+} from the exchanger after all calcite has been dissolved by LSW injection is slow. At 4.0 PV of injected LSW only a fraction of the attached Ca^{2+} has been removed from the exchanger. It seems unlikely that significant removal of Ca^{2+} will occur within a reasonable time.

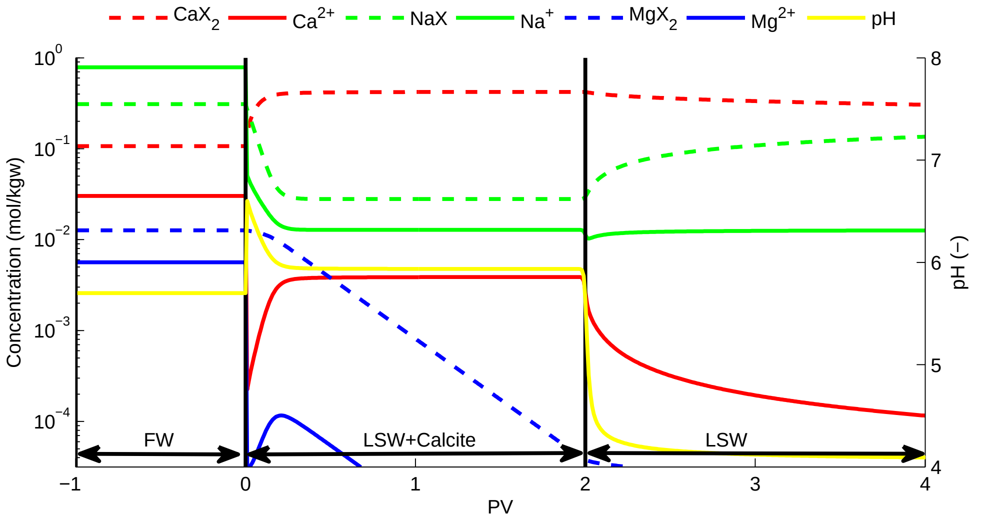

Figure 3.10: Evolution of ion concentrations and exchanger composition in the first grid cell of the model for a simulation including CO_2, calcite dissolution, and cation exchange.

3.4 Mixing

In earlier simulations LSW was modelled such that it pushed FW out of the reservoir without mixing. In reality, mixing between LSW and FW will occur in the reservoir.

In this section, the mixing process between LSW and FW is studied. Firstly, a mixing equilibrium calculation is performed for various mixtures between LSW and FW without calcite. In a second equilibrium calculation also the effect of calcite is taken into account. Finally, a transport simulation is run in which dispersivity is included.

3.4.1 Model Parameters

Values from field experiments from both Chin (2006) and Apello and Postma (2005) indicate that 10% of the displacement length is a reasonable estimate for longitudinal dispersivity in an aquifer. The same results however also indicate that the dispersivity of a particular reservoir can as well be an order of magnitude higher or lower. Mahadevan et al. (2003), working on oil reservoirs, argued that the dispersivity is rather lower than 10% of the displacement length than higher.

To study the effect of dispersivity a base case dispersivity of 5% of the displacement length has been assumed, that is 40 m. The high and low cases have been defined as 80 m and 20 m, respectively.

Other model parameters are those specified in Section 3.3.1. Table 3.3 provides the model parameters.

Table 3.3: Mixing simulations base model parameters

Description	Units	Value
CO_2 pressure	atm	1.38
Initial amount of calcite	mol/kgw	0.943
Flow velocity	m/y	200
Calcite dissolution rate	$mol/(m^2 \cdot s)$	10^{-6}
Specific reaction surface of calcite	m^2/g	0.01
Temperature	°C	85
Exchanger sites	mol/kgw	0.45
Dispersion	m	40

3.4.2 Equilibrium for FW and LSW Mixes without Calcite

During low salinity water flooding LSW and FW are mixed leading to new geochemical equilibria in the formation. In this section it is investigated how different LSW-FW mixtures behave in absence of calcite.

The key ion concentrations are plotted in Figure 3.11(a). By diluting the FW with LSW the ionic strength of the mixture will decrease in a linear fashion, mind that this behavior is masked by the semi-log presentation.

Figure 3.11(b) shows the relative exchange site occupation. For an increasing fraction of LSW, the affinity of Ca^{2+} to be adsorbed on the clay surface increases. The amount of Mg^{2+} attached to the exchanger also slightly increases. This is both an effect of a decrease in ionic strength and a reduction of the Na^+/Ca^{2+} ratio in the mixture. This behavior is described in Section 3.3.2.

Close to a LSW fraction of one the attached Ca^{2+} reaches a maximum. For even higher values of the LSW fraction Ca^{2+} is completely removed from the solution, and thus also from the exchanger.

This behavior also implies that removing Ca^{2+} ions from an exchanger in the formation is very difficult as small concentrations of Ca^{2+} in the solution give rise to a high amount of Ca^{2+} attached to the exchanger. This was also found in Section 3.3.3.

Clearly, when the LSW fraction is one, and only LSW is present, the adsorbed amount of Ca^{2+} to the clay surface is zero[1]. In this situation Na^+ is

---

[1] For actual LSW with Ca^{2+} traces this will not be the case.

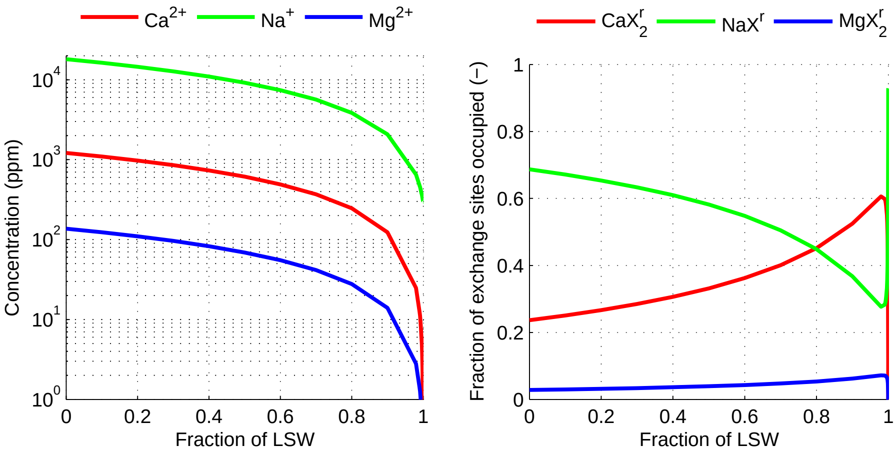

(a) Ion concentrations (b) Exchanger composition

Figure 3.11: Results of mixing FW and LSW without calcite.

the most preferred ion to be adsorbed, with a relative exchange site occupation of around 93%. Hydrogen, H^+, is attached to the remaining 7% of the exchange sites.

For Mg^{2+} the same pattern holds as for Ca^{2+} in the case without calcite. The amount of Mg^{2+} will (slightly) increase upon increasing the fraction of LSW. Close to a LSW fraction of one a maximum value for attached Mg^{2+} is reached. For a LSW fraction of one no Mg^{2+} is in the solution nor on the exchanger.

3.4.3 Equilibrium for FW and LSW Mixes with Calcite

As calcite is available in the formation, the mixing behavior will be influenced accordingly. Upon mixing with LSW, the concentrations for all ions, except for Ca^{2+}, will decrease linear, as already explained in the previous section.

When the saturation index of calcite falls below zero, the equilibrium will be reestablished by dissolving calcite and therefore increasing the Ca^{2+} concentration again. By increasing the fraction of LSW the Ca^{2+} concentration will not be further lowered than the equilibrium concentration due to calcite prescribes. Figure 3.12 shows the results of mixing FW with LSW in the presence of calcite.

From Figure 3.12(a) it is clear that concentrations of Na^+ and Mg^{2+} behave in exactly the same fashion as they did in the case without calcite dissolution (see Section 3.4.2). However, the Ca^{2+} concentration does not go to zero for high LSW fractions due to calcite dissolution.

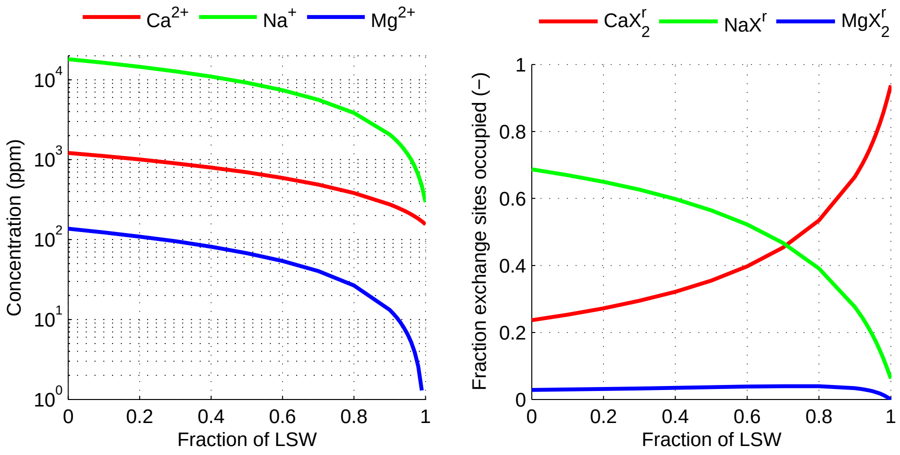

(a) Ion concentrations (b) Exchanger composition

Figure 3.12: Results of mixing FW and LSW in equilibrium with calcite.

Figure 3.12(b) shows the resulting relative exchange site composition as a result of the mixing process. The amount of exchanger attached Ca^{2+} will increase for an increasing LSW fraction. This is in accordance to the behavior described in Section 3.3.2. Increasing concentrations of Ca^{2+} ions on the exchanger upon injecting LSW is not a new idea: it was also described by Apello and Postma (2005) in connection to low saline brine injection into aquifers.

3.4.4 Dispersivity Effects during Fluid Flow

To investigate the impact of dispersivity three simulations have been run. A base case scenario has been defined in which the dispersivity has been assumed to be 5% of the displacement length, that is 40 m. The high and low case have been defined as having a dispersivity of 80 m and 20 m, respectively. All other parameters are equal to the simulation setup of Section 3.3.3.

Figure 3.13(a) shows that the calcite dissolution is slightly slower than in the case without dispersion. This could very well be the case as, due to mixing, it will take longer to get the salinity in the first grid cell down.

However, Figure 3.13(b) shows that the dip in Ca^{2+} concentration has a longer duration. This does not correlate to the shape of the calcite dissolution profile. In the case without dispersion, the minimum in the Ca^{2+} dip corresponds to the highest dissolution rate. For the case with dispersion this is not the case. It seems that by including dispersion into the model a lot of back-diffusion also has been introduced. During water injection, advection is the dominant transport mechanism and therefore the results of this model are inaccurate.

Dispersion will be remodelled in Chapter 4. In Chapter 5 simulations will investigate the impact of dispersion on low salinity water flooding.

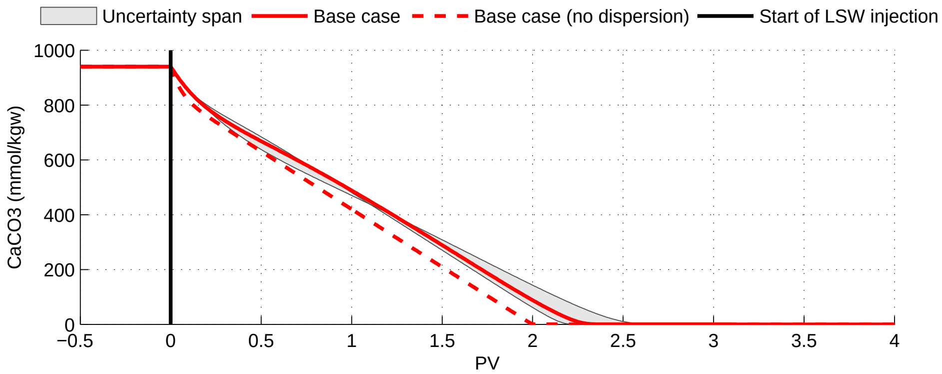

(a) Calcite dissolution

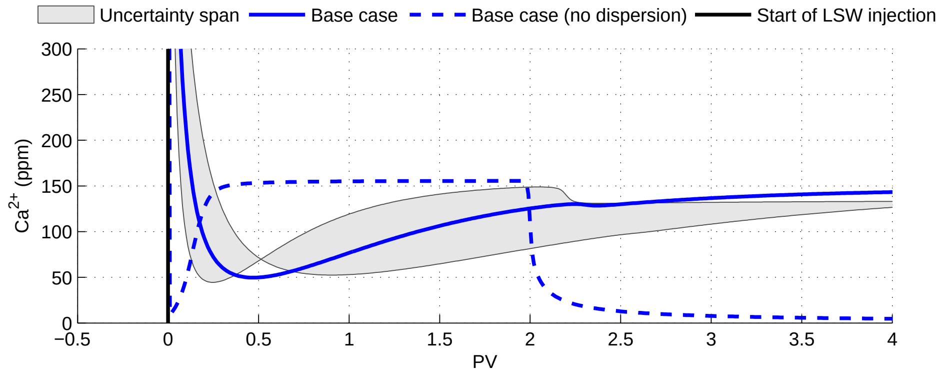

(b) Calcium concentration

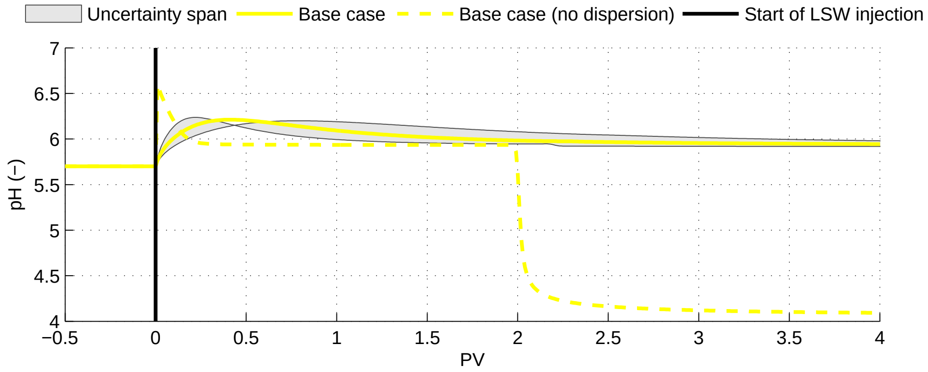

(c) pH

Figure 3.13: Effect of dispersivity on LSW injection.

3.5 SRP Water Injection

A typical source of injection water on the NCS is seawater. In the case study field seawater is treated in a sulphate reducing plant (SRP) to minimize the risk of scaling. The composition of SRP can be found in Appendix C.

Similar to LSW injection, SRP water injection will influence the geochemistry. The differences in ion concentration between FW and SRP water are however smaller than between FW and LSW. The impact on the reservoir chemistry is therefore less.

The standard transport simulation is performed as described in Section 3.1.2. However, SRP is injected instead of LSW. An overview of the simulation parameters can be found in Table 3.4.

Figure 3.14 shows the amount of calcite in the first grid cell as a function of the injected number of PVs. After the initial change from FW to SRP water the ion concentrations and exchanger composition remain constant. This is the case as during the full 4.0 PV of SRP injection calcite is available in the first grid cell. SRP dissolves calcite slower than LSW, as is to be expected. Consequently, after 4.0 PV injection of SRP water, only half of the calcite in the first grid cell is dissolved.

Figure 3.15 shows the simulation results for the ion concentrations and exchanger composition for the first grid cell. The Na^+ and Mg^{2+} concentrations in FW and SRP water are similar. The Ca^{2+} concentration is however much lower in the SRP water. The reduction in Ca^{2+} concentration, in combination with a slightly lower Na^+ and increased Mg^{2+} concentration gives rise to a big increase in attached Mg^{2+}. As the attached Na^+ remains almost constant the Mg^{2+} attaches to the exchanger solely at the expense of Ca^{2+}.

Table 3.4: SRP simulations base model parameters

Description	Units	Value
CO_2 pressure	atm	1.38
Initial amount of calcite	mol/kgw	0.943
Flow velocity	m/y	200
Calcite dissolution rate	$mol/(m^2 \cdot s)$	10^{-6}
Specific reaction surface of calcite	m^2/g	0.01
Temperature	°C	85
Exchanger sites	mol/kgw	0.45

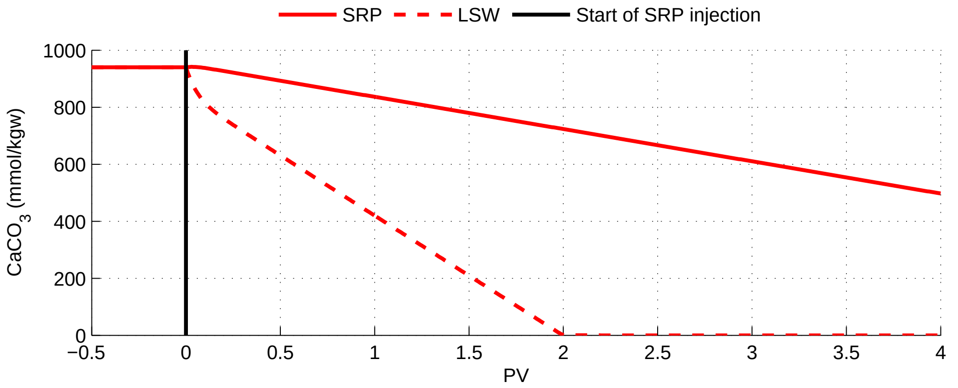

Figure 3.14: Calcite dissolution during SRP injection.

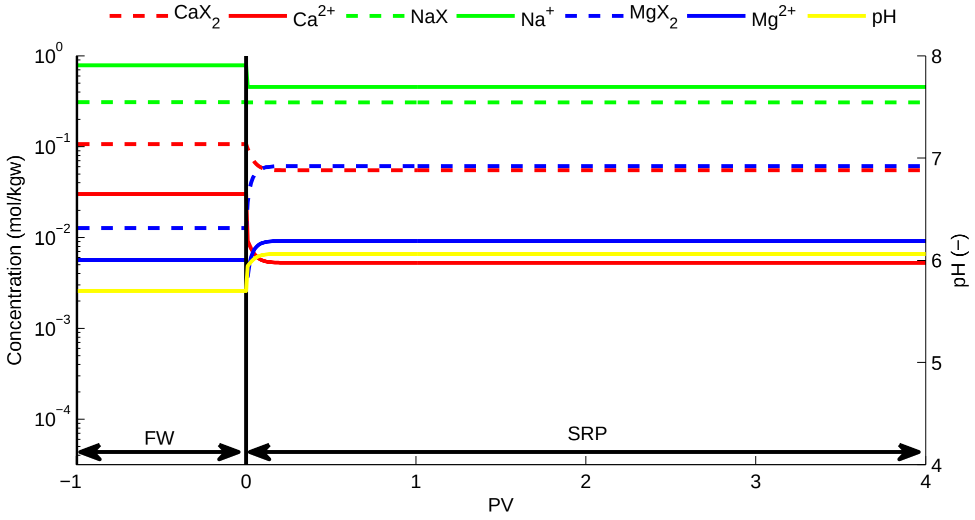

Figure 3.15: Evolution of ion concentrations and exchanger composition in the first grid cell of the model for a simulation including CO_2, calcite dissolution, cation exchange.

3.6 Simulation Stability

To test the simulation stability of the PHREEQC simulator, various transport simulations have been run for an increasing amount of grid cells.

It was found that already for a small number of grid cells, a grid cell every 100 m, stability is reasonable. Of course, in this 8-cell situation the simulator's resolution is poor, but does already a great job capturing the general direction of the solution. It must however be noted that a 10 cell system had convergence issues.

For an increasing number of grid cells, and a decreasing time step, the results become more detailed, i.e., converge. Figure 3.16 shows for 8, 20 and 100 grid cells how number of grid cells influences the simulation results. Note that these results are acquired including the dispersion model. This makes the results indictional for the convergence only.

As always, selecting the amount of grid cells during simulations is a trade-off between the resolution one tries to achieve and the amount of calculation time required. Figure 3.17 shows for 8, 20, 40, 100 and 200 grid cells the lowest salinity reached throughout the reservoir. Clearly, the resolution of the result increases for a larger number of grid cells. That is, convergence occurs.

Increasing the amount of grid cells to 20 already improves the results. The

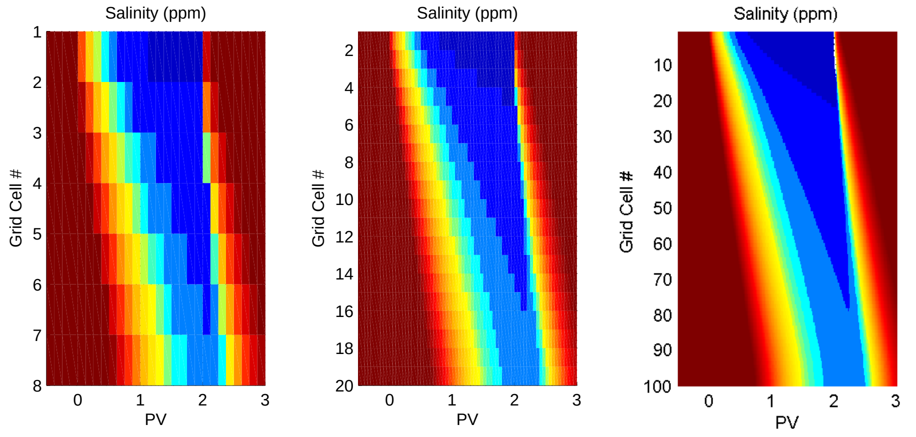

(a) 8 grid cells (b) 20 grid cells (c) 100 grid cells

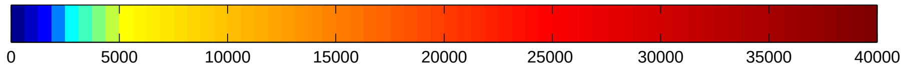

(d) Color bar, Salinity (ppm)

Figure 3.16: LSW slug simulation for a varying number of grid cells.

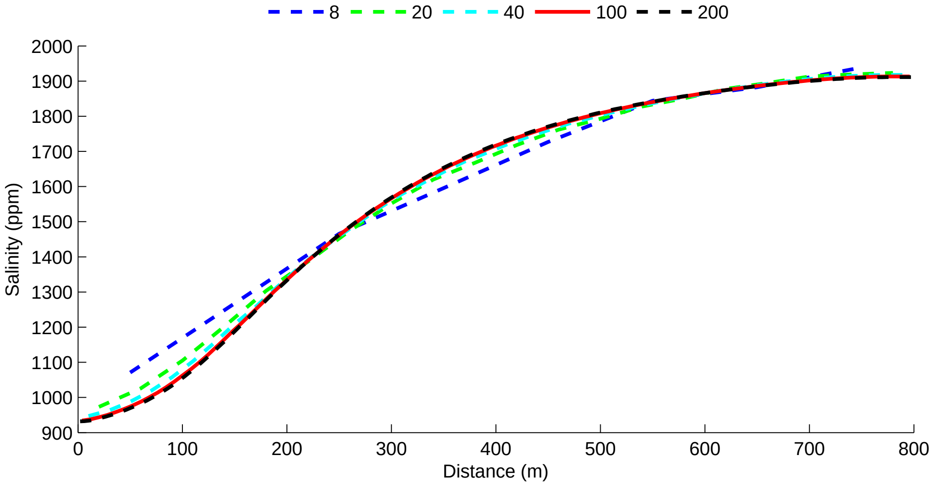

Figure 3.17: Lowest salinity reached for a varying number of grid cells.

40, 100 and 200 grid cell cases are difficult to distinguish, meaning that they have converged significantly. A 40 grid cell system could therefore be chosen as a good trade-off between resolution and calculation time.

However, a model with 100 grid cells is chosen because, in the next chapter, in which a Buckley-Leverett profile will be calculated, also a 100 grid cell system will be used to be able to fully capture the form of the Buckley-Leverett profile. By using the same amount of grid cells comparing both simulation results is straightforward.

The simulation case analyzed in this section includes all model mechanisms and shows excellent stability already at very coarse gridding. Stability issues for a 100 grid cell system are hence not to be expected in any of the simulation cases carried out in this chapter.

Chapter 4

Coupling PHREEQC and BL Flow

The PHREEQC simulations that were carried out in Chapter 3 involved only single-phase water flow. During low salinity water flooding in an oil field, two-phase flow in the reservoir will occur. Both the influence of geochemistry on the oil production and the two-phase flow influence on geochemistry cannot be simulated by means of a PHREEQC simulation alone.

The primary aim of coupling PHREEQC to a two-phase Buckley-Leverett (BL) multiphase flow simulator is therefore twofold:

- Getting an insight in the two-phase flow influence on the geochemistry.
- Understanding the influence of the geochemistry on the two-phase flow, and consequently the oil production.

Another aim of the BL-PHREEQC simulator is to create a simple and extendable tool that can be used in similar future studies on geochemical behavior.

In this chapter all aspects of the coupled simulator will be explained in detail. In Section 4.1 the discretization method used for the Buckley-Leveret advection equation is covered. Section 4.2 describes the methods involved in discretizing the ion transport. The integration and coupling method of geochemistry is discussed in Section 4.3. Then, a brief description of the computational setup is provided in Section 4.4.

4.1 Buckley-Leverett Simulator

In this section, the numerical approach used for the discretization of the Buckley-Leverett formula is covered. The general model and underlying assumptions will be explained followed by the mathematical derivation of the numerical solution. A numerical scheme 2nd order accurate in time and 1st order accurate in space will be created. The stability criteria will be derived and simulations for an increasing amount of grid cells will be performed as to check convergence.

4.1.1 Model Setup

The standard assumptions for the Buckley-Leverett equation apply (see Section 2.4). Relative permeability is, for now, assumed to be a function of the water saturation only. In the next section this assumption will be relaxed to include the dependency on the geochemical state of a grid cell.

The formula of interest is the Buckley-Leverett equation (Dake, 1978)

$$\phi\frac{\partial S_w}{\partial t}+u\frac{\partial f_w}{\partial x}=0 \tag{4.1}$$

in which ϕ is the porosity, u the (constant) Darcy velocity, S_w the water saturation and f_w the fractional flow of water. The fractional flow f_w is defined as

$$f_w=\frac{\lambda_w}{\lambda_w+\lambda_o}+\frac{\lambda_w\lambda_o}{\lambda_w+\lambda_o}\frac{1}{u}\left(\Delta\rho_{wo}g\sin(\vartheta)+\frac{\partial p_c}{\partial x}\right) \tag{4.2}$$

where p_c is the capillary pressure, ρ_{wo} the density difference between water and oil, g the gravitational acceleration, ϑ the angle of inclination of the reservoir, and λ_α is the mobility of phase α. By assuming a horizontal reservoir and negligible capillary pressure ($p_c=0$) Equation 4.2 can be reduced to

$$f_w=\frac{\lambda_w}{\lambda_w+\lambda_o} \tag{4.3}$$

which is a function of the water and oil mobilities only. Mobility is defined as the permeability of a porous material to a given phase α divided by the viscosity of that phase. That is:

$$\lambda_\alpha=\frac{kk_{r,\alpha}}{\mu_\alpha} \tag{4.4}$$

where k is the absolute permeability of the rock, $k_{r,\alpha}$ is the relative permeability of the rock with respect to phase α and μ_α is the viscosity of phase α.

4.1.2 Numerical Discretization

Discretization of the Buckley-Leverett equation in a one-dimensional space of length L is performed by means of a finite difference method. A mesh of $N+1$ grid points x_i for $i = 0, 1, ..., N$ is defined. All grid cells have width $\Delta x = L/N$ and are of the cell-centered type. Figure 4.1 shows a schematic representation of the discrete grid.

By integrating the Buckley-Leverett equation, Equation 4.1, over a single grid cell, we get

$$\phi \int_{x_{i-\frac{1}{2}}}^{x_{i+\frac{1}{2}}} \frac{\partial S_w}{\partial t} dx = -u \int_{x_{i-\frac{1}{2}}}^{x_{i+\frac{1}{2}}} \frac{\partial f_w}{\partial x} dx \tag{4.5}$$

By assuming an average water saturation $S_{w,i}$ for each grid cell the previous equation can be further rewritten to

$$\phi \frac{d}{dt} \Big(\Delta x S_{w,i} \Big) = -u \Big(f_{w,i+\frac{1}{2}} - f_{w,i-\frac{1}{2}} \Big) \tag{4.6}$$

As a first approximation the left-hand side (LHS) of Equation 4.6 is temporal discretized using the 1st order accurate Euler forward method

$$\phi \Delta x \left(\frac{S_{w,i}^{n+1} - S_{w,i}^{n}}{\Delta t} \right) = -u \Big(f_{w,i+\frac{1}{2}}^{n} - f_{w,i-\frac{1}{2}}^{n} \Big) \tag{4.7}$$

which can be further rewritten in a fully explicit form for the water saturation

$$S_{w,i}^{n+1} = S_{w,i}^{n} - \frac{u \Delta t}{\phi \Delta x} \Big(f_{w,i+\frac{1}{2}}^{n} - f_{w,i-\frac{1}{2}}^{n} \Big) \tag{4.8}$$

For the spatial discretization the first order upwind is chosen and therefore $f_{w,i+\frac{1}{2}} = f_{w,i}$ and $f_{i-\frac{1}{2}} = f_{w,i-1}$. Equation 4.8 can now be rewritten as

$$S_{w,i}^{n+1} = S_{w,i}^{n} - \frac{u \Delta t}{\phi \Delta x} \Big(f_{w,i}^{n} - f_{w,i-1}^{n} \Big) \tag{4.9}$$

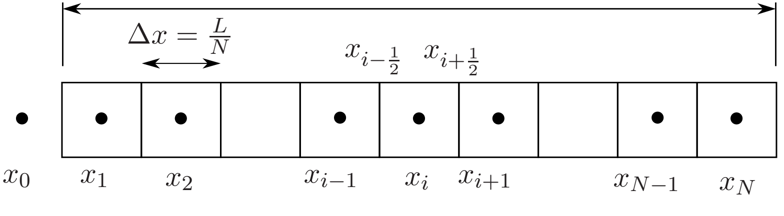

Figure 4.1: Discretized domain using $N + 1$ grid cells.

Equation 4.9 can also be written in a matrix form

$$\mathbf{S_w^{n+1}} = \mathbf{S_w^n} - \frac{u\Delta t}{\phi \Delta x}\Big(\mathbf{K_u f_w^n} - \mathbf{f_{bc}^n}\Big) \tag{4.10}$$

where $\mathbf{S_w^n}$ is a $N \times 1$ vector built up of the water saturation of all grid cells at time step n. $\mathbf{K_u}$ is a $N \times N$ matrix defined as,

$$\mathbf{K_u} = \begin{pmatrix} 1 & & & \\ -1 & 1 & & \\ & \ddots & \ddots & \\ & & -1 & 1 \end{pmatrix} \tag{4.11}$$

and $\mathbf{f_w^n}$ and $\mathbf{f_{bc}^n}$ are $N \times 1$ vectors defined as

$$\mathbf{f_w^n} = \begin{pmatrix} f_{w,1}^n \\ \vdots \\ \vdots \\ f_{w,N}^n \end{pmatrix}, \qquad \mathbf{f_{bc}^n} = \begin{pmatrix} f_{w,0}^n \\ 0 \\ \vdots \\ 0 \end{pmatrix} = \begin{pmatrix} 1 \\ 0 \\ \vdots \\ 0 \end{pmatrix} \tag{4.12}$$

As can be seen from the matrix formulation and the definition of the boundary condition vector $\mathbf{f_{bc}^n}$, an extra point $f_{w,0}$ is introduced which is located a distance Δx in front of point x_1. At this position the boundary condition $S_w(0,t) = 1$ is extrapolated, and therefore $f_{w,0} = 1$. By doing so, a small numerical error is introduced. As long as Δx is very small compared to the total length of the column, the error is negligible.

Initial simulations showed that the first order of discretization in time was not adequate. Small (diminishing) oscillations occurred upon switching the relative permeability curves during low salinity water injection at the newly established shock front. To solve this, a second order time discretization was introduced by means of the Modified Euler method.

The Modified Euler method captures both information at the beginning of a time step (equal to Euler Forward method) and in addition the information at the end of a time step. The final result of a single time step is based on the average of both sets of information. This can be regarded as a predictor-corrector way of numerical analysis. Equation 4.10 can be modified to the Euler Modified method as follows (Koenig, 1998)

$$\mathbf{S_w^{n+1}} = \mathbf{S_w^n} - \frac{u\Delta t}{\phi \Delta x}\frac{\Big(\mathbf{K_u f_w^n} - \mathbf{f_{bc}^n}\Big) + \Big(\mathbf{K_u \tilde{f}_w^{n+1}} - \mathbf{f_{bc}^{n+1}}\Big)}{2} \tag{4.13}$$

where $\tilde{\mathbf{f}}_{\mathbf{w}}^{\mathbf{n+1}}\left(\tilde{\mathbf{S}}_{\mathbf{w}}^{\mathbf{n+1}}\right)$ can be determined by first calculating the predictor step

$$\tilde{\mathbf{S}}_{\mathbf{w}}^{\mathbf{n+1}} = \mathbf{S}_{\mathbf{w}}^{\mathbf{n}} - \frac{u\Delta t}{\phi\Delta x}\left(\mathbf{K}_{\mathbf{u}}\mathbf{f}_{\mathbf{w}}^{\mathbf{n}} - \mathbf{f}_{\mathbf{bc}}^{\mathbf{n}}\right) \tag{4.14}$$

and calculating the fractional flow $\tilde{\mathbf{f}}_{\mathbf{w}}^{\mathbf{n+1}}$ from $\tilde{\mathbf{S}}_{\mathbf{w}}^{\mathbf{n+1}}$.

The modified Euler method is in fact a special implementation of the inclusive second order Runge-Kutta method for solving ordinary differential equations (Pozrikidis, 2009). The resulting numerical system is now first order accurate in space and second order accurate in time.

4.1.3 Convergence Criterion

Convergence of a numerical solution towards the 'real' answer is a necessary condition for accurate predictions. For convergence, both the consistency and stability of a numerical scheme must be within certain limits.

In the Buckley-Leverett theory water saturations travel with their respective *characteristic velocity*, given by (Dake, 1978)

$$\frac{x}{t} = \frac{u}{\phi}\left(\frac{df_w}{dS_w}\right)_{S_w=\text{const}} \equiv v_{S_w}(S_w) \tag{4.15}$$

To ensure stability for the Buckley-Leverett profile, stability must hold for all saturations travelling through the reservoir.

Stability of the numerical scheme used can be checked by making use of the Courant-Friedrichs-Lewy CFL condition (Chen, 2008), given by

$$\Delta t_{BL} < \frac{\Delta x}{v} \tag{4.16}$$

where Δt_{BL} is the time step used in the Euler forward method, Δx the grid cell size and v_{S_w} the characteristic velocity as defined in Equation 4.15.

Full stability is only achieved when the saturation with the highest saturation velocity is stable. To fulfill this requirement, the CFL condition must hold for the saturation for which the derivative of the fractional flow with respect to the water saturation is maximum, that is

$$\Delta t_{BL} < \frac{\phi\Delta x}{u \cdot \max\left\{\frac{df_w}{dS_w}\right\}} \tag{4.17}$$

Instead of performing a formal derivation of the consistency, simulations for various amounts of grid cells and (stable) step sizes have been carried out. The results are compared against the simple analytical Buckley-Leverett solution to check for both the accuracy and convergence of the numerical solution.

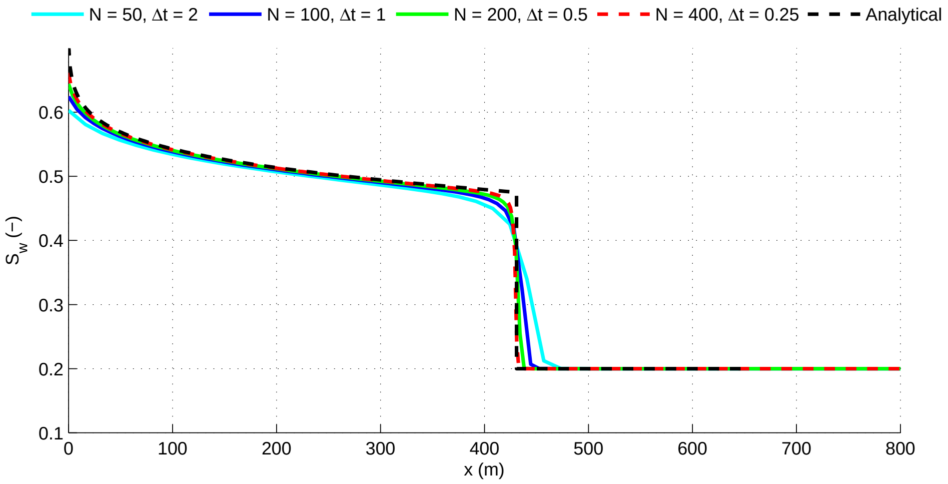

Figure 4.2: Buckley-Leverett simulator convergence demonstration. Comparison between numerical solution for different amounts of grid cells (N) for stable time steps (Δt_{BL} in days). Results plotted for $t = 250$ days.

Figure 4.2 shows that the accuracy of the numerical scheme is adequate and convergence towards the analytical solutions occurs for an increasing number of grid cells and decreasing time step length. Based on this analysis, the number of grid cells to be used was set to $N = 100$ in combination with the associated stable step size. This will result in a solution that captures the shock front reasonably well within reasonable CPU time.

4.2 Ion Transport

In this section the discretization method of the ion transport will be described. The approach is similar to that used in Section 4.1 for the Buckley-Leverett discretization. However, a higher order spatial scheme will be used. As will become clear in Section 4.2.2, this will create the need for flux limiters in the numerical scheme, which will be discussed in Section 4.2.3. Finally, the convergence criteria will be discussed. The resulting scheme will be second order accurate both in time as well as in space.

4.2.1 Model Setup

In addition to the assumptions of Section 4.1, this model assumes that all ions are in the aqueous phase and will therefore follow the water's Buckley-Leverett type of transport. Ions are modelled as passive water tracers. This means that during transport no interactions between ions in the liquid phase or at the interface between rock, oil and water will occur.

4.2.2 Numerical Discretization

Similarly as for the Buckley-Leverett equation, the discretization of the ion transport in a one-dimensional space of length L is performed with a cell-centered finite difference method. However, due to the use of a higher order spatial scheme a mesh of $N+2$ grid points x_i for $i = -1, 0, 1, ..., N$ is needed. That is, yet an additional grid point x_{-1} needs to be defined. The grid cell width is again $\Delta x = L/N$. Figure 4.3 shows a schematic representation of the new extended discrete grid.

The ion concentration in each grid cell will be modelled with the same type of advection equation as the water saturation. However, the equation now takes the form (Omekeh et al., 2012)

$$\phi \frac{\partial}{\partial t} \left(S_w C_\gamma \right) + u \frac{\partial}{\partial x} \left(f_w C_\gamma \right) = 0 \tag{4.18}$$

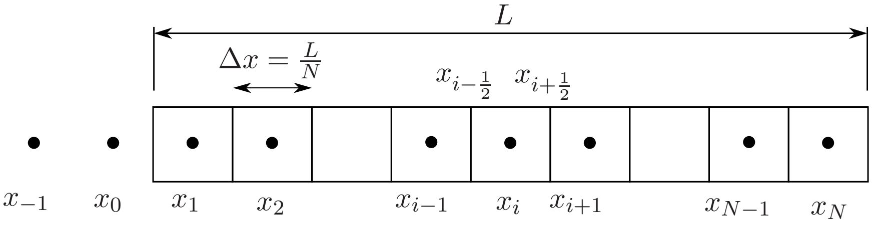

Figure 4.3: Discretized domain using $N + 2$ grid cells.

where C_γ is the concentration of ion type γ. Using the water particle velocity (Isaacson, 1980), defined as

$$h = \frac{f_w}{S_w} \tag{4.19}$$

Equation 4.18 can be loosely written as (Sumnu-Dindoruk and Dindoruk, 2008)

$$\phi \frac{\partial C_\gamma}{\partial t} + uh \frac{\partial C_\gamma}{\partial x} = \frac{\partial C_\gamma}{\partial t} + \frac{u}{\phi} \frac{f_w}{S_w} \frac{\partial C_\gamma}{\partial x} = 0 \tag{4.20}$$

It is important to note that the water saturation S_w should not become zero, which would lead to infinite values and a model breakdown. As the water saturation cannot be lower than the connate water saturation $S_w \geq S_{wc}$, a water saturation of zero is impossible.

Equation 4.20 can in theory be discretized in a similar way as was done for the Buckley-Leverett advection equation. A problem arising with first order spatial discretization is that it often exhibits large numerical dispersion. Especially for multi-component augmented reservoir simulation this has been discussed in multiple papers (Alsofi and Blunt, 2010, Jerauld et al., 2006a,b). It is recognized that the standard method of limiting numerical dispersion, increasing the amount of grid cells, is often impractical as it in augmented reservoir simulations leads to unrealistic large amounts of grid cells.

An example of the dispersion in a first order upwind system is shown in Figure 4.4. The initial block function is highly dispersed after one transport cycle, fully due to numerical dispersion. Higher order numerical schemes can be used to limit numerical dispersion while keeping the required amount of grid cells realistic (Lantz, 1971).

In this thesis, the ion transport equation is discretized both second order in time by means of the Modified Euler method, as well as second order in space by means of a second order Upwind scheme. By applying the first order accurate Euler forward method[1] and the second order Upwind method to Equation 4.20, the resulting equation will be

$$\frac{C_{\gamma,i}^{n+1} - C_{\gamma,i}^{n}}{\Delta t} + \frac{u}{\phi} \frac{f_{w,i}^{n}}{S_{w,i}^{n}} \frac{3C_{\gamma,i}^{n} - 4C_{\gamma,i-1}^{n} + C_{\gamma,i-2}^{n}}{2\Delta x} = 0 \tag{4.21}$$

which can be rewritten to

$$C_{\gamma,i}^{n+1} = C_{\gamma,i}^{n} - \frac{u\Delta t}{2\phi\Delta x} \frac{f_{w,i}^{n}}{S_{w,i}^{n}} \left[3C_{\gamma,i}^{n} - 4C_{\gamma,i-1}^{n} + C_{\gamma,i-2}^{n}\right] \tag{4.22}$$

However, higher order numerical schemes suffer from oscillations near discrete steps. That is, if one tries to simulate a slug of low ion concentration

---

[1] The Modified Euler method will be applied as a modification to first order scheme.

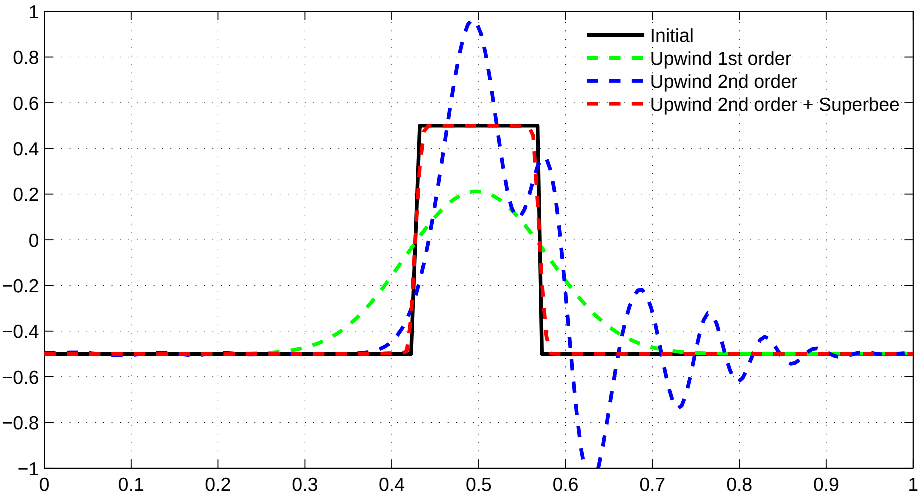

Figure 4.4: Example of numerical behavior for a block function as input for a 1st order, 2nd order, and flux limited upwind scheme. The 1st order upwind scheme shows massive numerical dispersion, the 2nd order is less dispersed but suffers from oscillations and consequently produces non-physical results. The second order upwind flux limited scheme provides a good match after one transport cycle.

with the numerical scheme from Equation 4.22 the result will be heavily distorted. Figure 4.4 shows an example for the use of a second order upwind scheme with a block function as initial input. After one transport cycle the 2nd order upwind solution shows lots of oscillations that will lead to faulty conclusions and non-physical results.

4.2.3 Removal of Oscillations using a Flux Limiter

Removing oscillations from higher order schemes can be accomplished by using so-called flux limiters (Hirsch, 2007). To do so, the first step is to rewrite the 2nd order upwind scheme as a correction to the monotone first order upwind difference, and writing the correction terms in the form of successive gradients

$$\begin{aligned} C^{n+1}_{\gamma,i} = C^{n}_{\gamma,i} \quad &- \overbrace{\frac{u\Delta t}{\phi\Delta x}\frac{f^{n}_{w,i}}{S^{n}_{w,i}}\left[C^{n}_{\gamma,i} - C^{n}_{\gamma,i-1}\right]}^{\text{1st order upwind}} \qquad (4.23) \\ &- \underbrace{\frac{u\Delta t}{\phi\Delta x}\frac{f^{n}_{w,i}}{S^{n}_{w,i}}\left[+\frac{1}{2}\left(C^{n}_{\gamma,i} - C^{n}_{\gamma,i-1}\right) - \frac{1}{2}\left(C^{n}_{\gamma,i-1} - C^{n}_{\gamma,i-2}\right)\right]}_{\text{Correction terms}} \end{aligned}$$

As a next step, both non-monotonous terms are multiplied by the flux limiter functions $\Psi(r_i)$ and $\Psi(r_{i-1})$, where

$$r_{i-1} = \frac{u_i - u_{i-1}}{u_{i-1} - u_{i-2}}, \quad r_i = \frac{u_{i+1} - u_i}{u_i - u_{i-1}} \tag{4.24}$$

which leads to

$$\begin{aligned} C_{\gamma,i}^{n+1} = C_{\gamma,i}^{n} & - \frac{u\Delta t}{\phi \Delta x} \frac{f_{w,i}^{n}}{S_{w,i}^{n}} \left[C_{\gamma,i}^{n} - C_{\gamma,i-1}^{n} \right] - \frac{u\Delta t}{\phi \Delta x} \frac{f_{w,i}^{n}}{S_{w,i}^{n}} \\ & \times \left[+\frac{1}{2}\Psi(r_i)\left(C_{\gamma,i}^{n} - C_{\gamma,i-1}^{n}\right) - \frac{1}{2}\Psi(r_{i-1})\left(C_{\gamma,i-1}^{n} - C_{\gamma,i-2}^{n}\right) \right] \end{aligned} \tag{4.25}$$

This can be rewritten to

$$C_{\gamma,i}^{n+1} = C_{\gamma,i}^{n} - \frac{u\Delta t}{\phi \Delta x} \frac{f_{w,i}^{n}}{S_{w,i}^{n}} \left[1 + \frac{1}{2}\Psi(r_i) - \frac{1}{2}\frac{\Psi(r_{i-1})}{r_{i-1}} \right] \left(C_{\gamma,i}^{n} - C_{\gamma,i-1}^{n} \right) \tag{4.26}$$

resulting in the flux limited second order upwind, first order Euler forward numerical scheme.

A large variety of flux limiter functions $\Psi(r_i)$ have been developed over the last decades. The flux limiter functions all need to fulfill certain requirements to be both stable and efficient in removing oscillations. A full review on all mathematical requirements and their implications is however outside the scope of this thesis. A good practical explanation can be found in Hirsch (2007).

There is no flux limiter function which is suitable in all situations. The limiter function in the ion transport numerical scheme must preserve a discrete step (slug) quite well compared to upwind 1st order. However, as the numerical dispersion will be used to model the physical dispersion, some degree of dispersion must remain. Three limiter functions have been tested for these properties:

$$\begin{aligned} \text{Superbee:} \quad & \Psi(r_i) && = \max\left[0, \min(2r_i, 1), \min(r_i, 2)\right] \\ \text{minmod:} \quad & \Psi(r_i) && = \max\left[0, \min(1, r_i)\right] \\ \text{Sweby:} \quad & \Psi(r_i) && = \max\left[0, \min(\beta r_i, 1), \min(r_i, \beta)\right]; \quad (1 \leq \beta \leq 2) \end{aligned}$$

A general example for the three different limiters can be found in Figure 4.5. The Superbee limiter has very limited diffusion and can capture discontinuities very well, also after many time steps. The minmod limiter is generally regarded as still very diffusive. As the numerical dispersion should model the analytical dispersion this behavior is a desired property. During testing on the simulator it was however found that the minmod flux limiter still had too much dispersion to model physical dispersion adequately. A third flux limiting function, the Sweby limiter, has a tuning parameter β that may range between 1 and 2. For

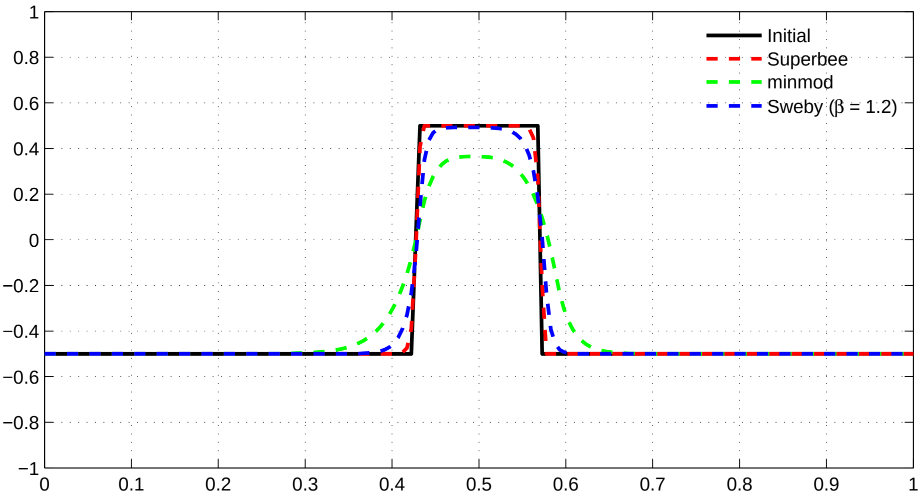

Figure 4.5: Example of numerical behavior for a block function as input using the Superbee, minmod and Sweby limiters, in a 2nd order upwind scheme. The elapsed time is equal to 10 transport cycles.

$\beta = 1$ the Sweby limiter is equal to the minmod limiter, for $\beta = 2$ the Sweby limiter is equal to the Superbee limiter. That is, by changing the parameter β between 1 and 2 the Sweby flux limiter can be freely tuned such that the numerical dispersion can be matched to the physical dispersion that one aims to model.

Equation 4.26 can now fully be evaluated numerically, it is however still only first order accurate in time. As second order accuracy is desired, the same modified Euler method as earlier described for the Buckley-Leverett equation will be applied. First the predictor step must be calculated,

$$\begin{aligned}\tilde{C}^{n+1}_{\gamma,i} = C^{n}_{\gamma,i} & - \frac{u\Delta t}{\phi \Delta x}\frac{f^{n}_{w,i}}{S^{n}_{w,i}}\left[1 + \frac{1}{2}\Psi(r_i) - \frac{1}{2}\frac{\Psi(r_{i-1})}{r_{i-1}}\right] \\ & \times \left(C^{n}_{\gamma,i} - C^{n}_{\gamma,i-1}\right)\end{aligned} \tag{4.27}$$

and secondly the averaged information of both the beginning and the ending of the time step is used in the corrector step to produce the final numerical prediction of the result of a single time step

$$\begin{aligned}C^{n+1}_{\gamma,i} = C^{n}_{\gamma,i} & - \frac{u\Delta t}{\phi \Delta x}\frac{f^{n}_{w,i}}{S^{n}_{w,i}}\left[1 + \frac{1}{2}\Psi(r_i) - \frac{1}{2}\frac{\Psi(r_{i-1})}{r_{i-1}}\right] \\ & \times \frac{\left(C^{n}_{\gamma,i} - C^{n}_{\gamma,i-1}\right) + \left(\tilde{C}^{n+1}_{\gamma,i} - \tilde{C}^{n+1}_{\gamma,i-1}\right)}{2}\end{aligned} \tag{4.28}$$

The resulting numerical scheme from the combination of Equations 4.27 and 4.28 is now both 2nd order accurate in time as well as in space. The scheme, as presented here, is used in the Buckley-Leverett + PHREEQC simulator for each ion type that is included in the simulation.

4.2.4 Convergence Criteria

For the standard advection formula of the form

$$\frac{\partial u}{\partial t} + a\frac{\partial u}{\partial x} = 0 \tag{4.29}$$

the CFL condition is defined as

$$\Delta t \leq \frac{\Delta x}{a} \tag{4.30}$$

The parameter a is not equal in the Buckley-Leverett formula and in the ion transport equation. The relation between the expressions of a_{IT} for ion transport and a_{BL} for Buckley-Leverett flow is the factor $\frac{f_w}{S_w}$ (see Section 4.2.2), which results in

$$a_{IT} = \frac{f_w}{S_w} a_{BL} \tag{4.31}$$

The CFL condition for ion transport can thus be written as a function of the CFL condition of the Buckley-Leverett equation by

$$\Delta t_{IT} \leq \frac{\Delta x}{a_{IT}} = \frac{\Delta x}{\dfrac{f_w}{S_w} a_{BL}} = \Delta t_{BL} \frac{S_w}{f_w} \tag{4.32}$$

The minimum value of the RHS of Equation 4.32 will be reached if the water saturation S_w is minimum and the fractional flow f_w is at a maximum,

$$\Delta t_{IT} \leq \Delta t_{BL} \frac{\min(S_w)}{\max(f_w)} = \Delta t_{BL} \frac{S_{wc}}{1} \tag{4.33}$$

where S_{wc} is value larger than 0 and smaller than $1 - S_{or}$.

As it is physically impossible that the water saturation is at connate conditions and at the same time the fractional flow of water is at a maximum the actual constraint to the maximum time step Δt_{IT} will be somewhat more relaxed. The minimum value for the ratio between the water saturation and fractional flow is a function of the relative permeability model used. To ensure stability in the ion transport one should therefore compute the time step based on the relative permeability model.

As will be explained later[2], for the relative permeability model used in this thesis a stable time step $\Delta t_{IT} = \frac{1}{2}\Delta t_{BL}$ is used. The overall stable time step

---

[2] Chapter 5 will cover a detailed description of all model parameters and a calculation of the stable step size using the utilized relative permeability model.

Δt for the combined simulator should therefore be

$$\Delta t = \min\left(\Delta t_{BL}, \Delta t_{IT}\right) = \min\left(\Delta t_{BL}, \frac{1}{2}\Delta t_{BL}\right) = \frac{1}{2}\Delta t_{BL} \tag{4.34}$$

A check for convergence of the ion transport model is carried out for an increasing amount of grid cells, whilst keeping the time step at stable values. The results for a LSW slug injected at $t = 0$ days for 50 days are plotted at both time $t = 500$ days and $t = 1000$ days in Figure 4.6. It must be noted that this simulation is carried out for a reservoir initially saturated with only formation water (and thus no oil). As expected, for an increasing number of grid cells the solution converges to the analytical solution. The analytical solution is in this case a constant boundary LSW slug travelling through the reservoir as no diffusion or dispersion is explicitly modelled.

As it is the intention to model the ion transport in such a way that the numerical dispersion equals the physical dispersion an appropriate amount of

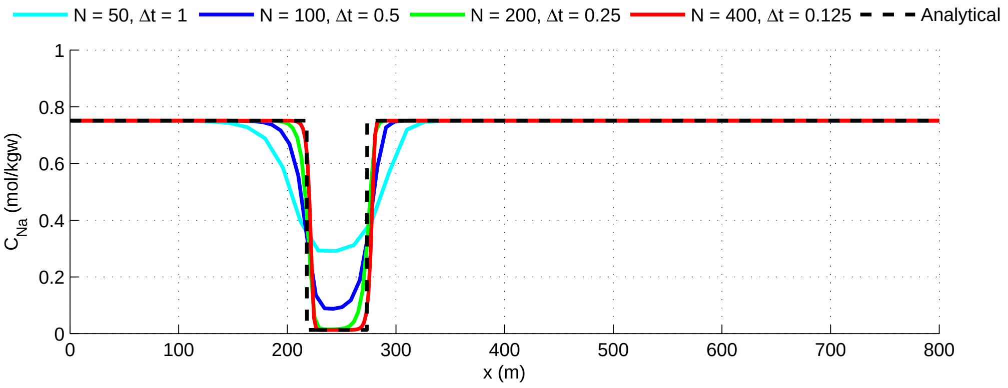

(a) $t = 500$ days

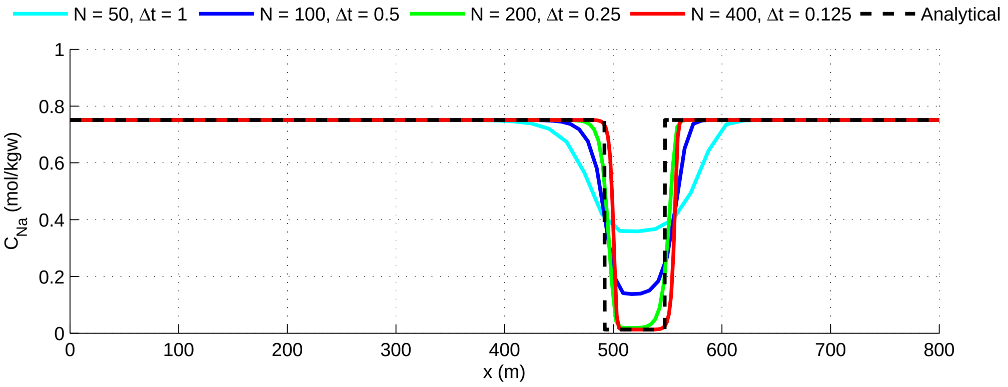

(b) $t = 1000$ days

Figure 4.6: Ion transport simulation numerical convergence.

grid cells should be chosen.

The simulations carried out in this section are in a water-only system and can therefore only be used to show the numerical system's convergence. When the ion transport is simulated in combination with low water saturation and Buckley-Leverett type two-phase displacement, extra dispersion is introduced due to varying flow velocities. An estimate of the total amount of grid cells that is needed in a particular setup thus depends on the initial water saturation, relative permeability model and the actual amount of physical dispersion that one needs to model.

4.3 Adding Geochemistry

In this section the incorporation of geochemical interactions in the Buckley-Leverett simulator will be covered. The geochemical model assumptions and implications of these assumptions are explained.

4.3.1 Geochemical Simulation Details

In PHREEQC, by default, a fully water saturated grid cell containing one kilogram of water is used. All parameters are defined relative to one kilogram of water. During a Buckley-Leverett simulation water slowly replaces oil in the reservoir, so that the water saturation in grid cells increases over time.

This effect is taken into account in the PHREEQC simulations by using the water saturation of a grid cell, as a multiplier for the amount of water used in a PHREEQC simulation. That is, when the water saturation $S_w = 0.5$, the PHREEQC simulation will be carried out for 0.5 kg of water.

However, the amount of exchanger sites are still defined in the PHREEQC simulation setup per kilogram water (Parkhurst and Apello, 1999). If one reduces the amount of water, then effectively a part of the exchanger sites in a grid cell cannot be reached anymore. This leads to the need to track which parts of the exchanger have and have not been in contact with water, making the simulation rather complicated (in addition, there is no spatial distribution in a single grid cell). A problem along the same lines holds for calcite dissolution.

To simplify this problem, it has been assumed that water can always contact all calcite and clay in a grid cell. That is, water wetness with respect to calcite and clay is assumed. Regardless of the water saturation in a grid cell, the total number of cation exchange sites is therefore constant. Meaning that, for a water saturation of $S_w = 0.5$ there are twice as much cation exchange sites defined per kilogram water as for a simulation with $S_w = 1.0$. This will increase the effects of cation exchange.

The geochemistry of a grid cell will be simulated in high precision each time the PHREEQC simulator is called. As grid cells do not have spatial dimensions, all ions, exchanger sites and calcite will be ‘evenly spread’ in a single grid cell.

4.3.2 Coupling by means of Relative Permeability

It is assumed that the low salinity effect can be modelled by a change in relative permeability, leading to a lower residual oil saturation and a more favourable displacement of the oil phase. Consequently, increasing the recovery from an oil field.

The standard way of switching between high salinity and low salinity relative permeability curves is to define a salinity threshold. This approach was also adopted in this thesis.

The salinity of a grid cell is calculated every time step by

$$\text{Salinity (ppm)} = 1000 \cdot \sum_{\gamma} C_{\gamma} M(\gamma) \tag{4.35}$$

where $\gamma \in \{\text{Na}^{+},\text{Ca}^{2+},\text{Mg}^{2+},...\}$, C_{γ} the concentration in mol/L and $M(\gamma)$ the molar mass in g/mol of ion type γ.

Upon injecting LSW into the formation the ion concentration will decrease, and consequently the salinity will decrease. A single ‘correct’ low salinity threshold does not exist and many different views on this value exist. In this thesis, threshold values ranging from 1000 ppm to 3000 ppm are used.

The threshold model used in the simulator can be fully described by:

$$\text{Relperm model} = \begin{cases} \text{Low salinity} & \text{if salinity} < \text{salinity threshold} \\ \text{High salinity} & \text{otherwise} \end{cases}$$

Alternative definitions for the low salinity threshold, which for example take into account the $\text{Na}^{+}/\text{Ca}^{2+}$ ratio, could potentially enhance the model. This has however not been performed in this thesis.

4.4 Simulator Setup

In this section an overview of the software that was used to build the coupled Buckley-Leverett and PHREEQC simulator is given. In addition the general computational flow of the simulator is explained.

4.4.1 Software

The coupled simulator was written in MATLAB® R2012a. Buckley-Leverett and ion advection calculations were performed in MATLAB® code.

Geochemistry has been added to the simulator by means of the IPHREEQC component object model (COM) modules. A requirement for this to work on an x64 operating system is that both the 32- and 64-bit modules must be installed on the PC (Charlton and Parkhurst, 2011). Version 2.18.3 build 5570 of the IPHREEQC module has been used to simulate the geochemistry. All simulations are performed using the standard *phreeqc.dat* geochemical database supplied with the PHREEQC package.

4.4.2 Computational Setup

Figure 4.7 shows the flow diagram of the coupled simulator. Before a simulation can be run all required input data (i.e., initial state, reservoir properties, injection scheme, etc) must be specified. Upon starting the simulator the simulation will first be prepared. This step involves generating matrices for the injection scheme and matrices that will be used to store the simulation results.

Next, a loop will start that will iterate through all grid cells for all time steps. The first step in the loop is to determine the permeability model that will be used in the transport calculation. In this thesis, the relative permeability is a function of water saturation and salinity, hence it is a function of the geochemical composition of a the grid cell. Based on the relative permeability model the Buckley-Leverett water and ion transport will be calculated.

The next step involves one of the three modes of operation. The mode that is to be used is defined in the input. The three possible modes are:

Ion transport only In this mode, PHREEQC will not be part of the simulation. This means that no cation exchange or calcite is included in the simulation. The advantage of this simulation is that it is very fast (typical simulation time ∼5 minutes for the typical simulation setup used in this thesis).

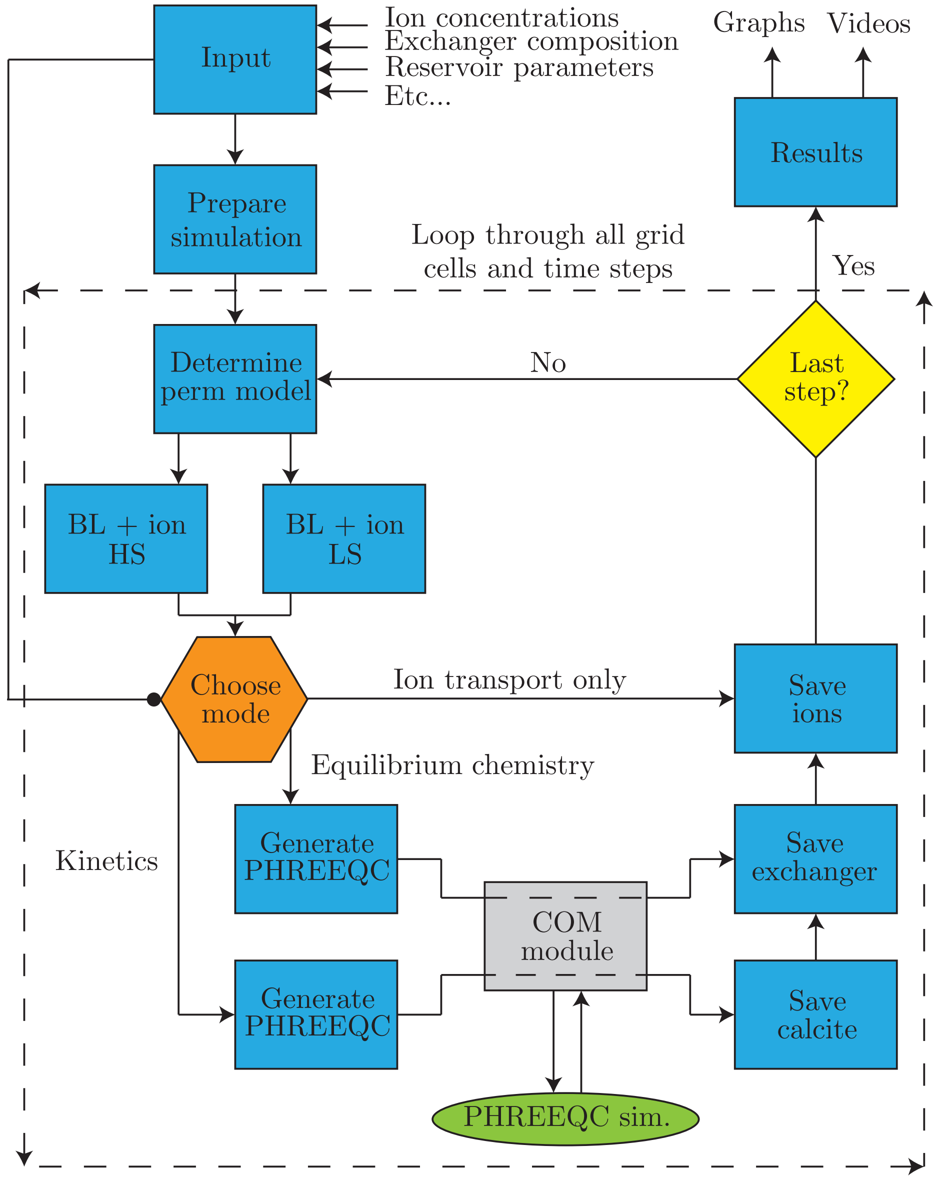

Figure 4.7: Flow diagram of coupled simulator.

Equilibrium chemistry The second mode of operation includes equilibrium chemistry. This will include cation exchange and calcite. An infinite amount of calcite will however be available and consequently one will never dissolve all calcite. The advantage of this method is that it includes most features and is still reasonably fast (typical simulation time ∼45 minutes).

Kinetics This mode is the most extensive mode of operation and includes all modelled features from this thesis. In each grid cell the amount of calcite is tracked, which means that it can also fully dissolve. The advantage of this mode is that it incorporates the most detailed model. However, a disadvantage are long simulation times (typical simulation time ∼5-6 hours). A reference to a simulation with geochemistry in thesis always means that the kinetic mode of operation is used.

If the first mode of operation is used, no communication with PHREEQC is performed and the results of the ion transport simulation will be saved directly after the Buckley-Leverett transport. For the other two modes, PHREEQC data files will be generated based on the Buckley-Leverett transport results, and send to the PHREEQC simulator via a COM module. The results of the geochemical simulation performed will be saved. The level of detail in the information that will be saved depends on the mode of operation. When all data for the specific mode of operation are saved, the process is repeated for the next grid cell / time step.

On completing all steps, the loop is ended and the results of the simulation can be outputted. In the program, a simple command line interface is build that provides methods to plot graphs and generate video files.

Figure 4.8 shows a detailed view of the simulation processes occurring

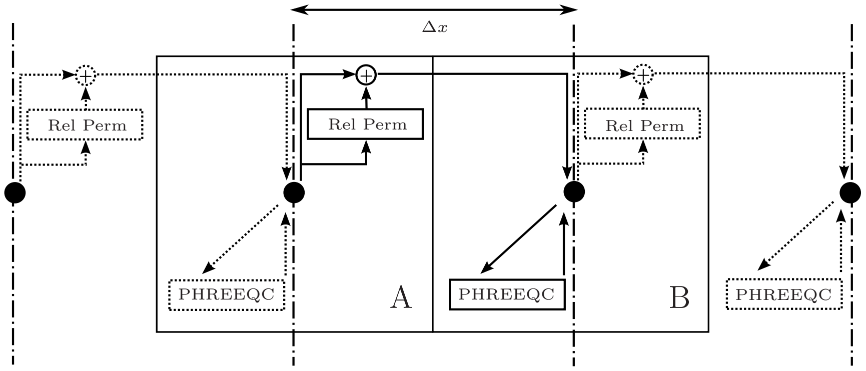

Figure 4.8: Schematic of computational setup. The four dots represent four grid cell center points, two grid cell are fully drawn. The calculation flow between these grid cells is drawn with solid lines.

between two grid cells A and B. Assuming that the geochemical state and water saturation for grid cell A are known, the relative permeability model can be determined. In combination with the ion concentrations and water saturation the transport to grid cell B can be calculated. The Buckley-Leverett transport calculation results in a new water saturation and ion concentrations for grid cell B.

These results are used as input for the PHREEQC geochemical simulator. Output from this geochemical simulation will be saved as the final ion concentrations for grid cell B, as if it were the transport result. In addition, the result for the exchanger and calcite dissolution are saved in grid cell B.

The full geochemical state and water saturation for B are now calculated. The described calculation cycle will be repeated for each grid cell and every time step.

Chapter 5

PHREEQC and BL Simulations

This chapter will cover the simulation results obtained by the second order space-time combined Buckley-Leverett and PHREEQC simulator as described in the previous chapter. In the first section, a detailed description of the general simulation setup will be given. The remainder of the chapter will concern simulation results that try to answer specific questions regarding the effects of geochemical interactions on the salinity, oil production and low salinity 'fingerprints' at the producer.

5.1 Basic Simulation Setup

For all simulations carried out in this chapter the basic simulation setup is equal. This setup will be covered in full detail in this section. Any deviations from this setup will be clearly stated at the beginning of a simulation section.

5.1.1 Basic Parameters

Under consideration is a typical well pair, with an injector-producer distance of 800 m, from the case study field's low salinity project target area. The reservoir is modelled using a 1D flow path between the injector and producer, assuming a homogeneous reservoir based on available mineralogic data (see Appendix B). Only the cation exchange capacity and calcite have been taken into account, all other rock components are assumed to be non-reactive. The resulting reservoir properties can be found in Table 5.1.

Oil is being produced by means of water injection and thus two-phase flow in the reservoir will occur. The two-phase flow is modelled by a Buckley-

Table 5.1: Reservoir data

Description	Variable	Units	Value
Porosity	ϕ	-	0.22
Initial calcite	-	mol/grid cell	0.94
Calcite dissolution rate	-	mol/($m^2\cdot$ s)	10^{-6}
Calcite specific surface	-	m^2/g	0.01
Exchanger sites	-	mol/grid cell	0.45
CO_2 pressure	P_{CO_2}	atm	1.51

Table 5.2: Fluid and relative permeability data

Description	Variable	Units	HS value	LS value
Darcy velocity	u	m/day	0.12	n/c
Viscosity of water	μ_w	mPa·s	1.0	n/c
Viscosity of oil	μ_o	mPa·s	2.4	n/c
Temperature	T	°C	85	n/c
Initial water saturation	$S_{w,init}$	-	0.2	n/c
Connate water saturation	$S_{w,c}$	-	0.2	n/c
Residual oil saturation	$S_{o,r}$	-	0.2	0.15
Corey water coefficient	n_w	-	2	2
Corey oil coefficient	n_o	-	6	5
Rel. perm. endpoint water	k_{rwe}	-	0.45	0.25
Rel. perm. endpoint oil	k_{roe}	-	1.0	n/c

Table 5.3: General simulation data

Description	Variable	Units	Value (low/base/high)
Number of grid cells	N	-	100
Distance between wells	L	m	800
Time step	Δt	days	1.0
Spatial step size	Δx	m	8
Salinity threshold	-	ppm	1,000/3,000/5,000
Limiter tuning parameter	β	-	1.4/1.6/1.8

Leverett equation. Three different water types will be used in the simulations, namely, formation water (FW), sulphate reduced seawater (SRP water) and low salinity water (LSW). Ion compositions of these fluids can be found in Appendix C. Further data on the oil and water properties can be found in Table 5.2.

The numerical system will be equal to the system described in Chapter 4. The general simulation data can be found in Table 5.3.

5.1.2 Relative Permeability Model

The relative permeability model used in all simulations is based on idealized field data. That is, it is the shape and behavior that is reproduced via Corey model type-curves. The relative permeability model consists of two sets of curves: the water and oil relative permeability for the high salinity and low salinity case. In Figure 5.1(a) the resulting relative permeability curves are plotted.

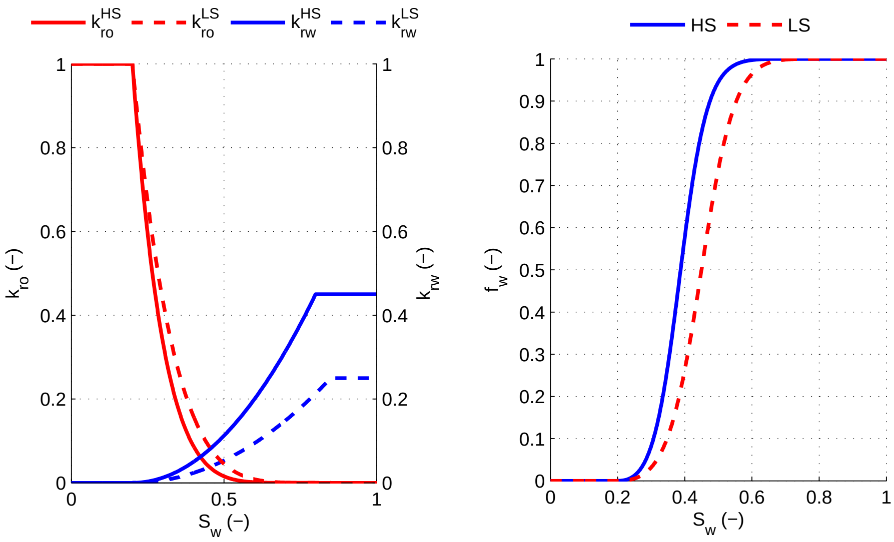

(a) Relative permeability (b) Fractional flow

Figure 5.1: Relative permeability model used in simulations.

As can be seen, the relative permeability to oil for the low salinity case shows an overall higher value compared to the high salinity case. For water, the relative permeability becomes less. In this way, the increase in oil production by injection of low salinity water can be modelled.

Figure 5.1(b) shows the water fractional flow curves for the same relative permeability model. From this figure, the expected shock front saturation for both high and low salinity water can be determined graphically, which clearly indicates that $S_{w,sh}^{HS} < S_{w,sh}^{LS}$. Because of the higher shock front saturation during low salinity flooding, a second shock front is expected to flow through the reservoir.

5.1.3 Numerical Stability

In order to ensure a converging solution for the Buckley-Leverett profile (Equation 4.17), it is required that the time step Δt_{BL} satisfies

$$\Delta t_{BL} < \frac{\phi \Delta x}{u \max \left\{ \frac{df_w}{dS_w} \right\}} = \frac{0.22 \cdot 8 \text{ m}}{0.12 \text{ m/day} \cdot 6.3} = 2.3 \text{ days} \tag{5.1}$$

The values for the Darcy velocity u and the spatial step Δx are taken from Table 5.3. The porosity value is taken from Table 5.1. The maximum value for the derivative of the fractional flow with respect to the water saturation can be determined from Figure 5.2(a). The highest value for the derivative is for the high saline situation. As the simulation should be stable in both high and low salinity cases the highest peak value should be chosen, that is $\max\{df_w/dS_w\} \approx 6.3$.

However, the ion transport stability requires a slightly smaller time step

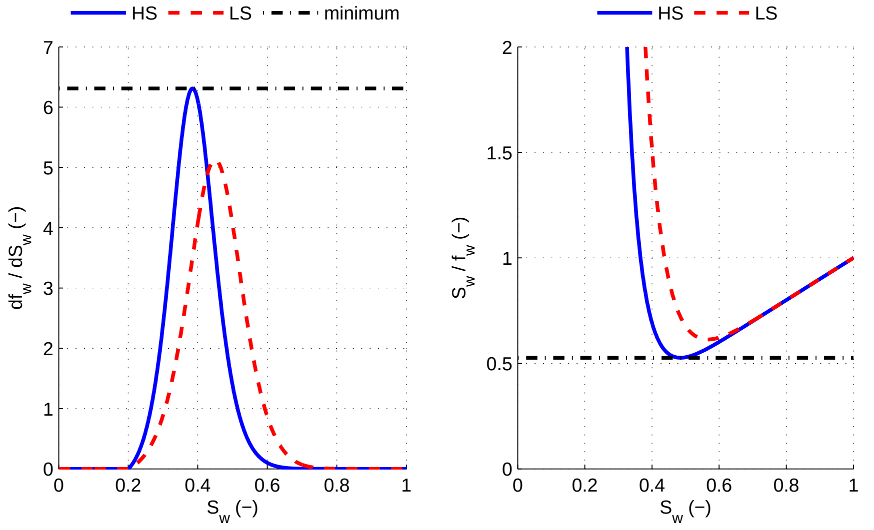

(a) Fractional flow derivative (b) Water saturation over fractional flow

Figure 5.2: Determination of stability for the relative permeability model.

via Equation 4.33,

$$\Delta t_{IT} < \frac{\min(S_w)}{\max(f_w)} \Delta t_{BL} \approx 0.5 \cdot 2.3 \text{ days} = 1.2 \text{ days} \tag{5.2}$$

where $\frac{\min(S_w)}{\max(f_w)}$ can be determined from Figure 5.2(b). Equation 4.34 shows that the overall stable time step limit is equal to the smallest limit calculated for either the water transport or the ion transport. As the ion transport stable time step is clearly shorter than the Buckley-Leverett stable time step, the overall time step must be shorter than 1.2 days. A slightly lower value of $\Delta t = 1.0$ day is arbitrarily chosen from the stable domain.

5.1.4 Numerical Dispersion

Values from field experiments from both Chin (2006) and Apello and Postma (2005) indicate that 10% of the displacement length is a reasonable estimate for longitudinal dispersivity in an aquifer. The same results also indicate that the dispersivity of a particular reservoir can as well be an order of magnitude higher or lower. Research by Mahadevan et al. (2003), which is more focussed towards oil reservoirs, shows that the dispersivity is more likely to be lower than 10% of the displacement length rather than higher.

For the following simulations a dispersion of circa 7% of the travel length is assumed. The numerical dispersion can be tuned to match the desired physical dispersion by changing the amount of grid cells or altering the tuning parameter β.

For a number of grid cells of $N = 100$ it has been found that it can be simulated without problems in about 5-6 hours for a full simulation (including PHREEQC kinetics) of 20 years (7300 time steps). Doubling to $N = 200$ grid cells (which requires also the double amount of time steps) increases the simulation time to unpractical values.

Although a single PHREEQC kinetic calculation takes only about 30 ms, for a simulation with 200 grid cells and 14,600 time steps this equates to almost 24 hours, which is impractical for quick calculations. A 100 grid cell setup is therefore highly desired.

All simulations are performed on a standard Intel® Core™ i5 processor clocked at 2.6 Ghz with 8 GB of RAM memory.

To tune the dispersion to the desired 7% value 6 simulations, without PHREEQC geochemical interaction, for both $N = 100$ and $N = 200$ have been run. All further parameters of these simulations are equal to the default setup, except for the tuning parameter β.

For a single-phase simulation, one would expect a 1 m wide low ion concentration slug to be dispersed over a length of around $1 \cdot 7\% \cdot 800 = 56$ m. The

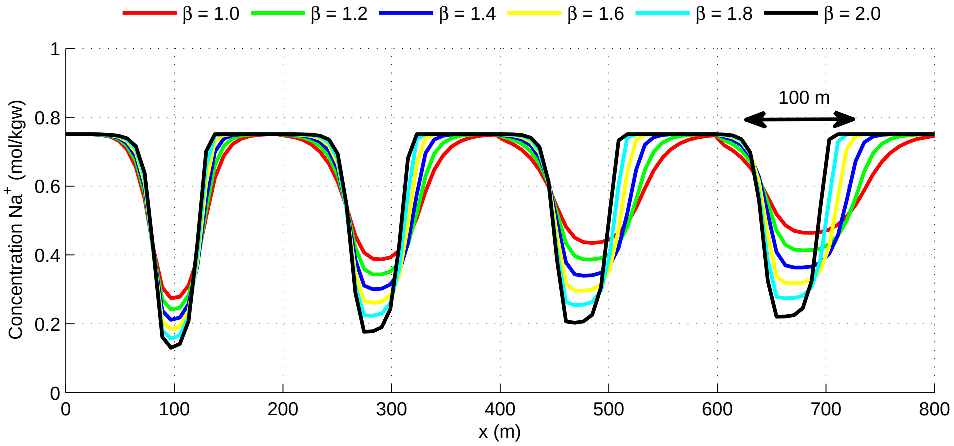

(a) $N = 100$ grid cells

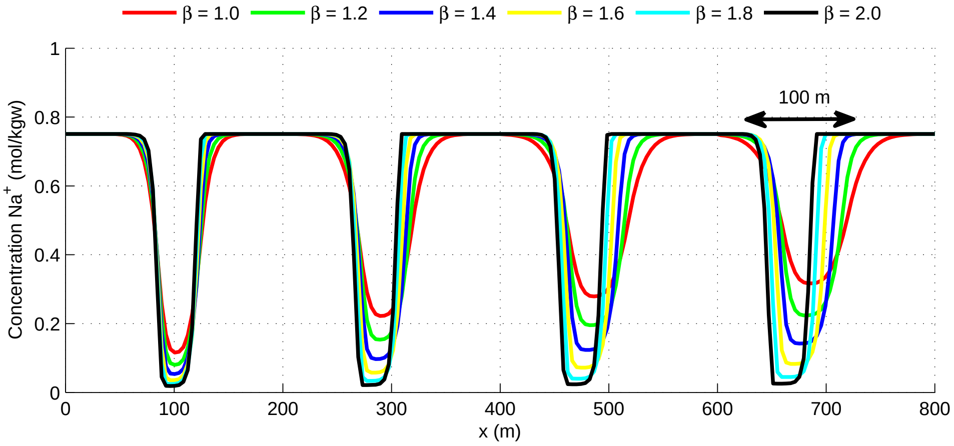

(b) $N = 200$ grid cells

Figure 5.3: A single low salinity slug plotted for the cases $N = 100$ and $N = 200$ in two graphs. Each graph shows the slug for time steps 1600, 1800, 2000 and 2200 days for various values for the tuning parameters β.

tuning test is performed for 40 days of injection, resulting in a low concentration slug width of 22 m. Using the same reasoning as before, the slug will be dispersed in both directions around 30 m. That means that the total width of the slug should be close to 80 m. This is however only valid for single-phase flow.

As the multiphase flow also affects the amount of dispersion observed in the ion concentration, the tuning simulations have been performed for situation in which already 1.0 PV of FW has been injected, such that there is a non-constant water saturation throughout the reservoir. That is, the LSW injection start is at $t = 1461$ days.

One would expect the dispersion in the water phase to be higher due to higher velocities in the water. To compensate for this, the original estimated value of 80 m width is rounded to 100 m. This of course is a rough assumption and a more detailed study into the actual dispersion is of major importance for the low salinity flooding process. This however, requires more field data on dispersion.

The simulation results for various -allowable- values of β for the Sweby limiter are plotted in Figure 5.3. For the $N = 200$ case it is clear that the dispersion is less than for simulations carried out for $N = 100$ and equal values for β. However, in both situations a dispersed slug size of around 100 m can be found. Table 5.4 sums up the tuning parameters that are used.

It may be noted that a higher number of grid cells, and a lower tuning parameter is more desirable as it gives smoother results. However, for practical reasons (simulation time and memory issues), a lower number of grid cells ($N = 100$) and higher tuning parameter has been chosen.

Table 5.4: Dispersion tuning parameters

Grid cells	Low dispersion	Base dispersion	High dispersion
$N = 100$	$\beta = 1.8$	$\beta = 1.6$	$\beta = 1.4$
$N = 200$	$\beta = 1.4$	$\beta = 1.2$	$\beta = 1.0$

5.2 Verification with PHREEQC

In this section the newly constructed simulator's results are checked against the previously run PHREEQC simulations for a water-only situation.

5.2.1 Setup Modifications

To be able to have a direct comparison between the PHREEQC water-only simulations and the two-phase flow simulation, the latter has been reduced to single-phase flow by using the following altered input parameters:

Table 5.5: Variable modifications for verification case

Description	Variable	Units	Value
Initial water saturation	$S_{w,init}$	-	0.98
Residual oil saturation	$S_{o,r}$	-	0.01

This means that the reservoir is almost fully flooded with water initially, and oil flow can thus be neglected. In addition, no switch from high salinity to low salinity relative permeability curves is performed; the high salinity model using the modifications of Table 5.5 is always used. The water injection scheme is equal to the scheme used in Section 3.3.3 which means first 1.0 PV of FW is injection, followed by 4.0 PV of LSW.

Because the relative permeability model is different in this case, also the stability criterion has changed. The derivative of the fractional flow is lower, and the minimum value of S_w/f_w is slightly higher. This means that the stable time step of the default setup is still within the stable region of the modified setup. Therefore, the default time step is used unchanged.

5.2.2 Results

The results of this simulation are plotted against the PHREEQC results of the simulations performed in Section 3.3.3 and Section 3.4.4. The simulations from these sections include all geochemical effects that are also implemented in the combined Buckley-Leverett and PHREEQC simulator. These effects are CO_2-buffering, calcite dissolution and cation exchange.

a) Calcite and pH

Results for the amount of calcite in the first grid cell for the three different simulations are plotted in Figure 5.4(a). From this figure it is clear that the calcite dissolution profile of the combined simulator resembles the behavior simulated with PHREEQC. Compared to the PHREEQC results the combined simulator predicts a dissolution profile which is between the non-dispersion (solid red line) and base dispersion affected (dashed red line) case. As the dispersion is indeed between zero and the PHREEQC base case value, the results of the combined simulator show expected behavior.

At first sight, the pH results of Figure 5.4(b) seem not to agree with earlier simulations. However, the PHREEQC results also show significant differences in the pH for the results with or without dispersion. The combined simulator's results lie neatly between the two results. It is therefore concluded that also the pH has a reasonable match.

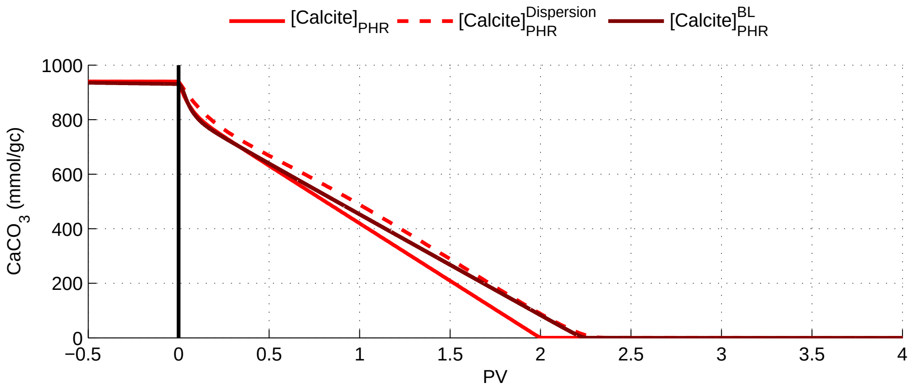

(a) Calcite dissolution

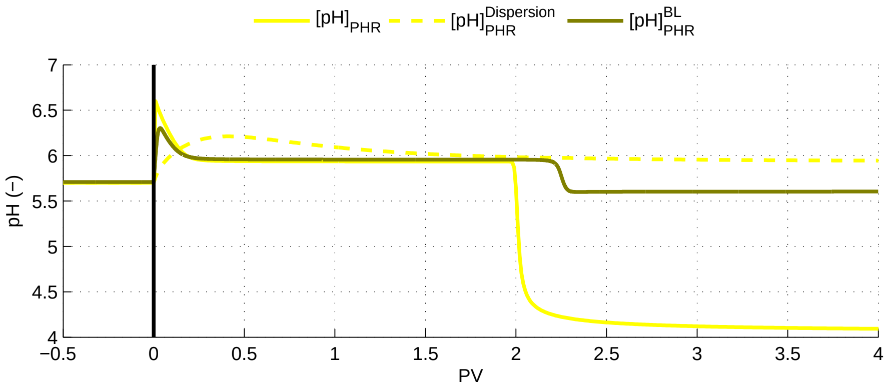

(b) pH

Figure 5.4: Comparison between simulator results for calcite and pH.

b) Ion Concentration and Exchanger Composition

The ion concentration profiles from Figure 5.5(a) are only plotted for the combined simulator and the non-dispersion affected PHREEQC simulation. Small differences at the initial shock are visible, which are again caused by dispersion in the combined simulator. As the timing for the moment when calcite is fully dissolved is slightly different, a delay in ion concentration drop at around 2.0 PV is visible. Other than a small time-shift the behavior of the two simulations are in good agreement.

The cation exchange mechanism shows equal behavior in both simulation setups, see Figure 5.5(b). Again, a match between both simulators is found.

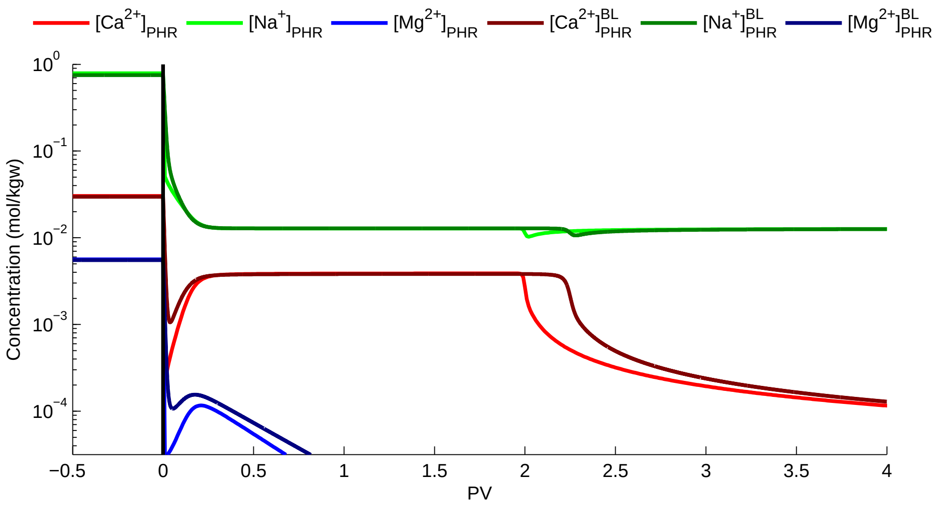

(a) Ion concentration

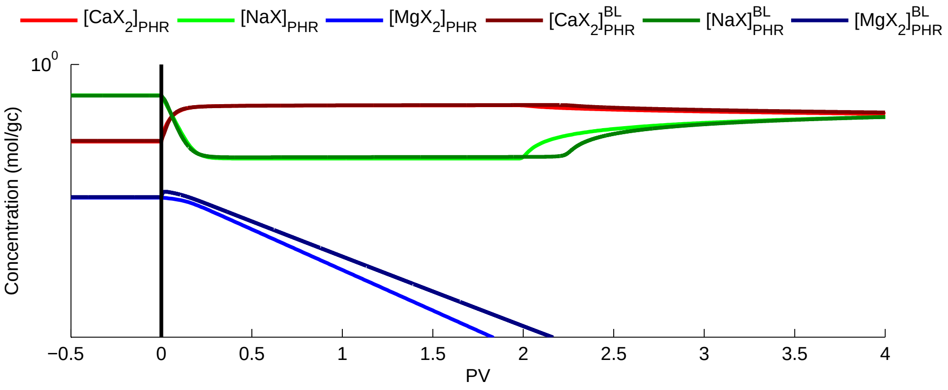

(b) Exchanger composition

Figure 5.5: Comparison between simulator results for the ion concentration and the exchanger composition.

5.3 Including Buckley-Leverett Behavior

The previous section showed a good match between the newly created combined simulator and the original PHREEQC simulations. In this section, two-phase oil-water flow is introduced into the setup. A secondary mode water flooding simulation is carried out to verify the simulator's behavior.

A more in-depth investigation of tertiary mode water flooding is performed as most low salinity projects are carried out in already water flooded fields. The injection schemes for secondary and tertiary mode water flooding are defined as follows:

- Secondary: 5.0 PV of LSW from $t = 1$ days.
- Tertiary: 1.0 PV of FW from $t = 1$ days, followed by 4.0 PV of FW.

5.3.1 Secondary Mode

To verify the simulator's behavior, a simulation for secondary mode low salinity water flooding has been carried out. Starting from $t = 1$ day, 5.0 PV of LSW will be injected into the reservoir. All other simulation input parameters are equal to the base case simulation setup as defined at the beginning of this chapter.

Figure 5.6 shows the water saturation profile throughout the reservoir after one year of injection. A good qualitative match with the theoretically predicted profile, as described in Section 2.4.2, is obtained. The constant-saturation bank behind the first shock front is made up of connate water. The dashed line represents the position of the salinity threshold concentration. This indeed coincides with the location as predicted in the theory. However, it must be

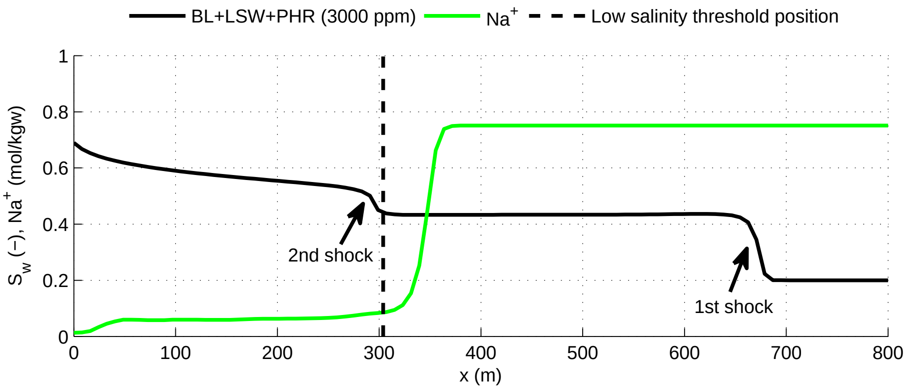

Figure 5.6: Buckley-Leverett profile and Na^+ concentration for secondary mode LSW flooding at $t = 365$ days (0.25 PV).

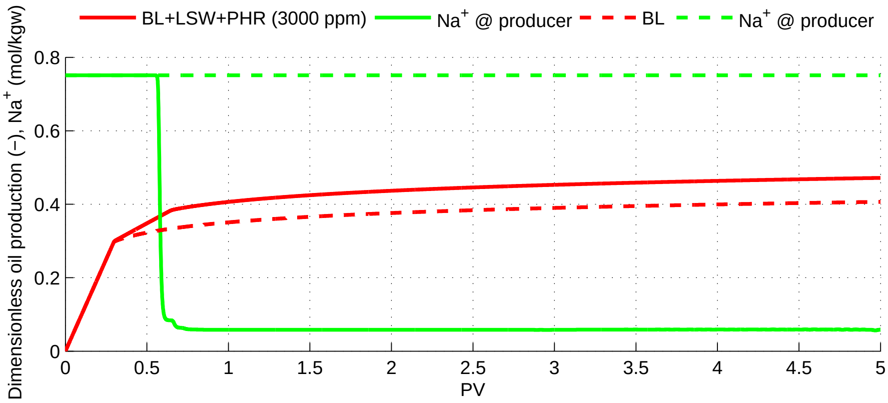

Figure 5.7: Cumulative oil production as a function of injected PVs LSW for secondary flooding.

noted that due to dispersion the salinity has already dropped significantly before this point. To show this, the Na^+ concentration has also been plotted in the figure.

The cumulative oil production in secondary flooding mode has been plotted in Figure 5.7 for both a high (dashed lines) and low salinity flooding scenario (solid lines). The increase in oil production for the low salinity scenario happens relatively early in the production life, when the second constant water-cut region is produced. The Na^+ concentration profile clearly shows that the breakthrough of low salinity water coincides with the end of the second constant water cut region.

The Buckley-Leverett profile and cumulative oil production simulated with the coupled simulator exhibit behavior expected from the theory, which it of course should, as it is based on this theory. A more in-depth discussion of the combined simulator results will be covered in the next section for a tertiary flooding mode.

5.3.2 Tertiary Mode

In tertiary mode, LSW is injected after a reservoir has already been flooded with FW. Most low salinity water flooding projects are aimed at improving the recovery from a conventional water flooded reservoir. Being the most common flooding scheme, an in-depth analysis of the combined simulator results will be performed.

Simulations have been carried out for a reservoir that has been flushed with 1.0 PV of FW and has produced around 35% of the OOIP during the period of conventional water flooding. Water breakthrough has already happened.

A switch to LSW injection is made at $t = 1460$ days, and will continue to be the injection fluid until the end of the simulation. That is, a total of 4.0 PV of LSW will be injected into the reservoir. Based on the theory from Section 2.4.2 an oil bank should establish in front of the LSW. Figure 5.8 shows the Buckley-Leverett water saturation profile throughout the reservoir at time step $t = 2100$ days. From this figure it is clear that indeed an oil bank has formed, which means that the numerical simulator captures the theoretical behavior.

The position of the low salinity threshold value again coincides with location predicted by the theory. However, just as was observed in the secondary mode flooding, the salinity has already dropped significantly before the actual threshold is reached.

To investigate the influence of geochemical processes on the oil production during low salinity water injection, simulations have been carried out for varying low salinity thresholds. The simulations are all based on the default setup described at the beginning of this chapter, with slight modifications that are

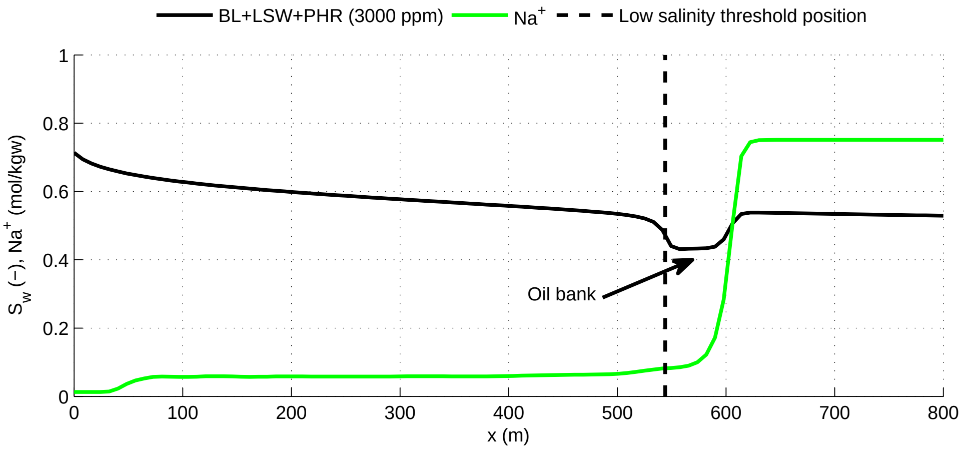

Figure 5.8: Buckley-Leverett profile for tertiary flooding at $t = 2100$ days.

Table 5.6: Overview of tertiary mode simulations

Simulation	#1	#2	#3	#4	#5	#6
Geochemical interactions	no	no	yes	yes	yes	yes
Threshold (ppm)	n/a	1000	1000	1500	2000	3000

summed up in Table 5.6.

The resulting cumulative oil production profiles are plotted in Figure 5.9. The increase in oil production observed for a non-geochemical affected secondary low salinity injection scheme is 5.8% for a low salinity threshold of 1000 ppm, compared to a simulation without low salinity effect. For simulations with geochemical interactions the incremental oil is 0.5%, 3.2%, 5.7% or 5.8% for a salinity threshold of 1000 ppm, 1500 ppm, 2000 ppm, or 3000 ppm, respectively. This indicates that salinity is influenced by geochemical interactions and consequently the cumulative oil production is affected.

Figure 5.10(a) shows the salinity profiles of simulations 1-6 at time step $t =$ 2200 days. In the simulations without geochemical interactions, simulations 1 and 2, the salinity in the reservoir changes in a single step to the LSW salinity of 750 ppm. This is not completely true for simulation 2, as a small bump in salinity occurs due to the switching of relative permeability model (marked with a dashed gray ellipse). This effect is however neglected.

For the simulations that include geochemical interactions, simulation 3-6, not a single, but three salinity steps can be observed. To further investigate

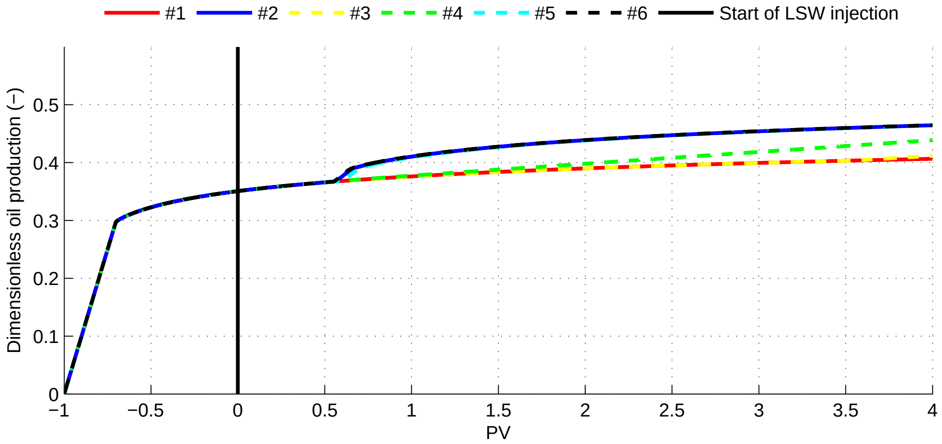

Figure 5.9: Oil production for various Buckley-Leverett simulation setups with varying salinity thresholds.

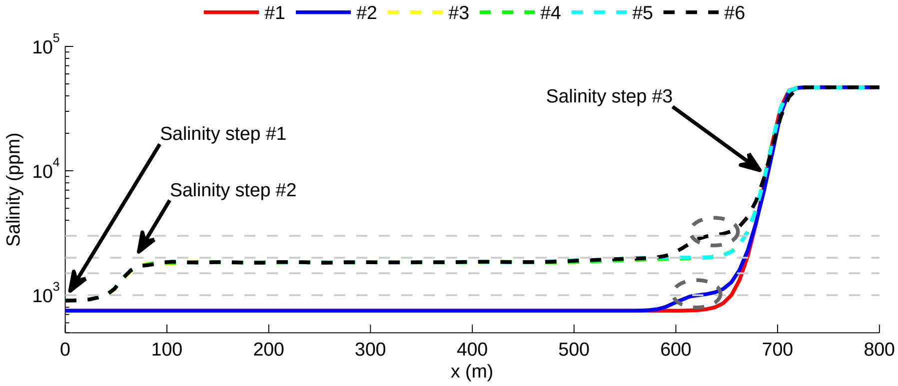

(a) Salinity profiles for various simulations a $t = 2200$ days

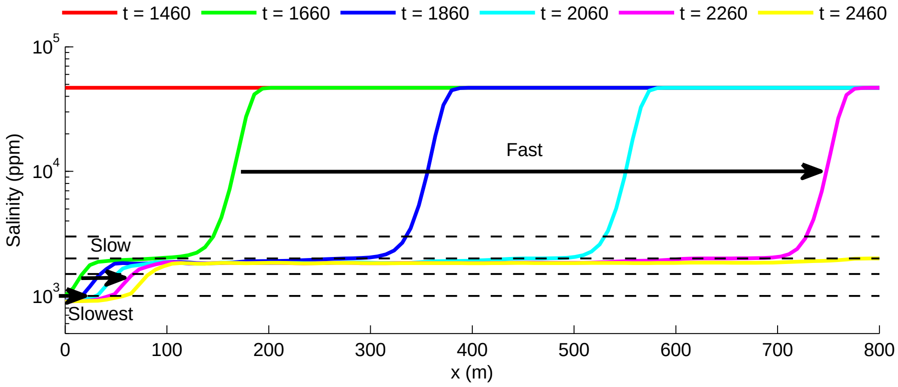

(b) Salinity profiles through time for simulation 5

Figure 5.10: Salinity profiles in the reservoir for various simulations and time steps.

these steps, the salinity profiles through the reservoir at various time steps in simulation 5 are plotted in Figure 5.10(b). Again, three salinity steps can be observed. Interestingly, the salinity steps do not travel through the reservoir with the same velocity.

The first salinity step is the slowest of the three steps and is related to full calcite dissolution. From earlier simulations (see Chapter 3) it was found that, to dissolve calcite in the first grid cell, around 2.0 PV of LSW need to be flushed through the first grid cell. Only when all calcite is dissolved, the salinity level of the injected LSW can be reached. As long as the calcite equilibrium is restored in the first grid cell due calcite dissolution, a minimum salinity of around 910 ppm will established already in the first grid cell.

The second salinity step is also slow, however it is faster than the first step. The second step is caused by calcite dissolution due to a change in cation exchanger composition. As the ionic strength of LSW is lower than that of FW, and at the same time the Na^+/Ca^{2+} ratio decreased when LSW was injected, Ca^{2+} will be more preferable to attach to the exchanger (see Chapter 3). When Ca^{2+} from the solution attaches to the exchanger the equilibrium with calcite will again be disturbed leading to additional calcite dissolution. As Na^{+} that was previously attached to the exchanger is replaced by Ca^{2+} originating from additional calcite dissolution, the overall salinity will increase resulting in the slow moving salinity step.

The fastest salinity step, salinity step #3, travels at the same velocity through the reservoir as the water phase. This salinity step forms the boundary between FW and LSW.

A more detailed overview of the geochemical processes is given in Figure 5.11. Figures 5.11(a)-5.11(c) show the salinity, amount of calcite, ion concentration and exchanger composition throughout the reservoir at time step $t = 2460$ days. Figures 5.11(d)-5.11(f) show the same information as the former three figures however, for time step $t = 7300$ days.

From these figures it is clear that salinity steps #1 and #2 are related to two different calcite dissolution waves in the reservoir. Salinity step #1 is related to a very slow moving full calcite dissolution wave, whereas salinity step #2 is related to a calcite dissolution wave that only dissolves a fraction of the calcite. The cause of the calcite dissolution wave forming the second salinity step is a change in cation exchange composition. This can also be observed in Figure 5.11, where is clear that the salinity step #2 coincides with a calcite dissolution wave and a change in cation exchange composition.

It must however be noted that the amount of ion exchange sites has been based on bulk rock data. As it is likely that the actual amount of cation exchange sites is lower, the impact of cation exchange on the salinity will be lower. That is, both the plateau salinity will be lower and the second salinity step will move faster through the reservoir. Further research with respect to rock surface chemistry is required to improve the estimate of the number cation exchange sites.

The increase in salinity due to the first salinity step is not much, the resulting salinity is still lower than the lowest threshold value. However, it is especially the concentration of double valence ions that is increased. This could potentially impact the low salinity EOR potential.

In Chapter 2 it was shown that the electrical double layer thickness is a function of the ionic strength. As the ionic strength is also a function of the ion valence, the increase in especially double valence ions has a large impact on EDL thickness. A next step would be not to use the salinity as a threshold, but rather define an ionic strength threshold in future projects that include geochemistry.

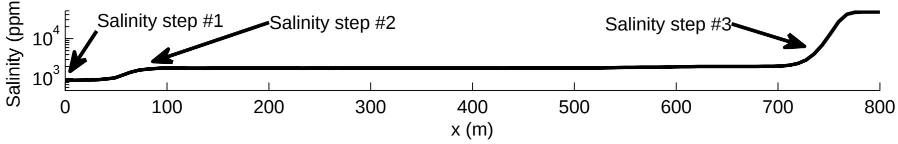

(a) Salinity profile at $t = 2460$ days

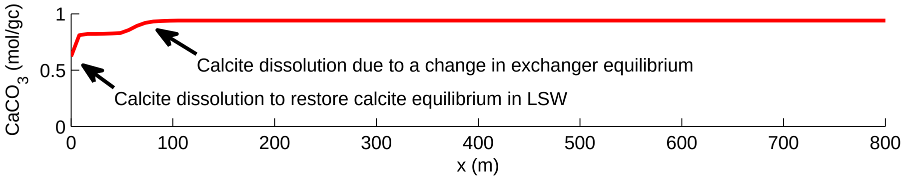

(b) Calcite profile at $t = 2460$ days

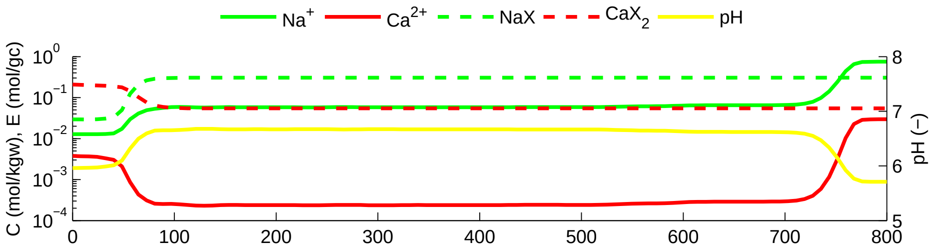

(c) Ion concentration, exchanger composition and pH at $t = 2460$ days

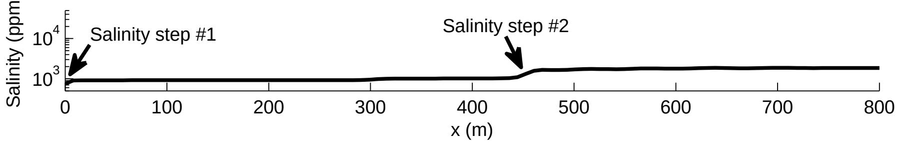

(d) Salinity at $t = 7300$ days

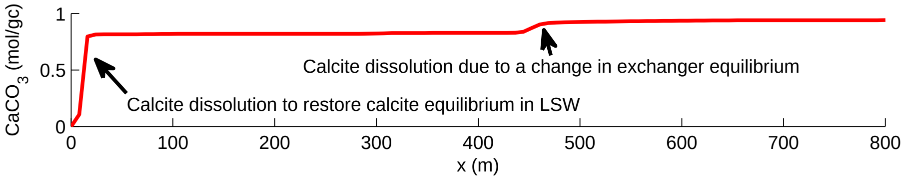

(e) Calcite profile at $t = 7300$ days

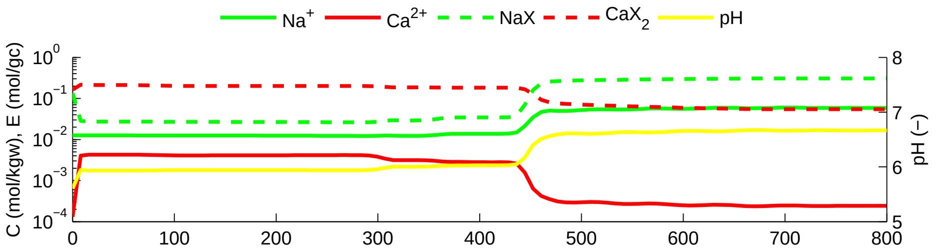

(f) Ion concentration, exchanger composition and pH at $t = 7300$ days

Figure 5.11: Figures 5.11(a)-5.11(c) show the salinity, calcite, ion concentration, exchanger composition and pH throughout the reservoir at time step $t = 2460$ days. Figures 5.11(d)-5.11(f) show the same information as the former three figures however, for time step $t = 7300$ days. Setup of simulation 5 used.

5.4 Effect of Slug Size

One of the methods to economically optimize low salinity flooding is to minimize the usage of LSW. In this section various simulations are run to investigate the impact of different LSW slug sizes on the recovery of oil and the underlying geochemical processes.

5.4.1 Simulation Modifications

All simulations carried out in this section are based on the base case simulation setup as described at the beginning of the chapter. A total of 5 simulations have been run for various slug sizes. See Table 5.7 for an overview of this section's simulations.

Table 5.7: Overview of slug size simulations

Simulation	#1	#2	#3	#4	#5
Slug size (PV)	0.1	0.2	0.4	1.0	2.0

All simulations carried out in this section are for a tertiary mode low salinity flooding system. That is, simulations have been carried out for a reservoir that has been flushed with 1.0 PV of FW and has produced around 35% of the OOIP during the period of conventional water flooding. Water breakthrough has already happened. The LSW slug will follow the FW. After the LSW slug again FW is flushed through the reservoir such that the total amount of water flushed through the reservoir is 5.0 PV.

5.4.2 Results

The results are divided in two parts. The first part (a) covers the oil recovery results and compares all 5 simulations. In the second part (b) the geochemical behavior of the simulated reservoir is evaluated for simulation 3, that is, for a slug of 0.4 PV of LSW.

a) Oil Recovery

Figure 5.12 shows the cumulative production profiles for all simulations of this section. These results suggest that the oil production is a function of the LSW slug size. This is not surprising, as the oil-favourable low salinity relative permeability model will only be used when the salinity is below the salinity threshold. When the salinity becomes higher again, due to the end of the

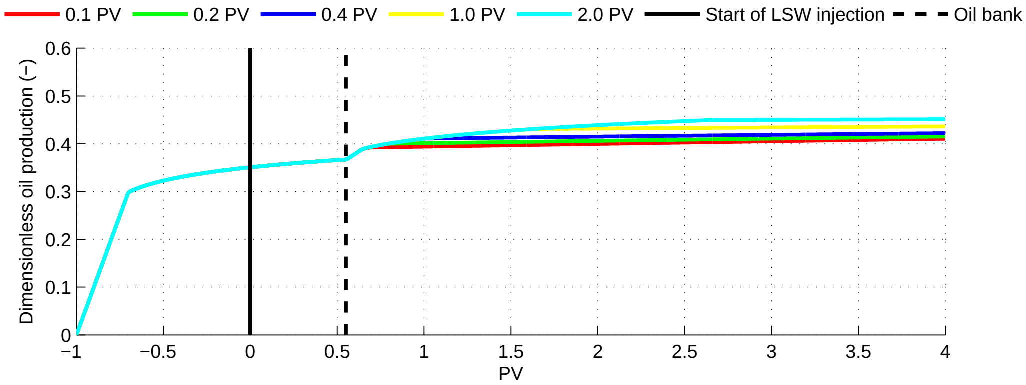

Figure 5.12: Cumulative oil production for various LSW slug sizes.

slug, the relative permeability model reverts back to the high salinity relative permeability model and consequently the oil production effectively halts.

The cumulative oil production profiles also suggest that injecting larger slugs always results in higher oil recovery. In the way the model has been build, by means of switching to a different relative permeability model and without taking into account the low salinity mechanism itself, or economics, this is true.

In real life, wells are shut-in when they produce too much water such that production is not economical anymore. This can be taken into account by introducing water cut limits. Figure 5.13 shows the increase in cumulative oil production, with respect to the time of the oil bank breakthrough, for various water cut limits as a function of the LSW slug size. The water cut limit has only been applied after the oil bank breakthrough. It is interesting to see that the increase in cumulative oil production is not simply growing for increasing

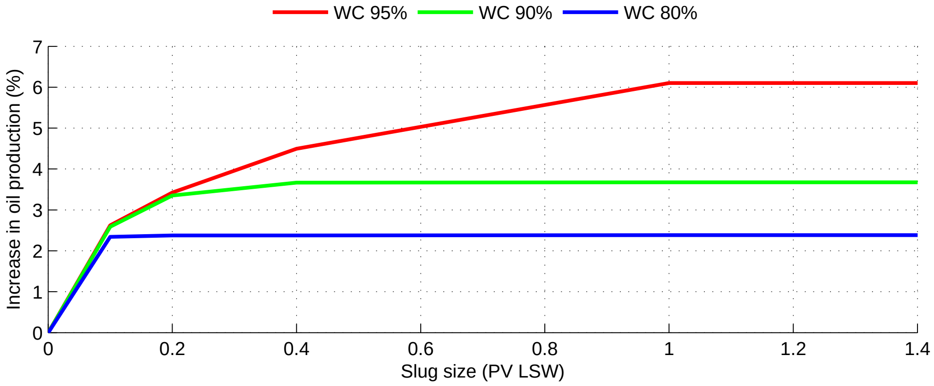

Figure 5.13: Increase in oil production with respect to the time of oil bank breakthrough as a function of LSW slug size for various water cut abandoning conditions.

slug sizes anymore. In fact, much smaller slug sizes may also be enough.

Due to the used relative permeability model, the water cut after water breakthrough is already relatively high, therefore also high water cut limits have been used. For this simulation the optimal slug size is less, or equal than 1.0 PV, depending on the shut-in criterium. Quantities of around 0.3-0.5 PV have been reported in the literature (Jerauld et al., 2006a, Seccombe et al., 2008) as optimal amount of LSW. Depending on the actual reservoir, dispersion and economical limits these values seem indeed to be applicable.

b) Geochemistry

When injecting a low salinity slug the geochemical processes as described in Section 5.3.2 are only allowed to take place for a short time. The low salinity slug will travel through the reservoir under influence of both geochemical processes and dispersion.

Figure 5.14 shows the low salinity slug moving through the reservoir for slug sizes between 0.1 and 0.4 PV. In Figure 5.14(a), for a LSW slug size of 0.1 PV, it can be observed that due to dispersion the salinity cannot reach very low salinity values (dark blue) throughout the whole column. For a slug size of double the size, as plotted in Figure 5.14(b), the salinity levels throughout the column are reaching low values for the salinity, albeit only for a very short

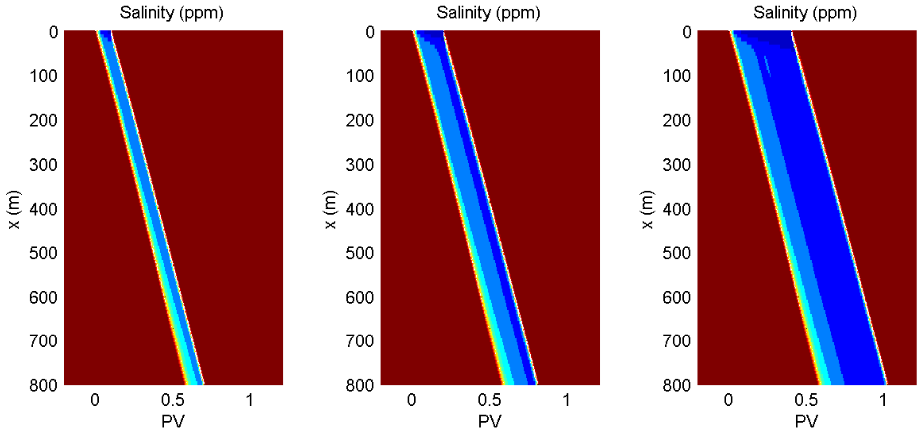

(a) Slug = 0.1 PV (b) Slug = 0.2 PV (c) Slug = 0.4 PV

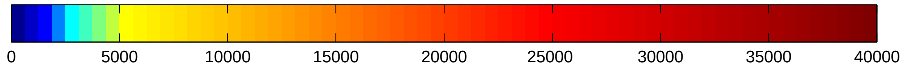

(d) Color bar, Salinity (ppm)

Figure 5.14: Salinity response of the reservoir for various slug sizes.

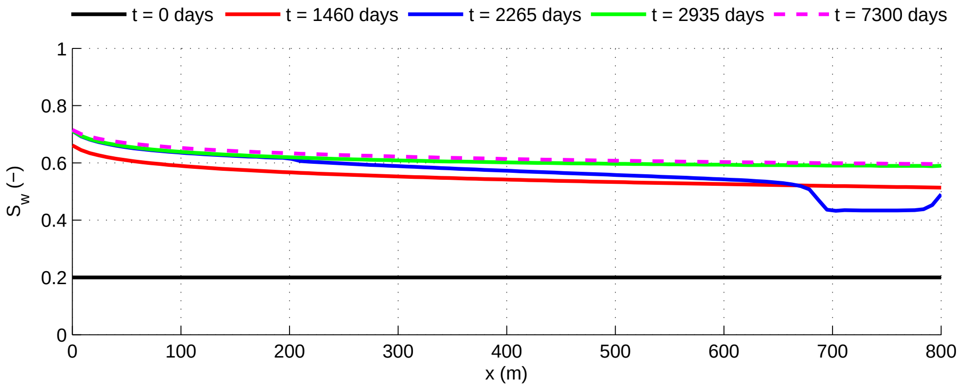

Figure 5.15: Water saturation at various time steps during a water injection scheme for a LSW slug size of 0.4 PV.

time.

As dispersion in real fields is not constant, nor precisely known, larger slugs are desired to compensate for this uncertainty. For a slug size of 0.4 PV, as plotted in Figure 5.14(c), the dispersion is not a very important anymore as the slug is wide.

Depending on the water saturation before injection of the LSW slug and of the width of the LSW slug, the water saturation may remain -almost- constant over time when reverting back to FW injection. Figure 5.15 illustrates this behavior.

For $t = 0$ days the water saturation is at initial values. After injecting 1.0 PV of FW the water saturation profile is represented by the red line ($t =$ 1460 days). From that moment LSW water will be injected, increasing the water saturation in the reservoir. The profile at $t = 2265$ days shows the saturation profile just before the oil bank breakthrough, which is the first time increased oil production can be observed at the well. The profile at $t = 2935$ marks the breakthrough of FW water and thus the end of low salinity associated oil production. At $t = 7300$ days, which is a long period of injecting FW later, the saturation profile has not changed much, meaning that the oil production effectively halted after the low salinity slug.

5.5 Influences of SRP Injection

In this section the influences of SRP water injection during LSW flooding are investigated. A detailed ionic composition can be found in Appendix C. The effect of disrupting tertiary low salinity water injection by regular SRP water injection periods is simulated for two different cases:

- Monthly injections of SRP water for a duration of 1-4 consecutive days.
- Yearly injection of SRP water for a duration of 2 consecutive weeks for various values of the dispersion tuning parameter β.

All other parameters used in the simulations are based on the base simulation as defined at the beginning of this chapter.

5.5.1 Monthly Short SRP Slugs

The effect of frequent injection of short SRP slugs on LSW flooding is investigated by injection of 1, 2 or 4 days of SRP water per month. Figure 5.16 shows the cumulative production profiles for the various SRP water injection schemes. For comparison, also the base case simulation without SRP water injection is plotted.

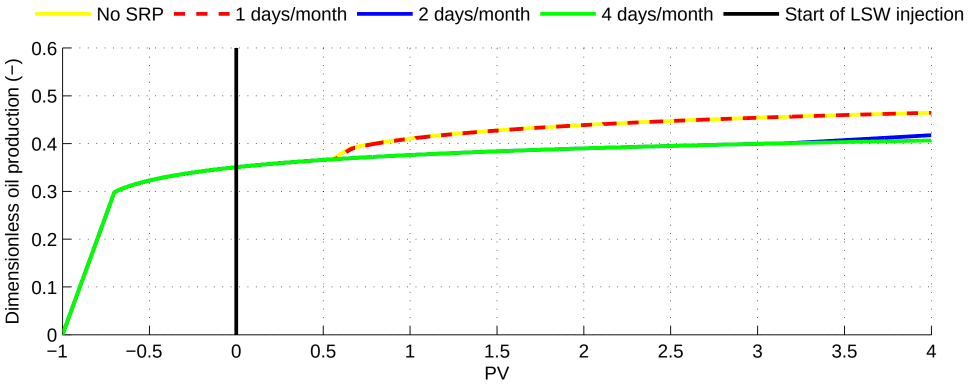

Figure 5.16: Cumulative oil production for 0-4 days/month SRP injection during LSW flooding.

No significant difference in oil production for the base case and 1 day per month of SRP water injection is visible. The simulation results suggest that a single day of SRP water injection does not have enough impact on the salinity to harm the low salinity effect. For the simulation cases with 2 and 4 consecutive days of SRP water injection per month a significant reduction in cumulative oil production can be observed. SRP water injection for around

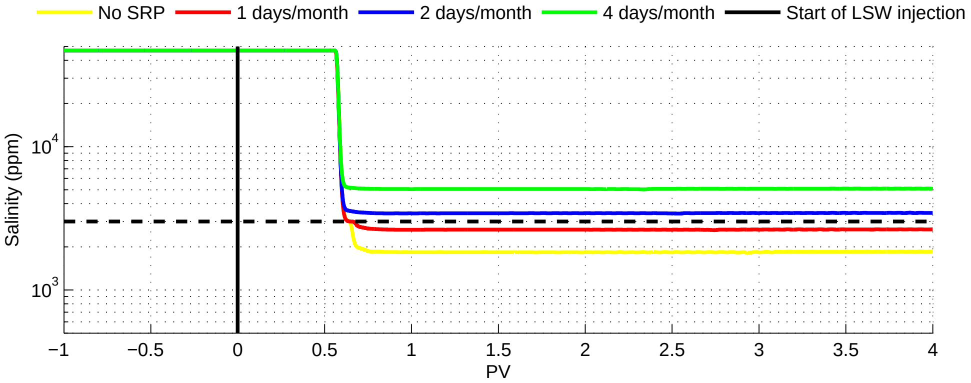

Figure 5.17: Salinity at the producer for various SRP slug injection schemes.

6% of the injection time per month already cancels out the low salinity effect and reduces the potential for increased oil recovery significantly.

In Figure 5.17 the salinity at the producer is plotted as a function of the amount of water injected. Water breakthrough of the LSW water happens after just over 0.5 PV of LSW has been injected. From this moment the salinity at the producer quickly drops towards a significantly lower value for all simulation cases. In the same figure, the base salinity threshold of 3,000 ppm is plotted.

No salinity fluctuations are observed at the producer. The salinity for all simulations is steady over time after water breakthrough. The constant level is however different for each simulation and increases for an increasing number of days of SRP injection. Both the cases without and with 1 day/month of SRP injection result in a salinity at the producer below the base threshold level of 3,000 ppm. For the cases with 2 and 4 days/month of SRP water injection the salinity at the producer is above the salinity threshold meaning that no low salinity effect will have taken place close to the producer. However, as the cumulative production profiles of the latter two cases do not show a significant increase in oil production it is likely that the threshold value of 3,000 ppm has been exceeded in most parts of the reservoir.

Plotting the salinity through time for specific grid cells shows that the quick salinity alterations level out to average values within a few grid cells. Figure 5.18 shows the salinity as a function of time for the first, fifth and tenth grid cell. The plots shows the period from $t = 1400$ days to $t = 1800$ days. That is, they start just before low salinity water is injected and cover just over one year of injection.

Grid cell #1, Figure 5.18(a), shows sharp peaks in salinity due to the temporary SRP injection each month. However, as a single day of injection roughly equals 0.5 m of travel distance (for high water saturation) the first

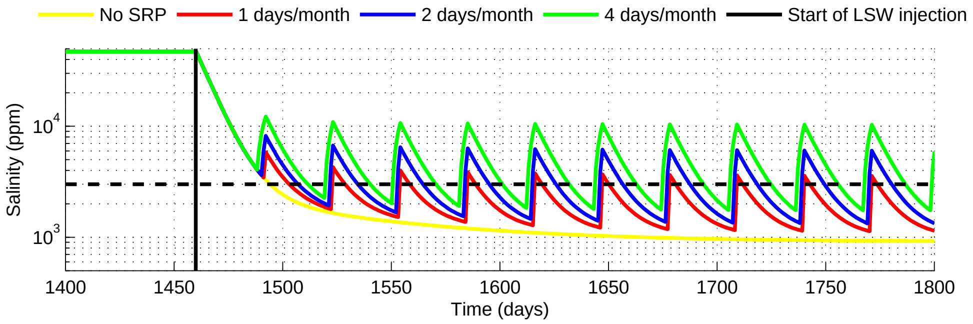

(a) Grid cell #1

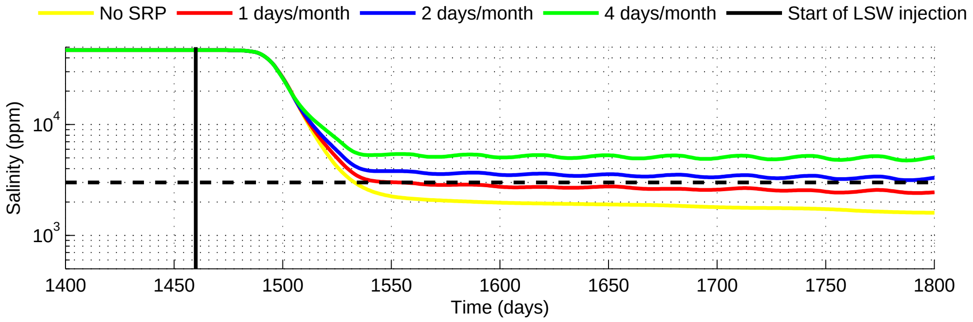

(b) Grid cell #5

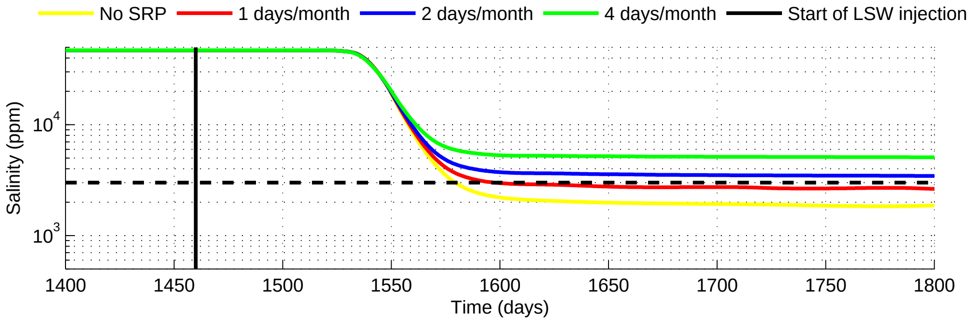

(c) Grid cell #10

Figure 5.18: Salinity of the first grid cell between $t = 1400$ and $t = 2000$ during injection of small SRP slugs of various lengths.

grid cell will not be fully flooded. This results in a salinity for the first grid cell of just over 10,000 ppm for the first SRP slug at $t = 1492$ days for the simulation with 4 days/month of SRP injection. The less SRP water injection is performed, the lower the salinity peaks and the more the solution converges to the salinity profile of the simulation without SRP injection.

Grid cell #5, Figure 5.18(b), is about 40 m into the reservoir. At this point wiggles in the salinity profile can still be observed but are not as sharp anymore as for the first grid cell. At 80 m in the reservoir, grid cell #5, Figure 5.18(b), the salinity profile in all simulation cases are stable after the initial drop in salinity. The stable salinity levels observed are equal to the levels earlier observed in Figure 5.17 for the salinity at the producer.

Due to the -relatively- fast switching between high and low saline waters a weighted average value salinity is established. As the absolute difference in salinity between the SRP water and the salinity threshold is much higher (27,000 ppm) compared to the absolute difference in salinity between LSW and the salinity threshold (2250 ppm) short periods of SRP injection time are sufficient to get salinity above the salinity threshold.

It must however be noted that by increasing the number of grid cells the spatial variations in salinity can be captured better. But, as the base dispersion of 7% of the travel distance ($7\% \cdot 800 = 56$ m) is much larger than the distance

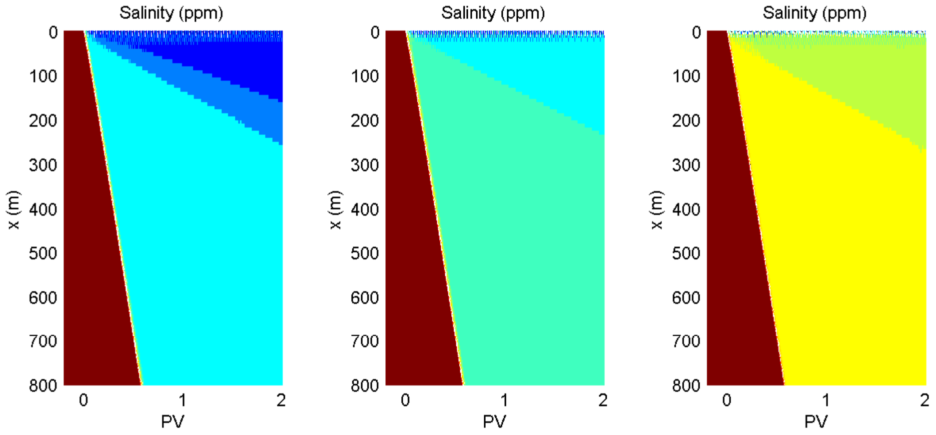

(a) 1 days/month (b) 2 days/month (c) 4 days/month

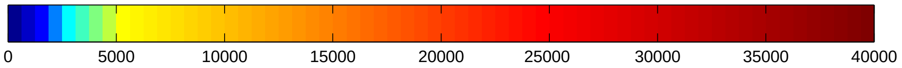

(d) Color bar, Salinity (ppm)

Figure 5.19: Salinity response of the reservoir for various amounts of monthly SRP injection days.

between the two SRP slugs (1 month $\sim$ 16 m) it seems likely that the slugs are fully dispersed after they have travelled a short distance through the reservoir.

From the results it follows that more than a single day of SRP water injection per month can have significant negative impact on the low salinity flooding process due to the impact on the salinity levels. The resulting salinity levels for 1, 2 and 4 days/month injection are plotted in Figure 5.19.

In the simulation the concentration of double valent ions do not play a role in the low salinity effect. Mind that when SRP water is injected, which has relatively high concentrations of both Ca^{2+} and Mg^{2+} ions, the low salinity effect can be further diminished by the increase in double valent ions.

5.5.2 Yearly Long SRP Slugs

As a second case, the injection of two consecutive weeks of SRP water on a yearly base is under investigation. The total amount of water that is injected per year in this case is comparable to the first case, it is only the timing of the injection that is significantly different. The impact of dispersion on the results is checked by changing the dispersion tuning parameter β.

Figure 5.20(a) shows the cumulative oil production for the base case without SRP injection in combination with the yearly SRP injection cumulative oil production profiles. Regardless of the fact that -more or less- the same

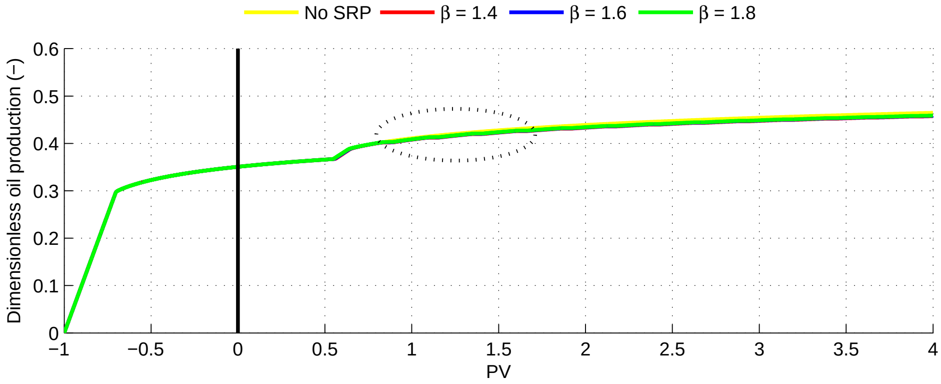

(a) Cumulative production

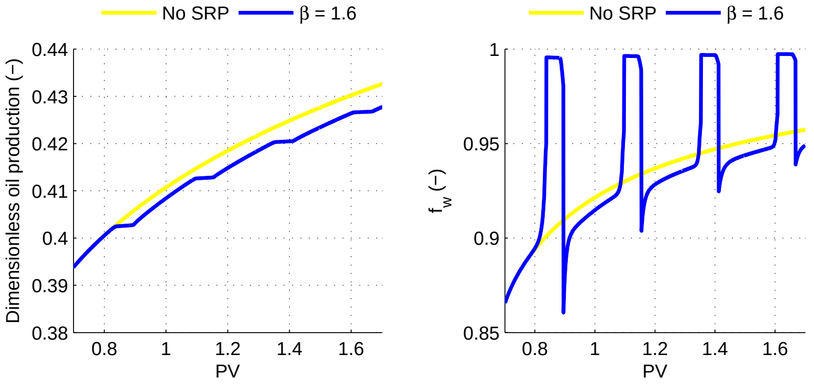

(b) Zoomed cumulative production (c) Zoomed water cut

Figure 5.20: Figure 5.20(a) shows the cumulative oil production results for simulations with 2 consecutive weeks per year of SRP injection for various values for the tuning parameter β. Figures 5.20(b) and 5.20(c) shown the zoomed in cumulative oil production and water cut for long yearly SRP slug injection, respectively. The dotted ellipse in Figure 5.20(a) shows the zoomed in portion of the cumulative production profile.

amount of SRP water is injected on a yearly base compared to the previous case, the cumulative oil production profiles hardly show any impact.

By zooming in on the cumulative production profile, see Figure 5.20(b), it becomes clear that the slugs-affected cumulative production profiles show periods of low oil production. Figure 5.20(c), which shows the water cut at the producer for the zoomed time frame, shows periodic increases of water cut.

As SRP water is injected into the reservoir for two consecutive weeks, the slugs are big enough to travel through the reservoir with salinities well above the base salinity threshold. As the salinity is above the threshold level the high salinity relative permeability model will be used locally, leading to a lower relative permeability for oil, and consequently a higher relative permeability for water. This leads to a temporary reduction in oil flow at the location of the SRP slug.

The cumulative production differences are however not very big, whereas one would expect bigger differences if only the periodic reduction of oil flow was taking place. As oil in low salinity areas is moving faster than oil in SRP areas oil banks will form behind each SRP slug. This can also be observed in Figure 5.20(c). Each period of high water fractional flow is followed by a period with a lower water fractional flow compared to the case without SRP water injection.

The SRP water slugs at $t = 2557$ days throughout the reservoir, in terms of salinity, are plotted in Figure 5.21. The salinity slugs are not dispersed fully when they reach the end of the reservoir and good distinction between SRP and LSW zones can be made.

The salinity throughout the reservoir has also been plotted in both space and time (-0.2 PV to 2.0 PV), see Figure 5.22. This again clearly visualizes that the slugs move through the reservoir, slowly disperse but still leave wide areas of the reservoir with salinity below the threshold value.

Before SRP slugs are injected, the ion concentration and exchanger occupation follow the behavior described in Section 5.3.2. Figures 5.23(a)-5.23(c) show the geochemical data at $t = 1810$ days, which is just before the first two-week SRP slug is injected.

Figures 5.23(d)-5.23(f) show the geochemical data throughout the reservoir at time step $t = 2555$ days. At this time step 3 SRP slugs are visible. The first and second slug have travelled a distance of approximately 650 m and 310 m, respectively, through the reservoir. They have been dispersed, significantly. A third slug is being injected at this time and disturbs the exchanger and ion composition near the injector. It may be clear that injecting SRP slugs leads to alternating exchanger composition near the injection wellbore. One is temporary ‘inverting’ the ongoing process, but as long as enough LSW water is flushed the overall process is not changed.

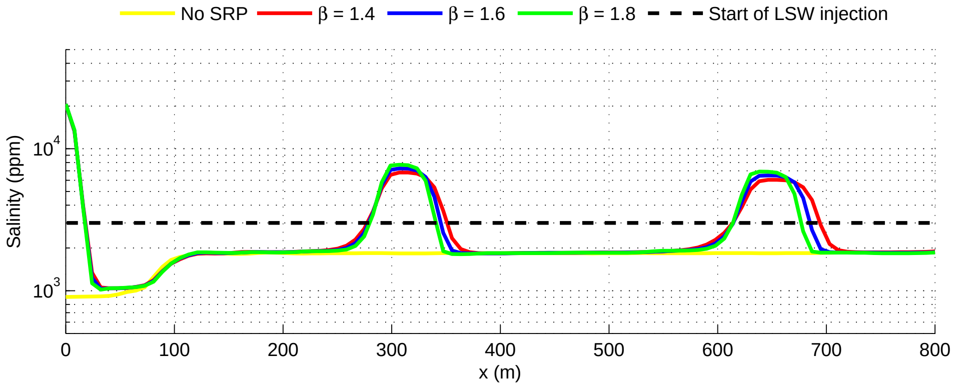

Figure 5.21: Salinity profile in the reservoir a $t = 2557$ days.

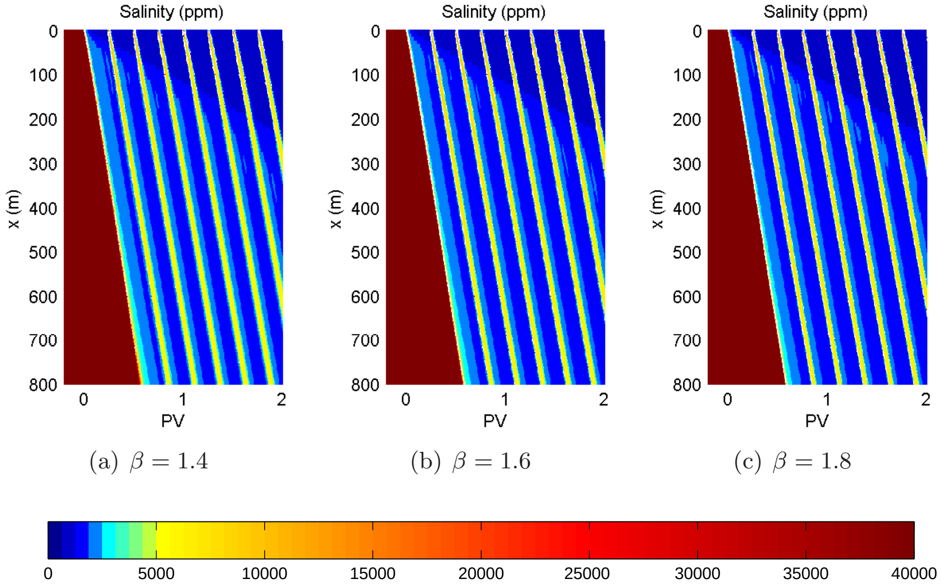

(a) $\beta = 1.4$ (b) $\beta = 1.6$ (c) $\beta = 1.8$

(d) Color bar, Salinity (ppm)

Figure 5.22: Salinity response of the reservoir for yearly injection of 2 consecutive days of SRP water injection. Plotted are the results for various values of the dispersion tuning parameter β.

Worth noting is that SRP water is relatively high in double valent ions like Ca^{2+} and Mg^{2+}. It has been discussed in Section 3.3.2 that low concentrations of Ca^{2+} can lead to vast different exchanger equilibria. For magnesium this has not been discussed as it was of little importance for the LSW simulations with the current assumptions (no Mg^{2+} in the LSW water; no Mg^{2+} source in the reservoir). However, when SRP water is injected the Mg^{2+} concentrations may play an important role on oil recovery.

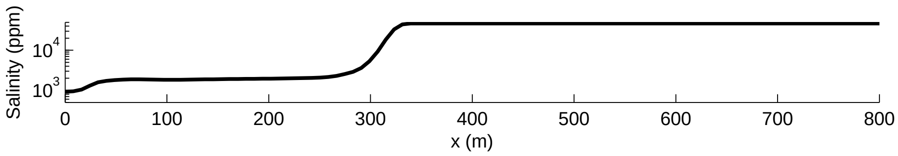

(a) Salinity profile at $t = 1810$ days

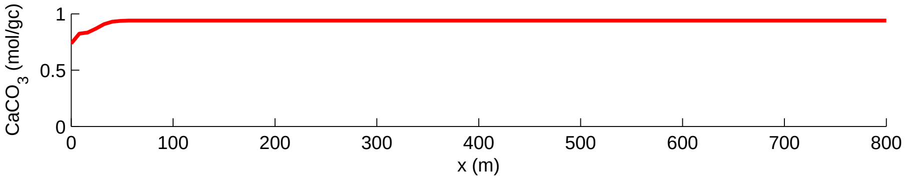

(b) Calcite profile at $t = 1810$ days

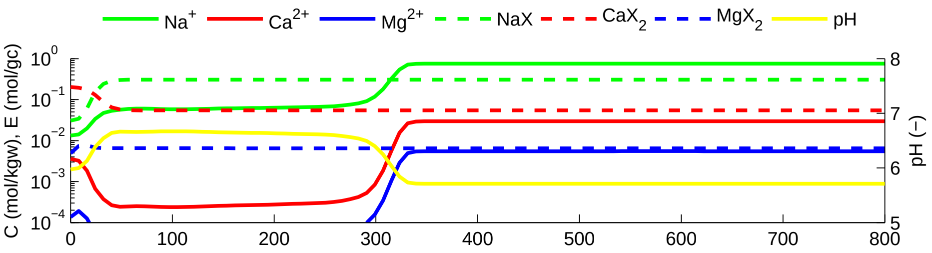

(c) Ion concentration, exchanger composition and pH at $t = 1810$ days

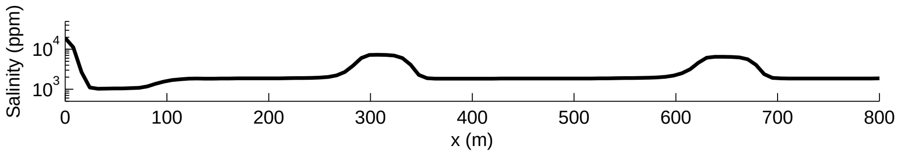

(d) Salinity at $t = 2555$ days

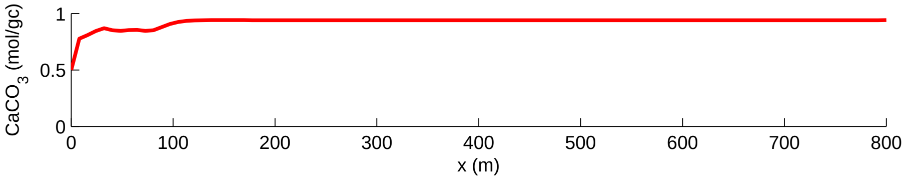

(e) Calcite profile at $t = 2555$ days

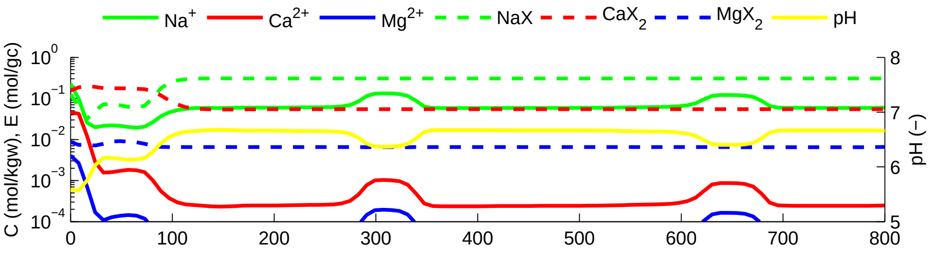

(f) Ion concentration, exchanger composition and pH at $t = 2555$ days

Figure 5.23: Figures 5.23(a)-5.23(c) show the salinity, calcite, ion concentration, exchanger composition and pH throughout the reservoir at time step $t = 1810$ days. Figures 5.23(d)-5.23(f) show the same information as the former three figures however, for time step $t = 2555$ days. Setup of simulation 3 used.

5.6 Low Salinity Fingerprints

Determining whether or not the low salinity effect has taken place in a reservoir is of importance to be able to define success criteria for low salinity projects. Simulations have been run to investigate the measurable changes at the producer, in secondary and tertiary flooding mode, for cases with and without low salinity effect. Except for the modifications mention below, the base case simulation setup is used as described at the beginning of this chapter.

5.6.1 Secondary Mode

The secondary flooding mode simulations are carried out for the injection of 5.0 PV of LSW from $t = 1$ day. In the simulation without LSW effect the relative permeability model is not allowed to switch, even if the salinity is lower than the salinity threshold. It is the high salinity relative permeability model that is always used. This is done to mimic a reservoir that is being flooded with low salinity water but does not have a response with respect to increased oil production. The other simulation is allowed to change relative permeability model as normal, if the salinity drops below the salinity threshold. See Figure 5.24 on page 107 for results on the cumulative oil production, salinity and water cut at the producer.

In secondary mode low salinity water flooding the increase in oil production is mainly visible just after initial water breakthrough. Before the water breakthrough oil was being produced at a high constant rate. After water breakthrough, water and oil will be co-produced at a constant ratio for a limited amount of time. It is during this time that the difference in water cut for the simulation with LSW effect and the simulation without LSW is the clearest. If no LSW effect would have taken place, no constant water cut regime would have occurred. Mind that the constant water cut regime happens long before a reduction is salinity is visible. From the moment that the salinity at the producer drops, the water cut starts to increase again.

The salinity, as measured at the producer, does not produce significant differences for both simulation cases. It is therefore unlikely that a success criteria can be formulated purely based on the geochemical composition of the produced water. As oil is modelled only as a single-phase, without internal components, no information about composition of the produced oil can be calculated. A more detailed implementation on oil chemistry, for example based on the oil complexation paper by Sandengen et al. (2011), could lead to improved success criteria as predictions for the ratio between acidic and basic oil particles in the produced oil can be calculated.

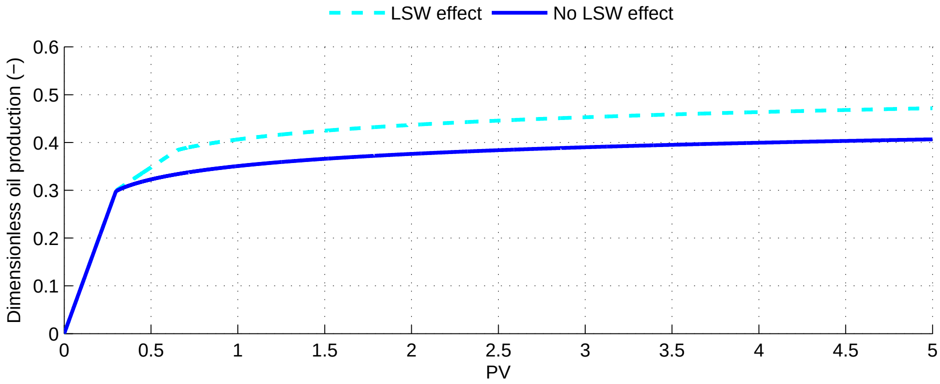

(a) Cumulative oil production

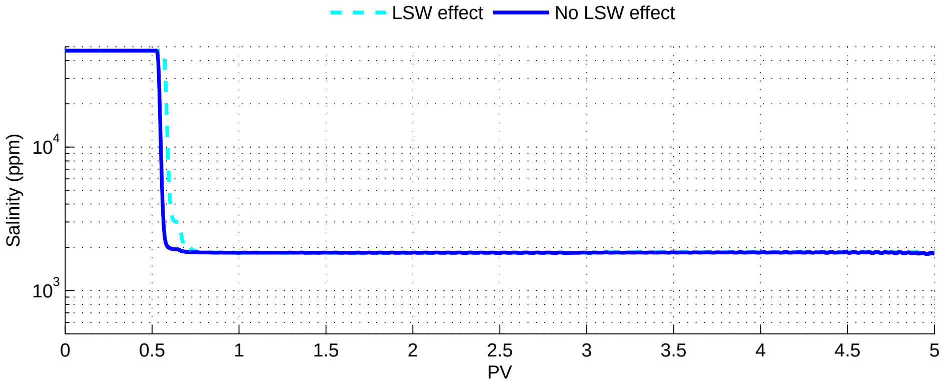

(b) Salinity

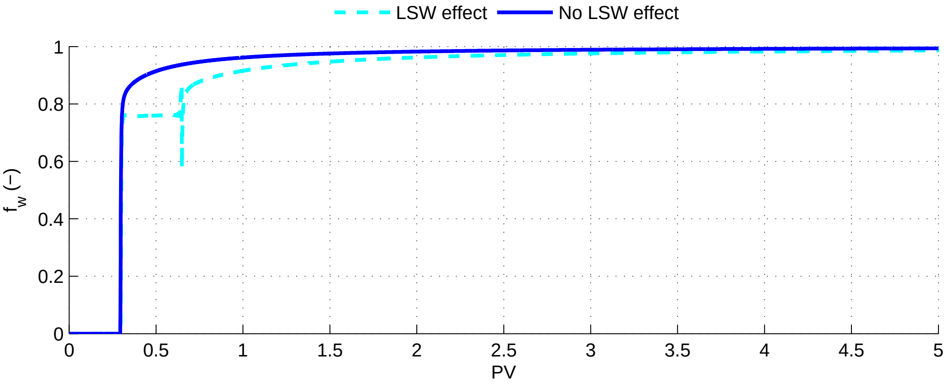

(c) Water cut

Figure 5.24: Comparison between measurable results at the producer for a case with and without the low salinity effect in secondary mode.

5.6.2 Tertiary Mode

The tertiary flooding mode simulations are carried out for the injection of 1.0 PV of formation water followed by 4.0 PV of LSW water. Again, in one of the two simulations the relative permeability model is fixed to the high salinity model and is not allowed to switch even if the salinity is below the threshold value. See Figure 5.25 on page 109 for results on the cumulative oil production, salinity and water cut at the producer.

In tertiary mode low salinity water flooding an oil bank will form in the reservoir and propagate to the producer. When the oil bank arrives at the producer a significant drop in water cut will be visible. The water cut remains constant during the time it takes to fully produce the oil bank. After the oil bank has been produced, the water cut will rise again. As the oil bank is pushed in front of the low salinity water, the drop in water cut happens earlier than the drop in salinity at the producer.

Comparing the results to the simulation without low salinity effect it is clear that especially the drop in water cut breaks the overall trend and is therefore the easiest feature to spot and can be used as success criteria for low salinity projects.

The salinity, as measured at the producer, does not show significant differences between both simulation cases. Again, it is unlikely that a success criteria can be formulated based on the geochemical composition of the aqueous phase alone.

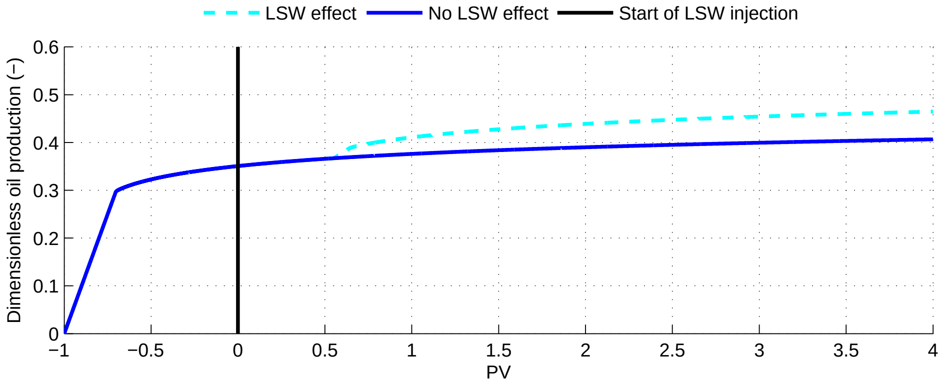

(a) Cumulative oil production

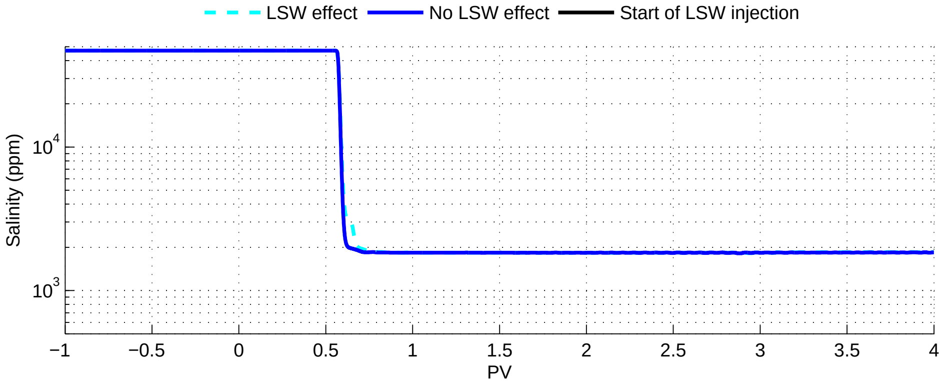

(b) Salinity

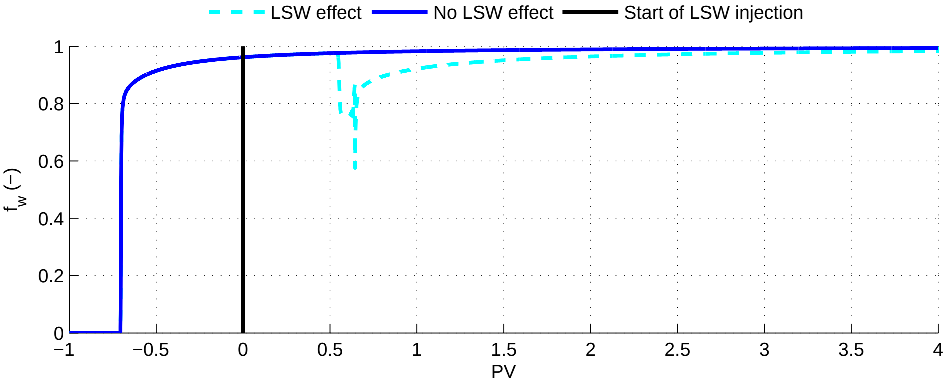

(c) Water cut

Figure 5.25: Comparison between measurable results at the producer for a case with and without the low salinity effect in tertiary flooding mode.

Chapter 6

Conclusions and Further Work

Geochemical processes taking place in the case study field were modelled using the PHREEQC geochemical package. Simulations were run to study the geochemical processes taking place in the reservoir. Next, a Buckley-Leverett flow simulator was coupled to PHREEQC simulator. The resulting multiphase simulator was used to carry out simulations to investigate the influence of geochemical interactions on the EOR potential of low salinity water flooding.

From the simulations carried out in this thesis for the case study field it was found that geochemical interactions between the reservoir's aqueous phase and the rock will influence salinity levels during low salinity water flooding.

By injecting low salinity water into the reservoir, calcite (content of 0.97 Wt%) will dissolve, increasing the minimum salinity that will be reached in the majority of the field to 910 ppm. To fully remove calcite from the reservoir would require an excessive amount of pore volumes of low salinity water to be injected. Full dissolution of calcite therefore, is a near injector well-bore effect only. As a result, a minimum Ca^{2+} concentration of 160 ppm will establish in the majority of the reservoir during production lifetime.

Adsorption of Ca^{2+} on the cation exchanger will occur upon injection of low salinity water. This is due the preferential adsorption of higher valence ions as a result of lowering the ionic strength, and a decrease in the Na^+/Ca^{2+} ratio. The adsorption of Ca^{2+}, which lowers the Ca^{2+} concentration in the aqueous phase, is counteracted by extra calcite dissolution, effectively resulting in higher salinities. Depending on the amount of cation exchanger sites, significantly higher salinities have been observed ($\sim$2000 ppm) as a result of this phenomenon. As the low salinity effect is assumed to be a function of the reservoir's salinity, including geochemical interactions can lead to a lower EOR potential.

The increase in oil production observed for a non-geochemical affected secondary low salinity injection scheme (1.0 pore volume formation water followed by 4.0 pore volumes low salinity water) is 5.8% of the OOIP compared to a high salinity injection scheme (5.0 pore volumes of formation water), for low salinity thresholds ranging from 1000-3000 ppm. By including geochemical interactions, the amount of incremental oil was 0.5%, 3.2%, 5.7% or 5.8% of the OOIP for a salinity threshold of 1000 ppm, 1500 ppm, 2000 ppm, or 3000 ppm, respectively. This indicates that, especially for low values of the low salinity threshold, geochemical interactions may be of importance for the EOR potential.

Dispersion was found to be very important for the determination of minimum low salinity slug sizes. However, no accurate dispersion data were available for the case study field to verify the current model. Simulation results showed that frequent (2 days/month) injection of seawater slugs during low salinity flooding may increase salinity levels throughout the whole reservoir above the threshold values, effectively eliminating the increase in oil production. Injecting larger seawater slugs on a less regular interval (2 weeks/year) results in fractions of the reservoir having a higher salinity than the threshold value. However, the overall impact on the cumulative oil production was far less (-0.6% of the OOIP compared to no seawater slugs).

By coupling the geochemical package PHREEQC to a multiphase Buckley-Leverett simulator it was shown that it is both viable to do so, and that the reservoir's salinity levels are affected by geochemical interactions. Although the low salinity mechanisms are still subject of extensive research, it is assumed that increases in oil recovery due to low salinity water flooding can be modelled as a change in relative permeability, from oil- or mixed-wet to more water-wet. It has also been shown that the low salinity EOR potential may be decreased by including geochemical interactions. These results however are based on many assumptions and simplifications.

First and foremost, the number of cation exchange sites has been calculated based on bulk rock data. This has likely resulted in too high estimates of the number of cation exchange sites, as it is only the rock surface which determines the interacting amount of exchange sites. In addition, it has been assumed that all rock can be contacted by the aqueous phase, which again overestimates the influence of geochemical interactions on the salinity. A recommendation for further work would therefore be to study the mineralogical composition of the rock surface as to improve the estimate of the amount of cation exchange sites.

The current simulation model can be enhanced by including geochemical interactions with more rock types, introducing surface complexation or by including clay mobilization. Another interesting possibility is to include oil chemistry.

During the course of this thesis, some effort was put into investigating the oil complexation theory by Sandengen et al. (2011) in collaboration with the Statoil Research Centre in Trondheim. A simple PHREEQC model was build that could be used to simulate the sorption of acidic and basic oils. The work, which is not included in this thesis, did not yet produce conclusive results but could form the basis of an highly interesting continuation of this project.

The current standard technique to model the low salinity effect is by means of a salinity threshold. This technique is also employed in this thesis. When however geochemical reactions are added to a reservoir simulator, more complex low salinity thresholds could be formulated that are not solely a function of salinity but, for example, also take the ratio between mono- and divalent ions into account. Formulating an accurate threshold would involve an in-depth study of the low salinity mechanism or empirical research, and has the potential to improve the results of low salinity flooding simulations.

Appendix A

PVT Data

Table A.1: PVT datasheet of reservoir conditions

Measurement	**T** (°C)	ρ (kg/m^3)	η (mPa·s)	**CO$_2$** (mol%)	P_{sat} (bara)	P_r (bara)
#1	83.3	781.0	1.3	1.099 %	213.9	248.5
#2	85.0	778.4	1.3	1.020 %	219.9	251.2
#3	N/A	807.0	3.0	0.730 %	197.0	232.0
#4	85.6	810.0	2.3	1.151 %	203.7	251.3
#5	84.9	814.0	N/A	1.008 %	184.1	N/A
#6	80.6	812.0	1.6	1.124 %	220.4	248.2
#7	85.0	801.1	1.8	1.100 %	202.5	248.3
#8	85.0	799.9	1.7	0.850 %	214.0	240.0
#9	85.0	812.9	2.5	0.960 %	190.5	250.1
#10	85.0	812.1	2.0	0.830 %	218.5	244.0
#11	85.0	816.5	2.5	1.180 %	196.5	251.2
#12	82.5	813.0	2.1	0.700 %	201.5	248.0
#13	82.2	823.0	2.3	1.276 %	200.6	252.2
#14	85.0	799.9	3.0	0.770 %	229.0	246.5
#15	85.0	828.9	2.6	0.790 %	186.1	254.2
#16	85.0	828.6	3.3	0.550 %	184.5	252.6
#17	85.0	819.8	3.9	0.710 %	199.5	251.1
#18	84.0	836.0	2.7	0.670 %	190.0	253.0
#19	83.0	N/A	3.0	0.915 %	210.0	248.0
#20	85.0	829.3	2.6	0.820 %	208.0	240.0
#21	83.0	811.2	2.2	1.209 %	190.7	250.0
Average, μ	84.2	811.7	2.4	0.927 %	202.9	248.0
Std. deviation, σ^2	1.3	14.8	0.7	0.206 %	13.0	5.4

Appendix B

Rock Data

Table B.1: Porosity measurements (Bøe, 2010)

Measurement	**Depth (m)**	**Porosity (%)**
#1	3183.63	28
#2	3184.78	23
#3	3221.63	20
#4	3221.73	24
#5	3222.73	21
#6	3222.78	15
Average		22

Table B.2: Rock composition (Rozhko and Faanes, 2009)

	ρ	M	x	C[1]	C	**Min CEC**[2]	**Max CEC**
	(g/cm^3)	**(g/mol)**	**(Wt%)**	**(mol/l)**	**(g/l)**	**(meq/kg)**	**(meq/kg)**
Illite/Smectite	2.42	469.205	0.00 %	0	0.0	800	1200
Illite+Mica	2.75	389.34	8.78 %	2.23	869.8	200	500
Kaolinite	2.62	258.16	10.05 %	3.67	948.2	30	150
Chlorite	2.65	595.22	3.12 %	0.50	297.4	100	400
Quartz	2.65	60.08	63.53 %	100.9	6063.1	N/A	N/A
K Feldspar	2.53	278.33	7.93 %	2.60	722.8	N/A	N/A
Plagioclase	2.67	270.77	3.78 %	1.34	363.8	N/A	N/A
Calcite	2.71	100.086	0.97 %	0.94	94.3	N/A	N/A
Dolomite	2.84	184.4	0.95 %	0.53	97.2	N/A	N/A
Siderite	3.74	115.86	0.83 %	0.97	112.2	N/A	N/A
Pyrite	4.84	119.98	0.00 %	0	0.0	N/A	N/A

[1] $n = \frac{1000(1-\phi)x\rho}{\phi M}$, see list of symbols. (Hellevang and Aagaard, 2011)

[2] Source: Apello and Postma (2005)

Appendix C

Water Composition Data

Table C.1: Water compositions.

		FW[1]		**LSW**[2]		**SRP**[3]	
Ion	**Mol Mass**	**Concentration**		**Concentration**		**Concentration**	
	(g/mol)	**(ppm)**	**(mol/l)**	**(ppm)**	**(mol/l)**	**(ppm)**	**(mol/l)**
Na^+	22.99	17,267	7.51E-01	295	1.28E-02	10,200	4.44E-1
K^+	39.10	398	1.02E-02	-	-	397	1.02E-2
Ca^{2+}	40.08	1,186[4]	2.96E-02	-	-	174	4.34E-3
Mg^{2+}	24.31	134	5.51E-03	-	-	233	9.58E-3
Ba^+	137.34	99	7.21E-04	-	-	-	
Sr^+	87.62	61	6.96E-04	-	-	2	2.28E-5
Cl^-	35.45	27,660	7.80E-01	455	1.28E-02	17,400	4.91E-1
SO_4^-	96.06	19	1.98E-04	-	-	47	4.89E-4
B^+	10.81	74	6.85E-03	-	-	-	-
Al^{3+}	26.98	1	3.71E-05	-	-	-	-
Si^{2+}	28.08	24	8.55E-04	-	-	-	-
Li^+	6.94	12	1.73E-03	-	-	-	-

[1] Source: Internal Statoil resources (DBR). (pH=5.7)
[2] Source: Well X SWCTT STARS simulations. (pH=6.0)
[3] Source: Well Y SWCTT Ion concentration data sheet. (pH =6.0)
[4] Adjusted to match equilibrium with calcite.

Bibliography

Abdallah, W., Buckley, J., Carnegie, A., Edwards, J., Herold, B., Fordham, E., Graue, A., Habashy, T., Seleznev, N., Signer, C., and Others (2007). Fundamentals of Wettability. *Oilfield Review*, 19(2):44–63.

Alsofi, A. M. and Blunt, M. J. (2010). Control of Numerical Dispersion in Simulations of Augmented Waterflooding. *SPE Improved Oil Recovery Symposium*, pages 1–12.

Anderson, W. (1987). Wettability Literature Survey Part 5: The Effects Of Wettability On Relative Permeability. *Journal of Petroleum Technology*, 39(11):1453–1468.

Apello, C. and Postma, D. (2005). *Geochemistry, groundwater and pollution.* A.A. Balkema Publishers, Leiden, 2nd edition.

Awan, A., Teigland, R., and Kleppe, J. (2008). A Survey of North Sea Enhanced-Oil-Recovery Projects Initiated During the Years 1975 to 2005. *SPE Reservoir Evaluation & Engineering*, (June):497–512.

Bøe, R. (2010). Petrographical Analysis of 11 Sandstone Plugs from [...] and [...] Formations, the [...] field. Technical report, SINTEF Petroleum Research, Trondheim.

Buckley, S. and Leverett, M. (1942). Mechanism of Fluid Displacement in Sands. *AIME*, (146):107–116.

Charlton, S. R. and Parkhurst, D. L. (2011). Modules Based on the Geochemical Model PHREEQC for Use in Scripting and Programming Languages. *Computers & Geosciences*, pages 1–37.

Chen, Z. (2008). *Reservoir Simulation: Mathematical Techniques in Oil Recovery.* SIAM/Society for Industrial and Applied Mathematics.

Chilingar, G., Mazzullo, S., and Rieke, H. (1996). *Carbonate Reservoir Characterization: A Geologic-Engineering Analysis, Part 2.* Elsevier Scientific Pub. Co., New York.

Chin, D. (2006). *Water-Quality Engineering in Natural Systems.* Wiley-Interscience, New Jersey.

Dake, L. (1978). *Fundamentals of Reservoir Engineering.* Elsevier Scientific Pub. Co., Oxford, 19th edition.

Deynoux, M., Miller, J., and Domack, E. (2004). *Earth's Glacial Record.* Cambridge University Press, Cambridge.

Drummond, C. and Israelachvili, J. (2004). Fundamental Studies of Crude Oil-Surface Water Interactions and its Relationship to Reservoir Wettability. *Journal of Petroleum Science and Engineering*, 45(1-2):61–81.

Grahame, D. (1947). *Electrical Double-layer and the Theory of Electro Capillary.*

Hellevang, H. and Aagaard, P. (2011). Mobilization of Divalent Metal Cations in the Peregrino Oil Sand. Technical report, University of Oslo.

Hirsch, C. (2007). *Numerical Computation of Internal and External Flows - Fundamentals of Computational Fluid Dynamics.* Elsevier, Oxford, 2nd edition.

Isaacson, E. (1980). *Global Solution of a Riemann Problem for Non Strictly Hyperbolic System of Conservation Laws Arising in Enhanced Oil Recovery.* The Rockefeller University, New York.

Jerauld, G., Webb, K., Lin, C., and Seccombe, J. (2006a). Modeling Low-Salinity Waterflooding. In *SPE Annual Technical Conference and Exhibition*, number December, pages 24–27.

Jerauld, G. R., Lin, C. Y., Webb, K. J., and Seccombe, J. C. (2006b). Modeling Low-Salinity Waterflooding.

Koenig, H. (1998). *Modern Computational Methods.* Series in Computational and Physical Processes in Mechanics and Thermal Sciences. Taylor & Francis.

Lager, A., Webb, K., and Black, C. (2007). Impact of Brine Chemistry on Oil Recovery. *14th European Symposium on Improved Oil Recovery.*

Lager, A., Webb, K., J. Black, C., Singleton, M., and Sorbie, K. (2008). Low Salinity Oil Recovery-An Experimental Investigation. *Petrophysics*, 49(1):1–12.

Lantz, R. (1971). Quantitative Evaluation of Numerical Diffusion (Truncation Error). *Society of Petroleum Engineers Journal*, (2).

Mahadevan, J., Lake, L. W., Johns, R. T., and Texas, U. (2003). Estimation of True Dispersivity in Field-Scale Permeable Media. *SPE Journal*, (September).

Mahani, H., Sorop, T., Ligthelm, D., Brooks, D., Vledder, P., Mozahem, F., and Ali, Y. (2011). Analysis of Field Responses to Low-salinity Waterflooding in Secondary and Tertiary Mode in Syria. In *SPE EUROPEC/EAGE Annual Conference and Exhibition*.

Mitchell, R. W. and Finch, E. M. (1981). Water Quality Aspects of North Sea Injection Water. *Journal of Petroleum Technology*, 33(6):1141–1152.

Moran, M., Shapiro, H. N., Boettner, D. D., and Bailey, M. (2010). *Fundamentals of Engineering Thermodynamics*. John Wiley & Sons, Inc., West Sussex, 7 edition.

Omekeh, A., Friis, H., Fjelde, I., and Evje, S. (2012). Modeling of Ion-Exchange and Solubility in Low Salinity Water Flooding. *Proceedings of SPE Improved Oil Recovery Symposium*.

Parkhurst, D. L. and Apello, C. (1999). User's Guide to PHREEQC (Version 2)–A Computer Program for Speciation, Batch-Reaction, One-Dimensional Transport, and Inverse Geochemical Calculations. Technical report, U.S. Geological Survey, Denver.

Pokrovsky, O. S., Golubev, S. V., Schott, J., and Castillo, A. (2009). Calcite, Dolomite and Magnesite Dissolution Kinetics in Aqueous Solutions at Acid to Circumneutral pH, 25 to 150 Degree Celcius and 1 to 55 atm pCO2: New Constraints on CO2 Sequestration in Sedimentary Basins. *Chemical Geology*, 265(1-2):20–32.

Pope, G. (1980). The Application of Fractional Flow Theory to Enhanced Oil Recovery. *Old SPE Journal*, 20(3):191–205.

Pozrikidis, C. (2009). *Fluid Dynamics: Theory, Computation, and Numerical Simulation*. Springer, New York, 2nd edition.

Raza, S., Treiber, L., and Archer, D. (1968). Wettability of Reservoir Rocks and its Evaluation. *Prod. Monthly*, 33(4):2–7.

RezaeiDoust, a., Puntervold, T., Strand, S., and Austad, T. (2009). Smart Water as Wettability Modifier in Carbonate and Sandstone: A Discussion of Similarities/Differences in the Chemical Mechanisms. *Energy & Fuels*, 23(9):4479–4485.

Robertson, E. P. (2007). Low-Salinity Waterflooding To Improve Oil Recovery - Historical Field Evidence. *SPE Annual Technical Conference and Exhibition*.

Rozhko, A. and Faanes, S. (2009). Low Salinity Water Injection Study on [...] Formation Core Material from the [...] Field. Technical report, Weatherford Laboratories, Trondheim.

Sandengen, K., Tweheyo, M., Raphaug, M., Kjø lhamar, A., Crescente, C., and Kippe, V. (2011). Experimental Evidence of Low Salinity Water Flooding Yielding More Oil-Wet Behaviour. In *International Symposium of the Society of Core Analysts*, pages 1–12.

Schlumberger (2012). Oilfield Glossary.

Seccombe, J. C., Lager, A., Webb, K., Jerauld, G., and Fueg, E. (2008). Improving Wateflood Recovery: LoSal(TM) EOR Field Evaluation. *Improved Oil Recovery Symposium*, pages 1–19.

Smith, J. and Ehrenberg, S. (1989). Correlation of Carbon Dioxide Abundance with Temperature in Clastic Hydrocarbon Reservoirs: Relationship to Inorganic Chemical Equilibrium. *Marine and Petroleum Geology*, 6.

Spycher, N. F. and Reed, M. H. (1988). Fugacity Coefficients of H2, CO2, CH4, H2O and of H2O-CO2-CH4 Mixtures: A Virial Equation Treatment for Moderate Pressures and Temperatures Applicable to Calculations of Hydrothermal Boiling. *Geochimica et Cosmochimica Acta*, 52(3):739–749.

Statoil ASA (2010). Mechanisms of Low Salinity Oil Recovery: Influence of the Expansion of the Electrical Eouble Layer - Theoretical and Experiments. Technical report, Trondheim.

Statoil ASA (2012). Energy Perspectives: Long-Term Macro and Market Outlook. Technical report.

Stumm, W. and Morgan, J. (1996). *Aquatic Chemistry.* John Wiley & Sons, Inc., New York.

Sumnu-Dindoruk, D. and Dindoruk, B. (2008). Analytical Solution of Non-isothermal Buckley-Leverett Flow Including Tracers. *SPE Reservoir Evaluation & Engineering*, pages 555–564.

Swaddle, T. (1997). *Inorganic chemistry: An Industrial and Environmental Perspective.* Academic Press, San Diego.

Tang, G. and Morrow, N. (1999a). Oil Recovery by Waterflooding and Imbibition - Invading Brine Cation Valency and Salinity. *Proceedings of the 99th International Symposium of the*, (Table 3).

Tang, G. and Morrow, N. R. (1997). Salinity, Temperature, Oil Composition, and Oil Recovery by Waterflooding. *SPE Reservoir Engineering*, 12(4):269–276.

Tang, G. and Morrow, N. R. (1999b). Influence of Brine Composition and Fines Migration on Crude Oil/Brine/Rock Interactions and Oil Recovery. *Journal of Petroleum Science and Engineering*.

Van Olphen, H. (1977). *Introduction to Clay Colloid Chemistry*. New York, 2nd edition.

Vledder, P., Gonzalez, I., Carrera Fonseca, J., Wells, T., and Ligthelm, D. (2010). Low Salinity Water Flooding: Proof Of Wettability Alteration On A Field Wide Scale. In *SPE Improved Oil Recovery Symposium*.

Yildiz, H. O. and Morrow, N. R. (1996). Effect of Brine Composition on Moutray Crude Oil by Waterflooding. *Journal of Petroleum Science and Engineering*, 14:159–168.